The ZEUS Micro-Vertex Detector System Test - Triggering and Data Analysis

Diploma Thesis

Universität Hamburg
Institut für Experimentalphysik

Ingo Bloch

Hauptstrasse 23 a
22145 Stapelfeld

Hamburg, November 2001

Abstract

During the shutdown of the electron proton collider HERA (at DESY, Hamburg) in winter 2000/2001 a new silicon strip detector (Micro-Vertex Detector, MVD) was installed in the ZEUS detector. Before the installation, a comprehensive test ("system test") of the MVD was carried out. The main aim of this test was to confirm the interplay and stability of all components of the MVD. A scintillator coincidence setup allowed to trigger on cosmic ray induced muons.

The design and construction of the scintillator setup and the analysis of the muon test data are the subjects of this thesis.

HERA and ZEUS are presented in the beginning. The layout of the MVD is presented. In the barrel MVD section, 30 ladders with 5 silicon modules each are arranged in three layers around the beampipe. In the forward section, the sensors are arranged in four rings (wheels) with 14 modules each.
The MVD system test is presented. The MVD and the readout chain were set up and tested in a hall on the DESY premises. The description of properties of cosmic ray induced muons precedes the detailed description of the scintillator coincidence setup. All components of this setup were tested and calibrated. The setup was integrated into the system test readout. It worked stable and reliably.

The analysis of the system test data shows comparable efficiency of the barrel and forward MVD section. The readout timing of both sections agrees within one nanosecond. Individual modules show maximal relative timing deviations of less than 8 ns. The response of the detector modules to minimal ionising particles yields the expected landau shape. The result of a study concerning the angular dependance of the signal height distributions was used to correct for the direction of incidence of the muons. The maxima of the corrected signal height distributions of all barrel section modules follow a Gaussian distribution. This corresponds to a distribution of the modules gain values with a relative width of 3%.

Further analyses show e.g. preliminary track residuals of better than 80 μm and a module efficiency of better than 97% in the barrel MVD section.

The muon data set was used for immediate analysis of the detector and will furthermore be used for quality comparisons with later data sets.

Zusammenfassung

Während der Betriebspause des Elektron-Proton-Beschleunigers HERA (am DESY in Hamburg) im Winter 2000/2001 wurde ein neuer Siliziumstreifen-Detektor (Micro-Vertex Detector, MVD) in das ZEUS-Experiment eingebaut. Vor der Installation wurde der MVD einem umfassenden Test (Systemtest) unterzogen. Dieser Test diente der Kontrolle des Zusammenwirkens aller Komponenten des Detektors. Ein Szintillator-Koinzidenzaufbau um den MVD ermöglichte die Aufzeichnung von Myonenereignissen aus kosmischer Strahlung.

Diese Arbeit beschäftigt sich mit dem Entwurf und der Konstruktion des Szintillator- Koinzidenzaufbaus sowie der Analyse der Myonen-Testdaten.

Einführend werden HERA und ZEUS kurz beschrieben. Der Aufbau des MVD wird ausführlich dargestellt. 30 Leitern mit je 5 Silizium Modulen sind in drei Lagen im "Barrel"-Bereich um das Strahlrohr arrangiert. Im Vorwärtsbereich sind die Sensoren in 4 Ringen mit je 14 Modulen arrangiert.
Der MVD-Systemtest wird beschrieben. Der MVD, sowie die Ausleseelektronik wurden in einer Halle auf dem DESY Gelände aufgebaut und betrieben. Die Beschreibung einiger Eigenschaften von Myonen aus kosmischer Strahlung geht der detaillierten Beschreibung des Szintillator-Koinzidenzaufbaus voraus. Alle Komponenten dieses Aufbaus wurden getestet und kalibriert. Der Aufbau wurde in die Systemtest-Auslese integriert und funktionierte stabil und zuverlässig.

Die Analyse der Systemtest-Daten zeigt vergleichbare Effizienz von Barrel und Vorwärts Bereich des MVD. Die zeitliche Abstimmung von beiden Bereichen des MVDs stimmt innerhalb einer Nanosekunde überein. Zwischen Modulen sind individuelle Abweichungen der Zeitabstimmung von weniger als 8 ns gefunden worden. Die Signalhöhenverteilungen der Myonen-induzierten Signale der einzelnen Module haben die erwartete Landau-Form. Das Ergebnis einer Untersuchung der Winkelabhängigkeit des Maximums dieser Verteilungen wurde verwendet, um auf die Einfallsrichtung der Myonen zu korrigieren. Die Maxima der korrigierten Signalhöhenverteilungen aller Module des Barrel-Bereichs folgen einer Gaussverteilung. Dies entspricht einer Verteilung der Verstärkungen der Module mit einer relativen Breite von 3%.

Weitere Analysen ergeben z.B. eine vorläufige Spurauflösung von besser als 80 μm sowie eine Moduleffizienz von besser als 97% im Barrel-Bereich.

Der Myonen-Datensatz diente der sofortigen Analyse des Detektors uns soll weiterhin zum Qualitätsvergleich mit späteren Datensätzen verwendet werden.

Contents

1 Introduction **9**

2 HERA and the ZEUS detector **11**

2.1 HERA 11

2.2 ZEUS 12

2.3 Physics at ZEUS 13

3 The ZEUS Micro-Vertex Detector (MVD) **17**

3.1 MVD physics and design goals 17

3.2 Detector layout 18

3.2.1 The barrel MVD 19

3.2.2 The forward MVD 22

3.3 Basic principle of silicon sensors / MVD silicon strip sensors 23

3.4 MVD readout 26

3.4.1 The front end readout chip 26

3.4.2 Readout chain (patchbox, ADC, C&C) 28

3.5 Module tests and resolution studies 29

4 Cosmic rays **31**

4.1 The signal source: cosmic rays 31

4.2 Energy loss by ionisation 32

4.2.1 Bethe-Bloch energy loss 32

4.2.2 Energy loss fluctuations 33

5 The scintillator trigger **35**

5.1 Trigger setup 35

5.2 Purposes of the different layers 38

5.3 Components . . . 38
5.3.1 Scintillators . . . 40
5.3.2 Electronics . . . 42
5.3.3 Tests, calibration and construction . . . 45
5.4 Performance . . . 50
5.4.1 Hit distribution . . . 50
5.4.2 Estimation of the expected rate . . . 51
5.4.3 Trigger efficiency . . . 52

6 The system test **55**
6.1 System test setup . . . 56
6.2 Slow control . . . 56
6.3 Run control . . . 58
6.4 The trigger and readout . . . 58
6.5 Detector checks . . . 63
6.6 Data taking . . . 63

7 System test data analysis **67**
7.1 Data preparation . . . 67
7.1.1 Investigation of bad channels . . . 68
7.1.2 Clustering . . . 68
7.1.3 Cuts . . . 69
7.2 Results . . . 71
7.2.1 Efficiency comparison of barrel and forward section . . . 71
7.2.2 Timing of barrel and forward section . . . 74
7.2.3 The effective angular dependance of the signal size . . . 74
7.2.4 Measurement of the gain distribution . . . 78
7.3 Related results of other analyses . . . 84
7.3.1 Pedestal stability . . . 84
7.3.2 The track resolution / track residuals . . . 84
7.3.3 Efficiency of the barrel modules . . . 84

8 Conclusion **87**

A The ZEUS coordinate system **89**

B Scintillator numbering scheme **91**

C Estimation of the angle of incidence: error estimation **93**

D The ntuple **95**

E Documentation of the code **97**

E.1 Data format 97

E.2 test.c ana.C / MvdAna 98

E.3 hexer 99

E.4 matcher 99

E.5 unhex 99

E.6 angler 99

E.7 no_shower 100

Chapter 1

Introduction

In winter 2000/2001 the ZEUS collaboration carried out a comprehensive test of a new Micro-Vertex Detector based on silicon strip sensors. This thesis focuses on the trigger setup for this test and on the test data analysis.

The ZEUS high energy physics experiment is located at the electron proton collider HERA at DESY in Hamburg. This experiment studies e.g. the structure of the proton, tests quantum chromo dynamics and searches for physics beyond the Standard Model.

The HERA collider was upgraded in 2000/2001. During this shutdown phase, the ZEUS detector was also upgraded by a new Micro-Vertex Detector (MVD) situated inside its central tracking detector.

Before the MVD was installed, a check of the complete detector, called system test, was performed. For this purpose, the detector and the readout components were set up in a hall on the DESY premises. The main aims of the MVD system test were to confirm the functionality and stability of the complete system as well as to record a reference set of cosmic ray test data.

A scintillator coincidence setup was developed and integrated into the MVD test setup. It was installed to trigger on cosmic ray induced muons.

About half the time spent on this thesis was used to develop and implement this scintillator coincidence setup. The other half was invested into the test data analysis.

The document is structured as follows. After introducing HERA and ZEUS and briefly summarising some physics topics of interest in chapter 2, the MVD layout, readout, principle of silicon detectors and some physics applications of the MVD are presented in chapter 3.
A short summary of properties of cosmic rays, used as a data source during the system test, is provided in chapter 4. A detailed description of the scintillator setup, electronics and performance is given in chapter 5. A summary of the system test is presented in chapter 6. The data analysis and results are finally explained in chapter 7.

Chapter 2

HERA and the ZEUS detector

2.1 HERA

The electron (positron) proton collider HERA was built to resolve the structure of the proton and to study the two underlying fundamental forces (electroweak and strong force). These forces mediate the observed processes and are described by the Standard Model. An other very important aim is to discover and study the nature of so far unknown interactions (beyond the standard model).
HERA consists of two large particle storage rings of 6.3 km circumference located at DESY, Hamburg (Fig. 2.1). Two pre accelerator machines (DESYII and PETRA), inject 14 GeV electrons (positrons) and 40 GeV protons into the two separate rings in the HERA tunnel, where they are further accelerated, stored and finally brought to collision.

HERA supplies 4 experiments with high energy particles. These experiments are placed at the 4 straight sections as seen in Fig. 2.1. At two of these experiments, H1 and ZEUS, e^- (e^+) bunches collide with proton bunches at a rate of 10.42 MHz. The other two experiments HERA-B and HERMES make use of only one beam, i.e. HERA-B uses the protons and HERMES the electrons (positrons).
The electrons (positrons) have an energy of 27.5 GeV, protons of 920 GeV, leading to a centre of mass energy of $E_{cms} \approx 318$ GeV (values for the 2000 data taking period).

Either positrons or electrons were used in alternation. From 1994 to 1998 and 1999 to 2000 positrons were used, electrons otherwise. From now, the high energy leptons will always be addressed as electrons.

An important parameter of a high energy collider is its luminosity. In 2000 the achieved peak luminosity of HERA was $\mathscr{L} = 1.97 \cdot 10^{31}$ cm^{-2}s^{-1} [1]. Knowing the luminosity $\mathscr{L}$ and the cross section σ_p for any process p, the event rate r_p is easily calculated:

$$r_p = \mathscr{L} \cdot \sigma_p \tag{2.1}$$

An extensive upgrade of the HERA accelerator, performed from autumn 2000 to summer 2001, will lead to a rise of the luminosity by a factor of 3.6, to reach $\mathscr{L} \sim 7 \cdot 10^{31}$ cm^{-2}s^{-1}. The higher luminosity will provide enhanced access to low cross section physics. A detailed description of the HERA upgrade is given in [2].

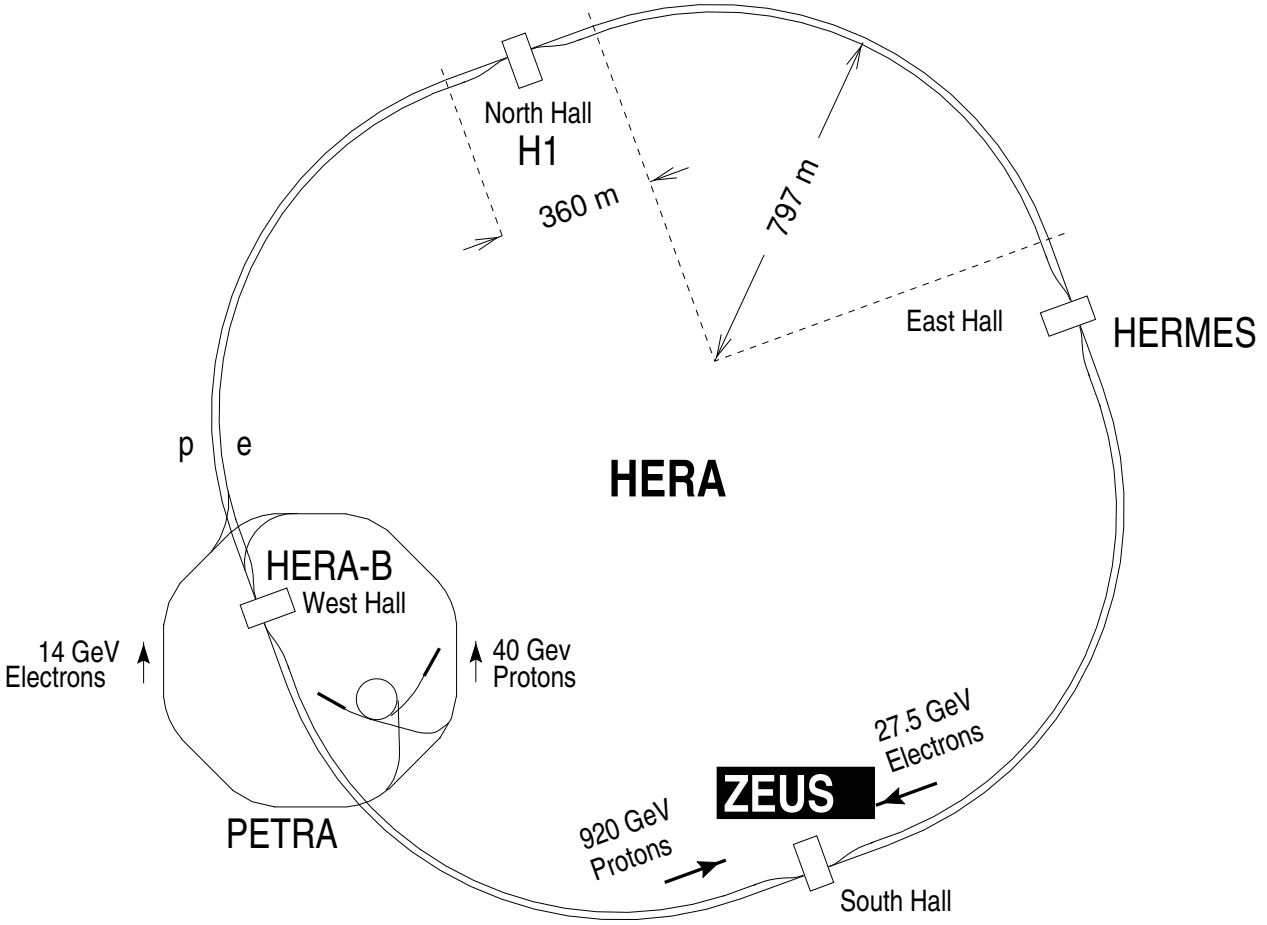

Figure 2.1: *The electron proton storage ring* HERA. *An experiment is situated at each straight section. While H1 and* ZEUS *make use of both particle beams,* HERMES *and* HERA-B *use only the electron and the proton beam respectively. In the lower left corner the pre accelerators are sketched.*

2.2 ZEUS

The ZEUS detector [3] is situated in the South Hall of the HERA ring. It mainly consists of tracking detectors, energy determining electromagnetic and hadronic calorimeters and an instrumented iron yoke. The layout of the ZEUS detector is shown in Fig. 2.2. Due to the asymmetric energy configuration of the colliding particles the centre of mass system moves in the positive z direction (proton direction) relative to the ZEUS detector. Therefore also the detector is asymmetric.

The tracks and momenta of charged particles in triggered events are measured mainly with the central tracking detector (CTD), a cylindrical wire proportional drift chamber surrounding the beam pipe. Making use of the magnetic field of 1.43 T inside the CTD, the momenta of the particles can be determined.
The CTD is made up of 72 cylindrical drift chamber layers subdivided into 9 super layers and covers an angular range of $15° < \theta < 164°$, where θ is the polar angle with respect to the proton direction (in the ZEUS coordinate system, the protons propagate in positive z direction, see Fig. A.1).

Additional tracking detectors are e.g. the Forward Detector, consisting of planar drift chambers and transition radiation detectors. The transition radiation detectors are being replaced by the so called straw tube tracker (STT), a tracking detector consisting of high precision proportional gas wire tubes.

The particle energy in the pseudorapidity range of $-3.8 < \eta < 4.3$ ($\eta = -\ln[\tan\frac{\theta}{2}]$) is determined using the high resolution depleted-uranium calorimeter, which is realised as a depleted uranium scintillator sandwich structure. It can be used to separate hadronic from electromagnetic energy depositions.

The instrumented iron yoke is used to identify particles leaving the detector (mainly muons).

The ZEUS coordinate system is shown in Fig. A.1. The z axis points along the proton direction, the y axis upwards and the x axis is directed into the centre of HERA with the point of origin at the nominal interaction point in ZEUS. Unless stated otherwise, all variables quoted are given in this coordinate system.

To further enhance the ZEUS detector, the ZEUS collaboration decided to install a new silicon vertex detector (Micro-Vertex-Detector, MVD) during the HERA upgrade shutdown. The vertex detector will improve the global precision of the tracking system and enable the study of secondary vertices originating from decays of long lived states ($c\tau \gtrsim 100$ μm) like hadrons containing charm or bottom quarks, or τ leptons.

2.3 Physics at ZEUS

The physics aims of the ZEUS experiment are to understand the processes and forces involved at high energy electron proton collisions, e.g. to resolve the structure of the proton and to measure the underlying interactions in a previously untested kinematic range[1].
Different types of processes in ep collisions have been defined. One of these, called deep inelastic scattering by neutral current (DIS, [4]), refers to events with a scattered electron and hadrons in the final state and seen in the detector:

$$ep \rightarrow eX \tag{2.2}$$

These processes are characterised by e.g. high momentum transfer ("deep") and a high mass of the hadronic system ("inelastic"). The events are interpreted such that the electron interacts with one parton of the proton via the exchange of a photon or a Z-boson.

Apart from measuring free Standard Model parameters like the strong coupling constant α_s or the $W^{\pm}$ mass (mainly from charged current events which have not been described), ZEUS significantly contributed to the determination of the parton density functions by measuring the proton structure functions F^i. These describe the structure of the proton in general and can be interpreted as the distribution of the partons inside the proton.

The study of events with heavy flavour particles in the final state is another sector of activity in the ZEUS collaboration. It concerns mainly charm and bottom, as well as tau physics.

[1] Fundamental knowledge concerning the Standard Model is assumed. An introduction is given by D. Griffiths. [5]

The main leading order charm and bottom quark production mechanism at HERA is photon gluon fusion. This process can be used to measure the gluon density of the proton. However, a large fraction of the cross section arises from other more complicated processes, including reactions were the photon fluctuates into a hadronic state before it interacts, and higher order QCD processes. Currently perturbative Next-to-Leading order QCD calculations seem to systematically underestimate the measured cross sections. The clarification of this phenomenon is one of the primary goals of future analysis.

ZEUS, without the MVD, is able to detect events containing heavy flavour particles e.g. by reconstructing D^* mesons to identify charm events or by finding muons or electrons from the decay of bottomed mesons. These methods, however, result in rather low efficiencies or low purities and the analysis of most of this data is still dominated by statistical errors. The usage of the MVD will yield high-purity and, by improved efficiency, large statistics samples, e.g. by introducing the option to measure the impact parameters of reconstructed particle tracks and determining secondary vertices, see Fig. 2.3, which can be used to find heavy flavour events efficiently. Results of Monte Carlo (MC) studies on purity and efficiency for charm identification including the MVD are shown in Fig. 2.4. These studies are based on an early design version of the MVD. The amount of material for multiple scattering was somewhat underestimated and the final geometry of the MVD was not simulated. Still, this plot gives a rough approximation of the performance of ZEUS with the MVD.

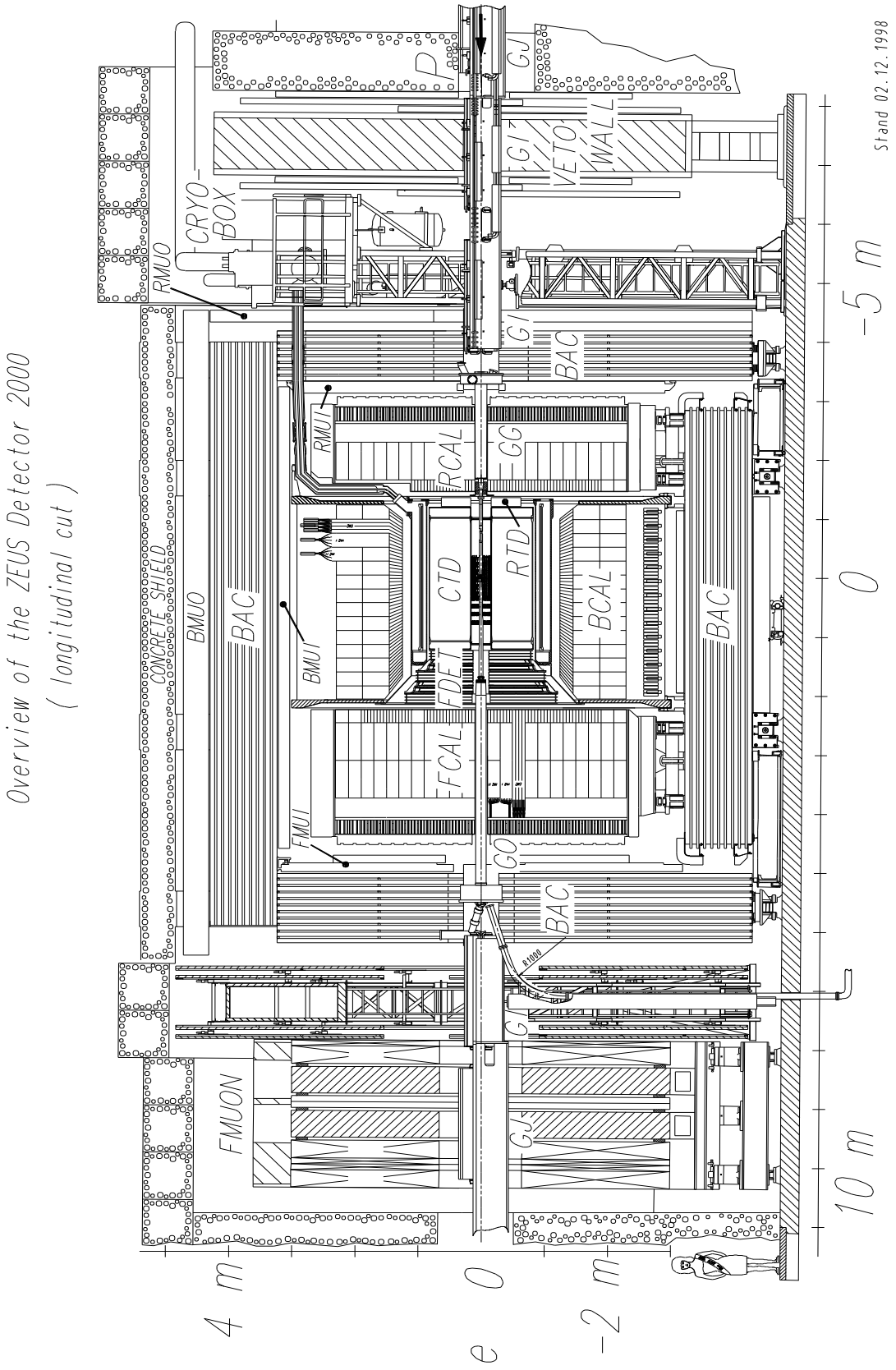

Figure 2.2: *Longitudinal cut through the* ZEUS *detector after the luminosity upgrade. A detailed description of all components of the detector is given in [3].*

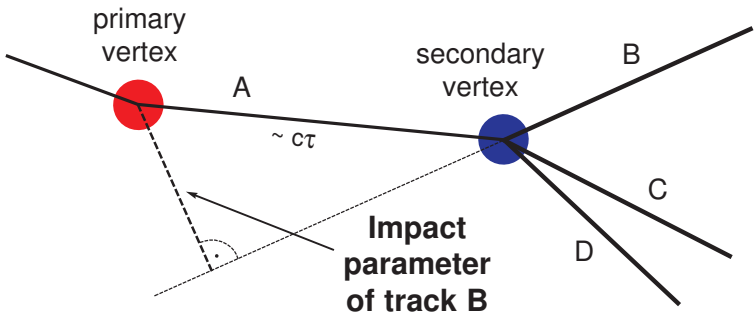

Figure 2.3: *A sketch of an event with a secondary vertex is shown in an arbitrary coordinate frame. Particle A with a lifetime τ decays to the particles B, C and D. The impact parameter of the track B is indicated by the dashed line.*

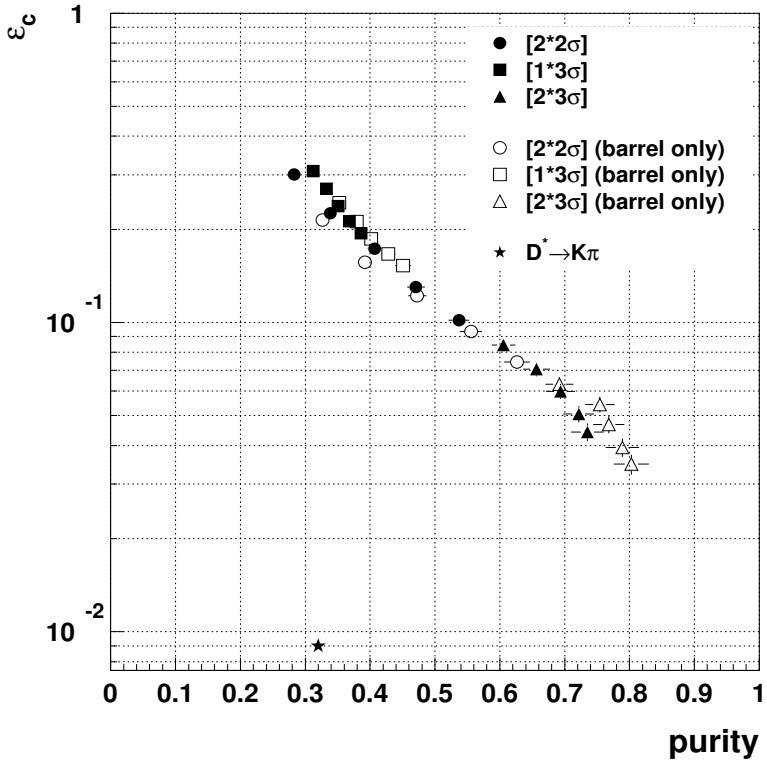

Figure 2.4: *Purity versus efficiency for different selection criteria of charm in deep inelastic scattering using the* MVD *(*MC *not for final design). As a reference point, the star shows the values obtained with the* ZEUS *tracking system by tagging a D^* [6].*

Chapter 3

The ZEUS Micro-Vertex Detector (MVD)

This section describes the design of the MVD, as well as its basic functionality. All components of the detector will be presented in some detail.

The MVD is situated at the centre of the CTD and therefore at the centre of the ZEUS detector. The empty space inside the CTD ($\varnothing = 324$ mm) is well filled by the MVD with an outer diameter of 319 mm. The innermost MVD silicon module comes as close as 4.4 cm to the electron and proton beams. The MVD covers the complete φ range and 7° to 175° in θ.

The resolution of the event vertex, the track acceptance towards the forward direction, as well as the momentum resolution of ZEUS is enhanced by the MVD. This offers an extended approach to e.g. studies of long lived particles (heavy quark states, taus, etc.).

3.1 MVD physics and design goals

Possible physics topics, as quoted in the MVD construction proposal to DESY [6], that can be accessed using the MVD are:

- Charm in photoproduction[1]. From the rate of charm events in direct photoproduction, the gluon content of the proton, from resolved the charm content of the photon can be determined. The transition from direct to resolved processes can be studied.

- Charm in deep inelastic scattering. The measurement of the charm structure function F_2^{charm}, which provides an important insight into the gluon density, can be improved.

- Beauty production. Currently perturbative Next-to-Leading order QCD calculations seem to systematically underestimate the measured beauty cross sections (at HERA [7, 8]). More precise measurements and improved calculations will help to clarify this puzzle and should yield important further tests of QCD, e.g. concerning the influence of the hard scale introduced by the heavy quark mass.

[1] High energetic quasi real photon proton collisions. In "direct" events, the photon does not fluctuate into a hadronic state before it interacts, in "resolved", the photon does fluctuate before the interaction.

- New physics. The knowledge about secondary vertices will potentially be a great help to understand the underlying interaction of any anomaly found at HERA.

To optimise the detector design to reach the physics goals several studies were performed. For example to tag charm events efficiently in a large rapidity region an impact parameter resolution of the order 100 μm or better is required (see Fig. 2.3, $c\tau$ values for charmed mesons are e.g. 315 μm for $D^{\pm}$ or 123.7 μm for D^0).

Further important parameters are:

- polar angular coverage of $10° - 170°$
- three spatial measurements, in two projections each, per track
- intrinsic hit resolution of 20 μm
- noise occupancy $< 10^{-3}$
- hit efficiency > 97 %
- alignment accuracy 20 μm
- two track separation 200 μm

For further details please refer to the MVD technical design report / proposal [6].

3.2 Detector layout

According to the design goals, the MVD has been divided into 3 sections:

Forward • Barrel • Rear

Fig. 3.1 shows a view of the bottom half of the MVD, cut in half in the xz-plane.

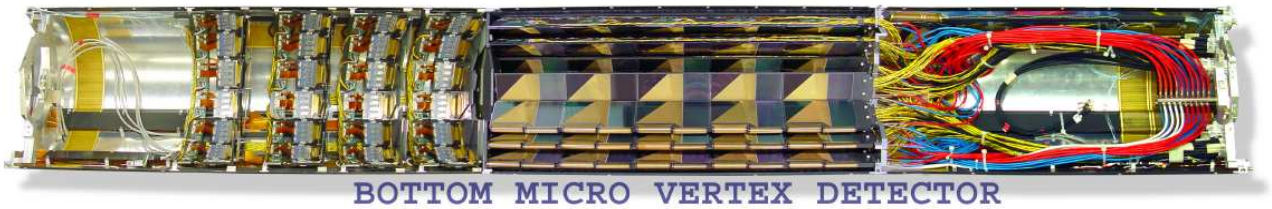

Figure 3.1: *The bottom half of the* MVD. *Inside the cylindrical support structure the silicon sensors are arranged. On the left is the forward section containing trapezoidal shaped sensors arranged in 4 "wheels", in the centre the barrel section with square sensors arranged in modules on the "ladders" and at the right the rear section (with space for cable and cooling connections) can be seen.*

The forward section holds 4 wheels. Each wheel consists of a double layer of 14 trapezoidal silicon strip sensors, arranged perpendicular to the beam pipe (see section 3.2.2). The barrel

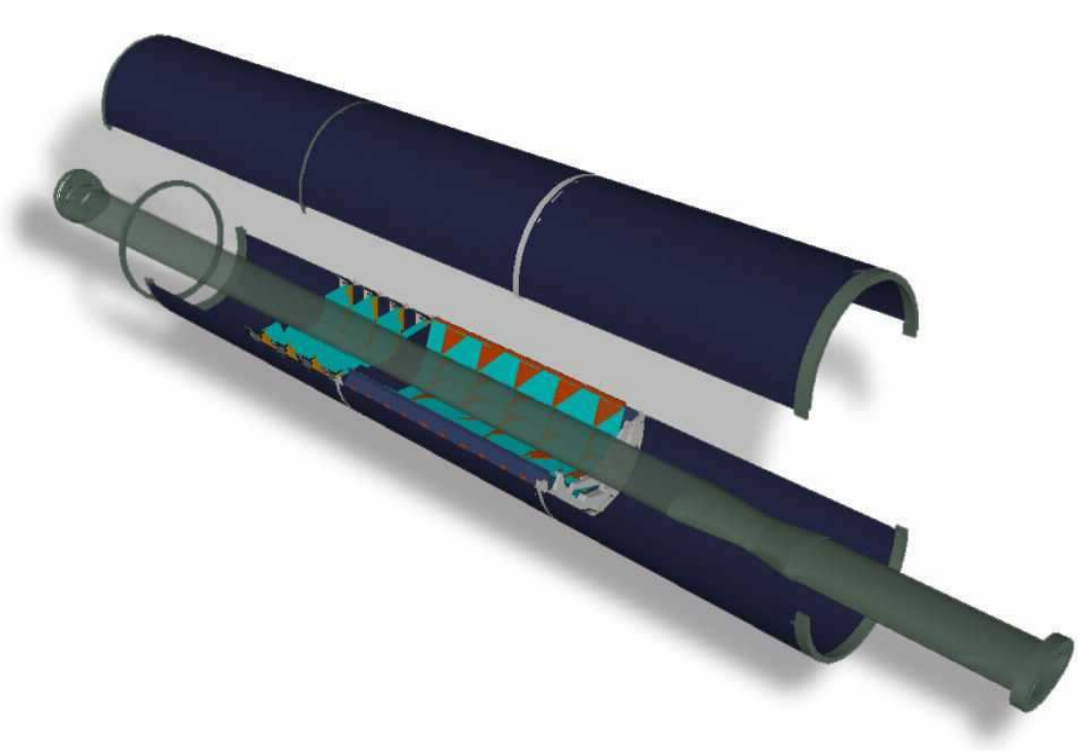

Figure 3.2: *Schematic view of the final assembly step of the* MVD. *The beam pipe was carefully inserted into the bottom half. Then the* MVD *was closed and sealed.*

section consists of 30 ladders arranged in 3 layers along the z axis around the beam pipe. Each ladder contains a double layer of 10 square silicon sensors (see section 3.2.1).

In Fig. 3.2 the final assembly step of the MVD is shown. The two halves were closed around the new elliptical beam pipe before the complete detector was intensively tested.

3.2.1 The barrel MVD

The barrel section of the MVD is presented in the following way: starting with the basic components, the silicon sensors, the barrel section is "assembled" and every new part is described until completion.

Sensors:

The basic components of the barrel are the 6.42×6.42 cm $\times$ 320 μm **silicon strip sensors**. Each sensor has 512 readout strips with 5 intermediate strips to enhance the position resolution. Fig. 3.3 shows a photograph of a silicon sensor. The brighter lines seen on the photograph are bond pads to electrically contact the readout strips. Schematic cuts through the sensor are shown in Fig 3.9 and Fig 3.10. The sensors are described in more detail in section 3.3.

Half modules:

Two sensors are glued together and are electrically connected[2] strip by strip by special cables

[2]by wire bonding

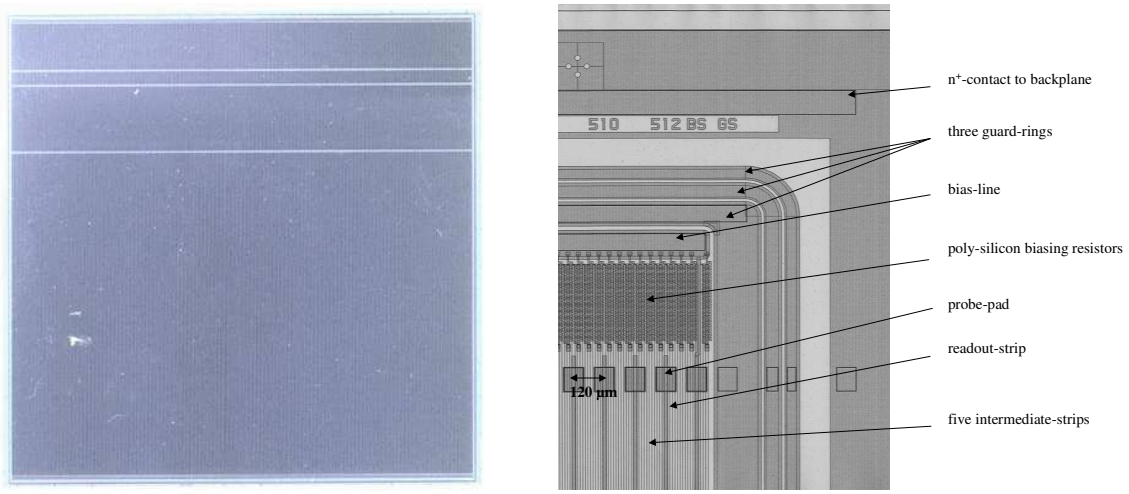

Figure 3.3: *On the left, a photograph of the strip side of a* 6.42×6.42 *cm silicon sensor. The brighter horizontal lines are strip contact pads. Here the sensors are electrically connected to each other and to the front end readout electronics. On the right, an enlarged view of the detectors corner is shown.*

(UPILEX[3]) to form a half module. The resulting sensitive area is approximately 60×120 mm; a small overlap (1.26 mm) between the two attached sensors is realised to reduce the dead area. The second sensor in the half module is rotated by 90° with respect to the first one. Thus the strips of the first one are perpendicular to the ones of the second. Another UPILEX cable connects the half module to a printed circuit board ("Hybrid") containing 4 readout chips (HELIX 3.0) (see Fig. 3.4). The readout chip is described in more detail in section 3.4.1.

The strips of two sensors are read out by the same electronics, reducing the number of required readout channels by a factor of two. This however leads to an ambiguity in the hit position. A hit detected in a half module may be on the first *or* on the second sensor (called "real hit" and "ghost hit", see Fig. 3.4b). This ambiguity is resolved later at the level of the track fit.

Modules:

Two kinds of half modules (see Fig. 3.4a) are glued together to form a module; one being a "mirror image" of the other. The strips of the sensors in the one half module are thus perpendicular to the ones of the other half module. Fig. 3.4b shows a schematic view of a module assembly. A particle passing through a module produces a signal in both half modules, yielding two possible hit positions.

Ladders:

Five modules are fixed to a carbon fibre support structure (also providing water cooling for the electronics attached to the rear side of the structure) to form a ladder with a length of approximately 660 mm of which 622 mm are covered by detectors. The modules are arranged in a row, with a 1 mm gap between them. A completely assembled ladder is shown in Fig. 3.5a.

The barrel MVD assembly:

30 ladders are arranged in 3 layers (cylinders) around the elliptical beam pipe. Fig. 3.6 shows a cut in the $r\varphi$-plane through the MVD; for clarity only the sensors are shown. A zy cut is

[3]On a copper coated Kapton® foil, gold plated copper conduction lines are arranged to form this cable.

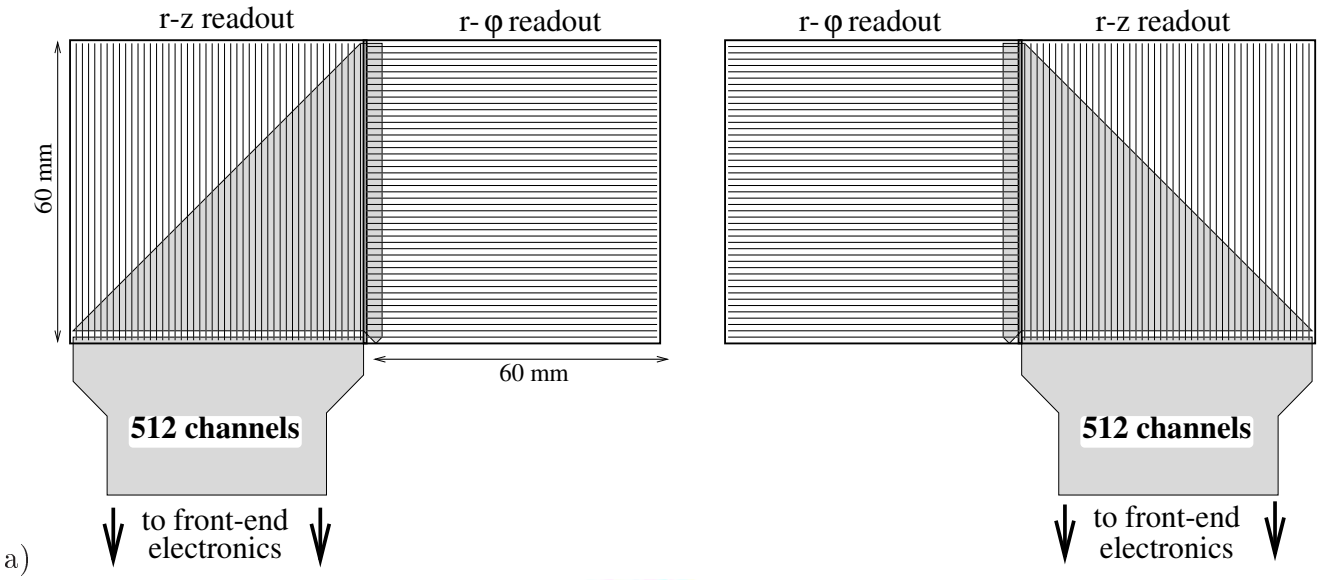

a)

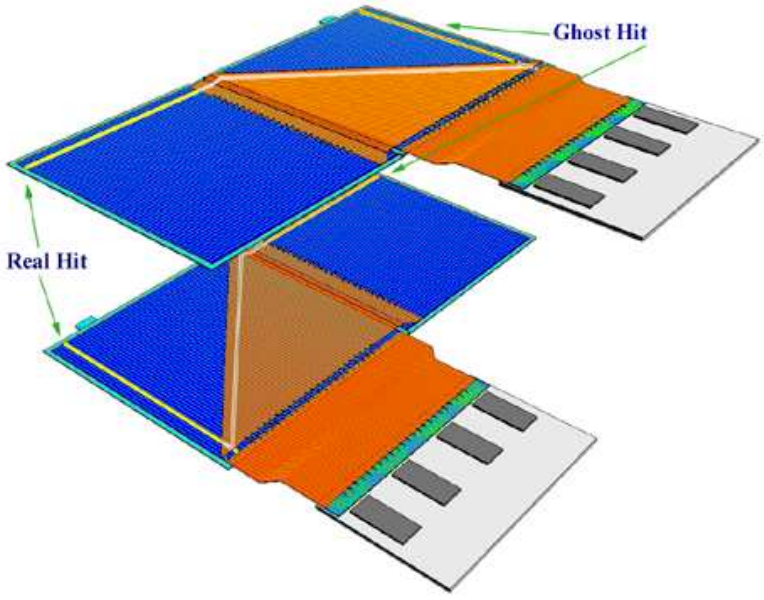

b)

Figure 3.4: *a) Two half modules. Notice the relative orientation of the strips in the sensors, which enclose an angle of 90°. The electrical connection of the $r\varphi$-sensor strips with those of the rz-sensor leads to a hit ambiguity (a ghost hit for each real hit). b) Mirror like halfmodules are placed on top of each other. The bright lines indicate the real and the ghost hit produced for each particle passing the module.*

shown in Fig. 3.7b.
The strips of the sensors are either parallel or perpendicular to the z direction; the parallel ones measure the $r\varphi$, the perpendicular ones the rz coordinates.
The length of the ladders has been chosen such, that despite the variation of the ep interaction point along the z axis, the events are well measured within the MVD. The variation is mainly due to the longitudinal extension of the proton bunches.

The elliptical shape of the beam pipe was chosen to prevent direct synchrotron radiation from hitting the beam pipe.

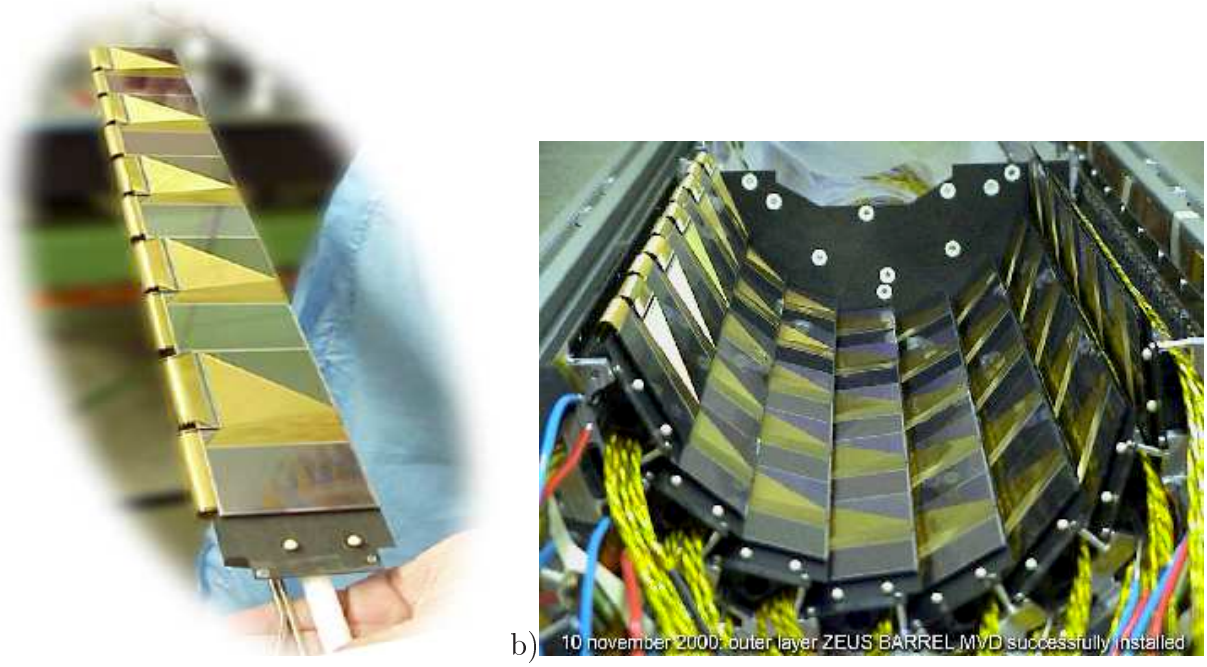

Figure 3.5: *a) An assembled ladder before installation into the support structure. b) The outer half layer of ladders is installed in the support structure. The cables in front (so called Combo cables) connect the front end electronics to the read out and power supplies.*

The innermost cylinder covers $\sim 75\%$ of the φ range and varies in distance from 4 to 6 cm relative to the CTD axis. The outer cylinders cover the full φ range and have a radius of 8.6 cm and 12.3 cm respectively.
The ladders of the innermost cylinder are placed as close to the beam pipe as possible. The ladders of the outer two cylinders are arranged at an angle of 36° for the inner and 22.5° for the outer layer with respect to each other (see Fig. 3.6). Only one ladder of the middle cylinder had to be rotated an extra 3° to fit around the beam pipe.

3.2.2 The forward MVD

The forward section of the MVD extends the forward acceptance of ZEUS and provides essential vertex and tracking information in regions not covered very well by the existing tracking system.

The sensors of the forward section are similar to the ones used in the barrel section. The material and the strip pitch is the same, but the wheel sensors are of trapezoidal shape. 480 instead of 512 strips per wheel sensor are read out. There are 2 kinds of sensor, differing in length to optimally cover the forward region around the beam pipe.

A double layer of 14 sensors is arranged in a ring, perpendicular to the beam pipe to form a wheel, Fig. 3.8b. The equivalent of a module of the barrel section is shown in Fig. 3.7a. The angle between the readout strips of the inner and outer sensors of one wheel is $\sim 26°$. Water cooling for the frontend chips is located on the inside of the carbon fibre support wheel. The four wheels are placed in the forward direction at $z_i = 33,\ 44,\ 57$ and 72 cm distance from the nominal interaction point.

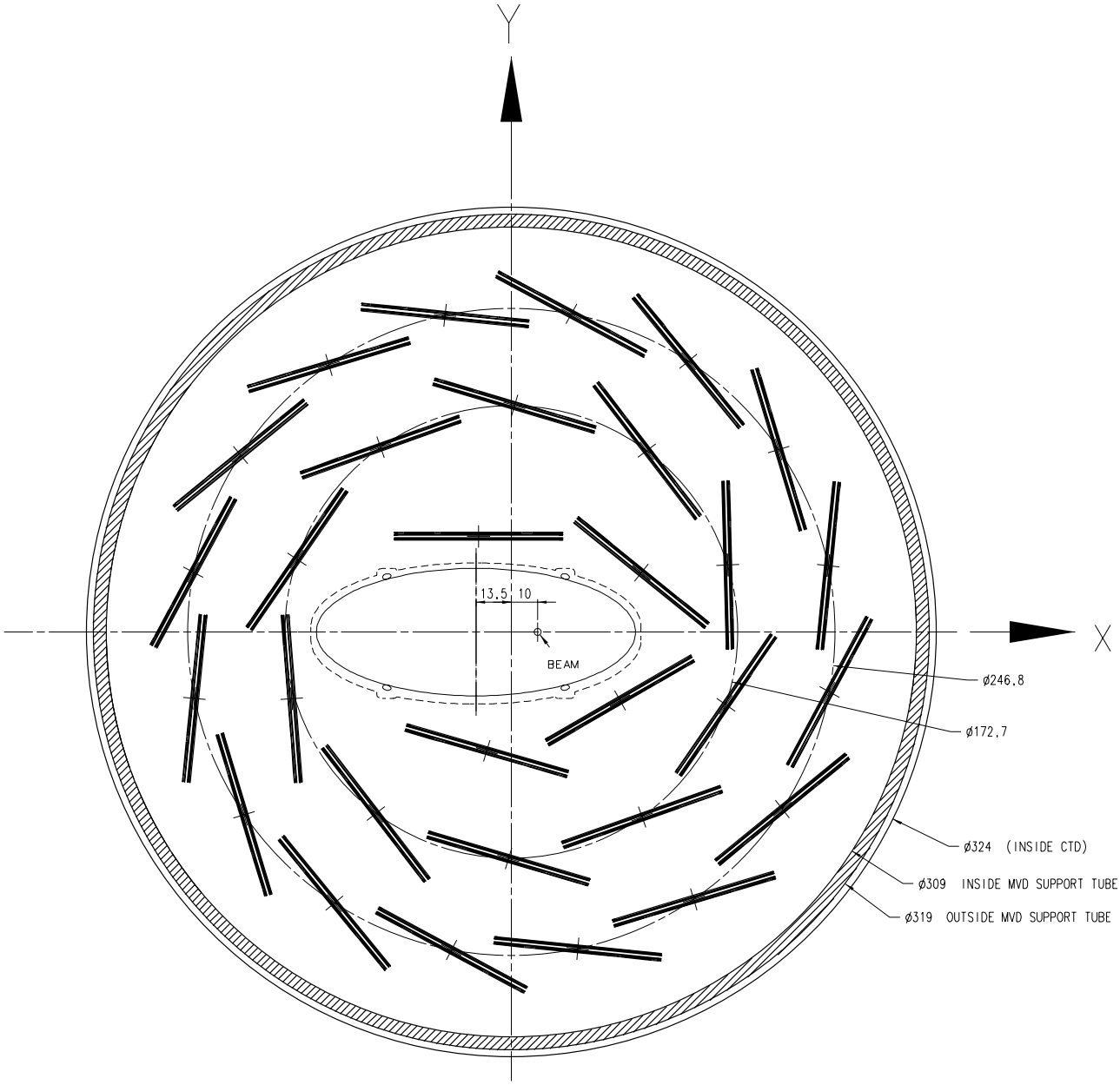

Figure 3.6: *A $r\varphi$ cut of the* MVD *barrel section. View in negative z direction. For details see section 3.2.1.*

3.3 Basic principle of silicon sensors / MVD silicon strip sensors

Silicon pn diodes are widely used as particle detectors [9]. The principle of operation is simple - a silicon detector can be considered as a solid state ionisation chamber.
Ionising particles traversing the silicon diode produce electron hole pairs in the detector volume by exciting electrons from the donator states and the valence band to the conduction band. To be able to detect these free charge carriers, the silicon diode is reversely biased e.g. by applying positive voltage to the n doped side of the diode and setting the p side to ground potential.

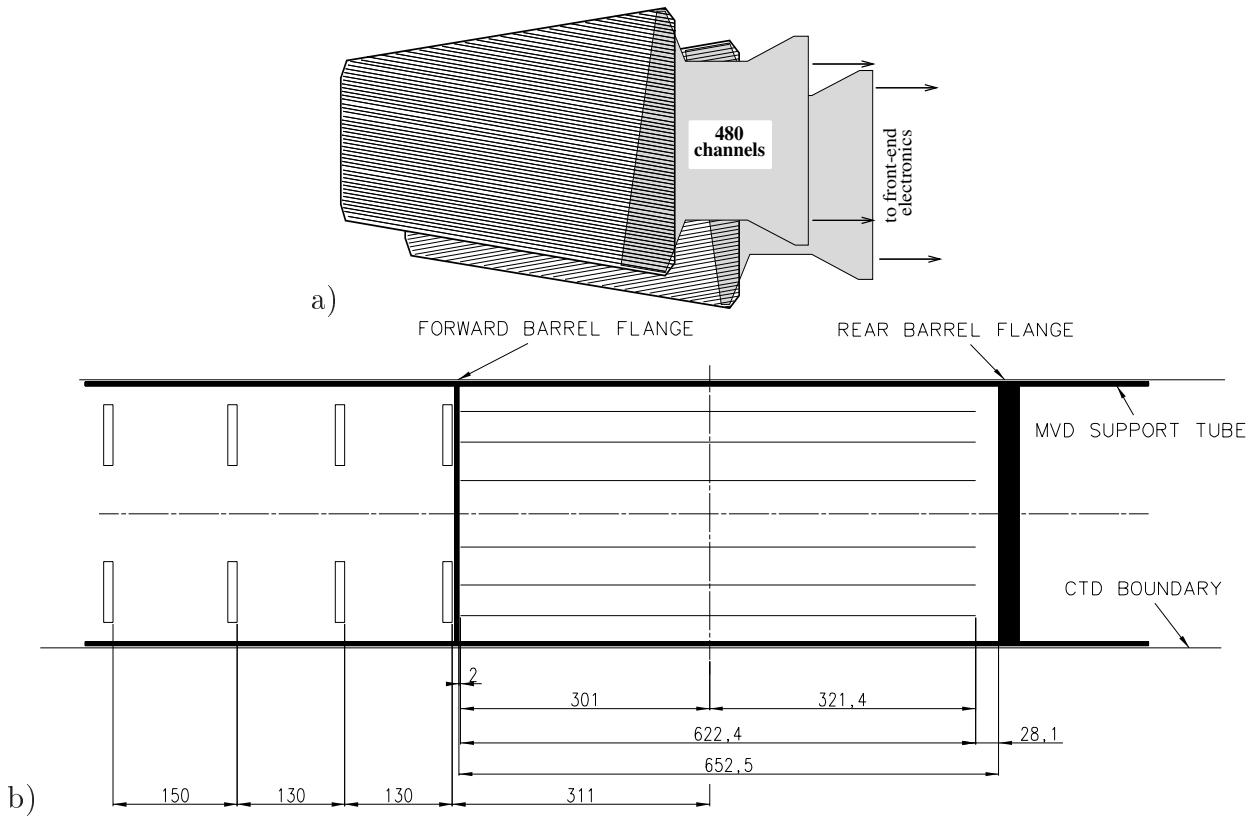

Figure 3.7: *a) Sketch of two trapezoidal silicon sensors of a wheel forming the equivalent of a module. The strips are inclined at an angle of* 26° *relative to each other. The front end readout board (hybrid) containing the 4 readout chips (*HELIX*) is not shown. b) A zy cut through the* MVD*. On the left hand side the 4 wheels can be seen. The support structure is sketched in thick black lines.*

This draws the free charge carriers in the material (due to thermal excitation and the doping concentration) out of the detector volume. The value of the bias voltage at which the volume with no free charge carriers reaches its maximum is called "depletion voltage".
If ionising particles traverse the depleted detector volume, the produced electron hole pairs are separated and drift along the potential gradient towards the electrodes, where they can be read out. In a 300 μm thick silicon diode a perpendicularly passing minimal ionising particle produces about 24000 electron hole pairs.

The current flowing in a reversely biased state in absence of ionising particles, called the "dark current", contributes to the noise together with the electronics.

For the MVD sensors, 300 μm thick, high resistivity n doped silicon serves as the sensitive volume of the sensors. p^+ doped strips (3082 in the case of the barrel MVD sensors) on the front side of one sensor collect the charge carriers produced by the ionising particles, see Fig. 3.9. The backplane is n^+ doped and contacted by an aluminium coating.

Every 6^{th} strip is AC coupled to an aluminium strip placed above the p^+ strip. These aluminium strips are directly connected to the readout electronics, thus in the case of the barrel modules 512 strips are read out, called readout strips.

All strips are separated at a pitch of 20 μm, leading to a readout strip pitch of 120 μm. The

a) 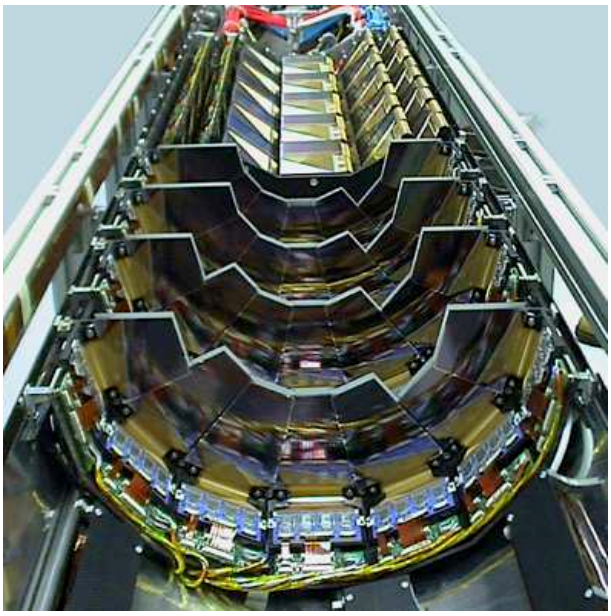 b) 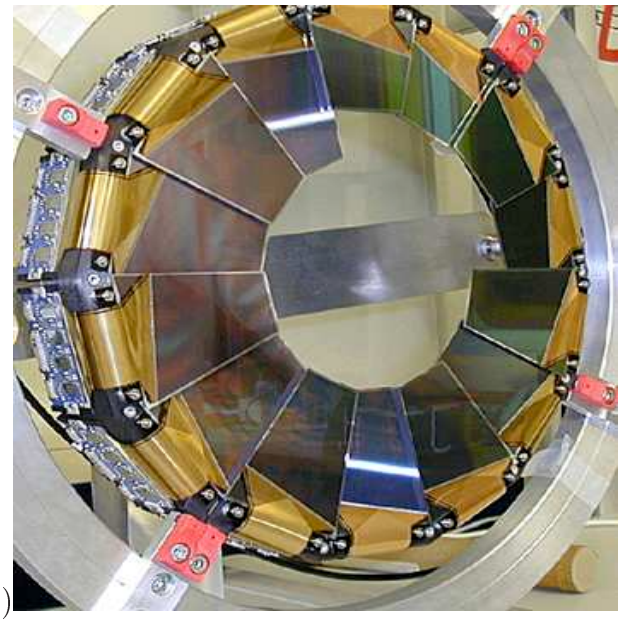

Figure 3.8: *a) A completely assembled wheel before it was installed in the* MVD *support structure. Some sensors are shorter than the rest to fit around the beam pipe. Clearly visible are the two planes of sensors in this wheel. The readout strips of the planes are inclined relative to each other at an angle of approximately* 26°*, allowing a 2 dimensional hit position reconstruction. b) View of the top half of the* MVD *after the wheels had been installed. One can clearly distinguish the 2 planes of silicon per wheel.*

5 intermediate strips contribute to the signal by transferring the signal to the readout strips via capacitive charge transfer. The sides of the strips act as capacitor planes, the material in between two strips as the dielectric material. The capacitive charge transfer is position dependent [10, 11]. By exploiting this position dependance during the hit reconstruction the resolution becomes as good as $\mathcal{O}(10\ \mu\text{m})$ for perpendicular incidence, see Fig. 3.14.

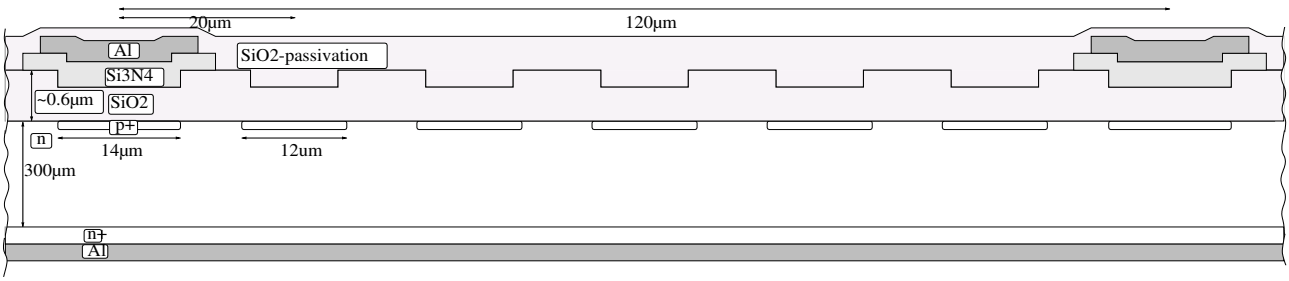

Figure 3.9: *A schematic cut through a* MVD *diode is shown. On the left and the right* 2 *of the* 512 *readout strips can be recognised by the aluminium contact above the* p^+ *doped readout strip. The aluminium pad on the back of the sensor is used to electrically contact the device.*

The depletion voltage is applied by connecting the n^+ doped, aluminium coated backplane of the detector diodes to a positive potential and the readout strips to ground potential. Fig. 3.10 shows a cut (roughly to scale) through a MVD sensor. An inclined track of a particle passing the sensor with an exemplary $e^- h^+$ pair is sketched to illustrate the signal origin.

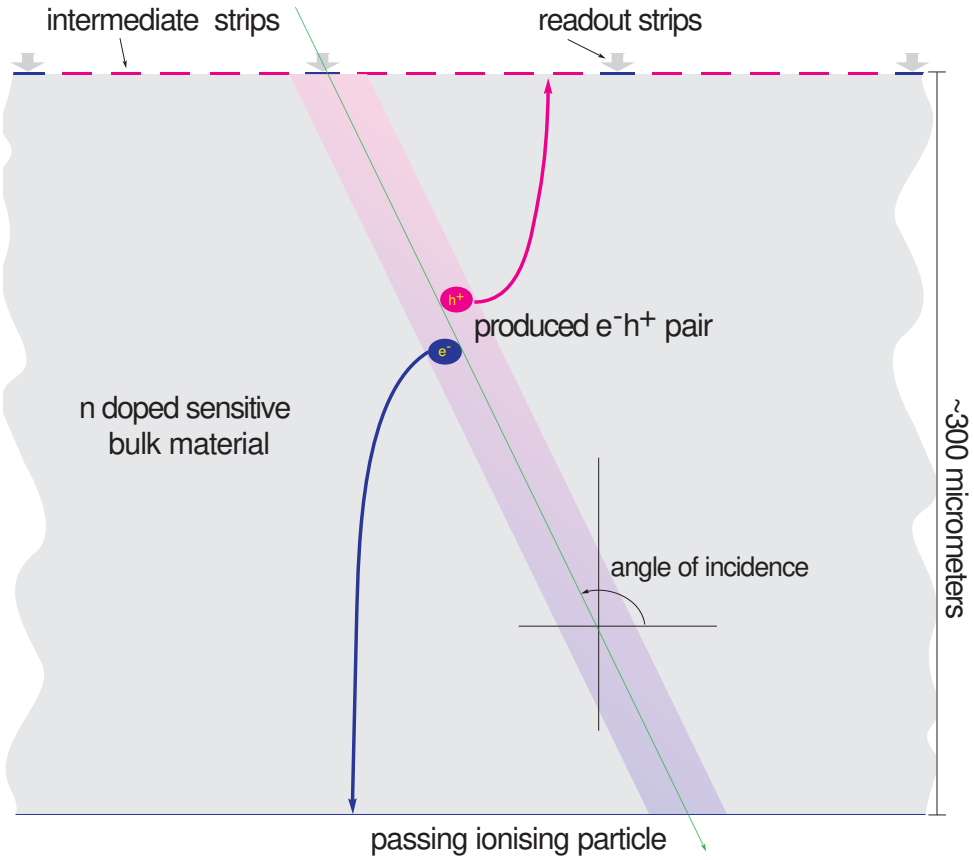

Figure 3.10: *Electron-hole production by a passing ionising particle in the depleted volume of the silicon detector (sketch roughly to scale). The readout strips lead the signal to the readout electronics where it is amplified, shaped and stored in a 128 clock counts long buffer.*

3.4 MVD readout

The front end readout chip of the MVD, as well as the subsequent readout chain is described in this section.

3.4.1 The front end readout chip

The front end analogue readout chip for the silicon diodes of the MVD is the HELIX 3.0 chip [12] designed by the ASIC laboratory (Heidelberg) and the NIKHEF Institute (Amsterdam).

One chip integrates 128 readout channels of the MVD silicon sensors, so 4 chips are required for each half module. Each of the 128 channels consists of an amplifier, a shaper and a pipeline buffer (128×96 ns long). A multiplexor is used to subsequently transmit the stored signals to the ADCs following a trigger signal. A circuit diagram of one channel of the HELIX chip is shown in Fig. 3.11.

Signals from the sensor are amplified by the preamplifier whose gain can be adjusted by varying the current I_{pre}. After amplification and shaping, the charge signal induced on the aluminium readout strip has the shape shown in Fig. 3.12.

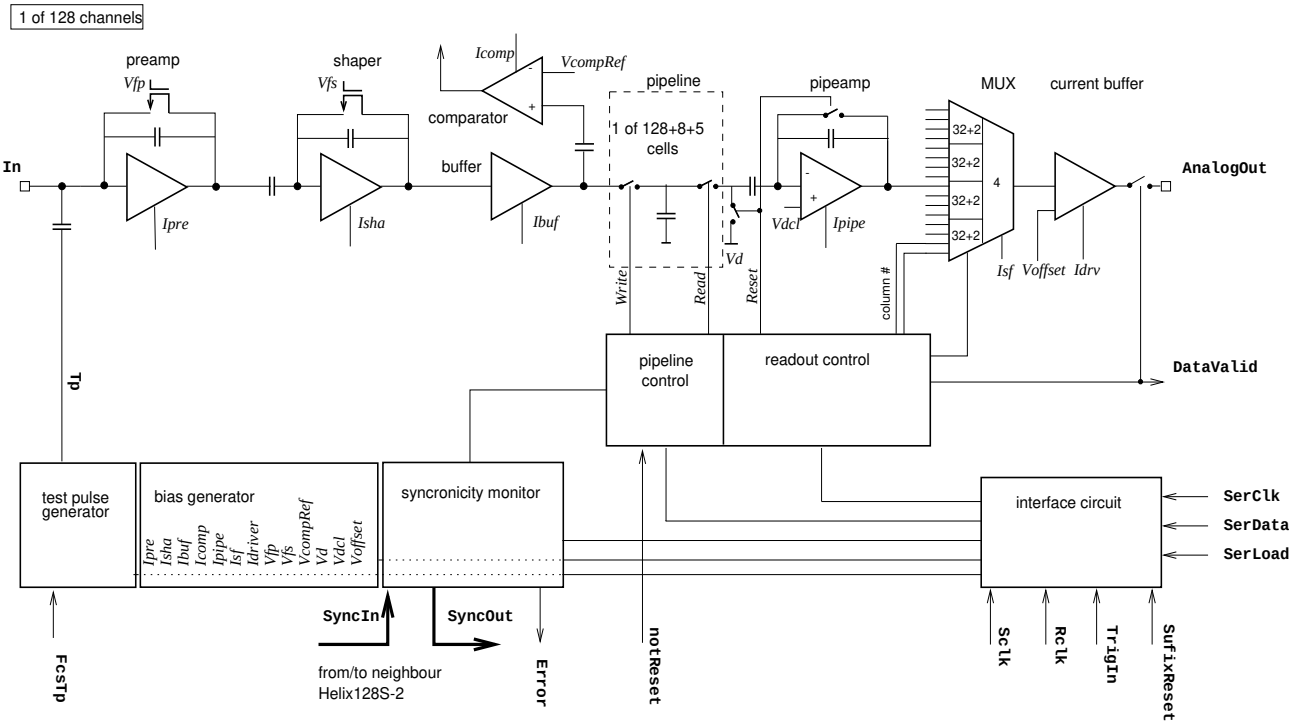

Figure 3.11: *A circuit diagram of one channel of the* HELIX *[12]. The* HELIX *readout chip integrates 128 readout channels. Each channels signal is amplified, shaped and stored in a* 128 *by* 96 *ns long pipeline buffer. Following an trigger signal, the pipeline signals of the required buffer slot are multiplexed and send to the* ADCS*.*

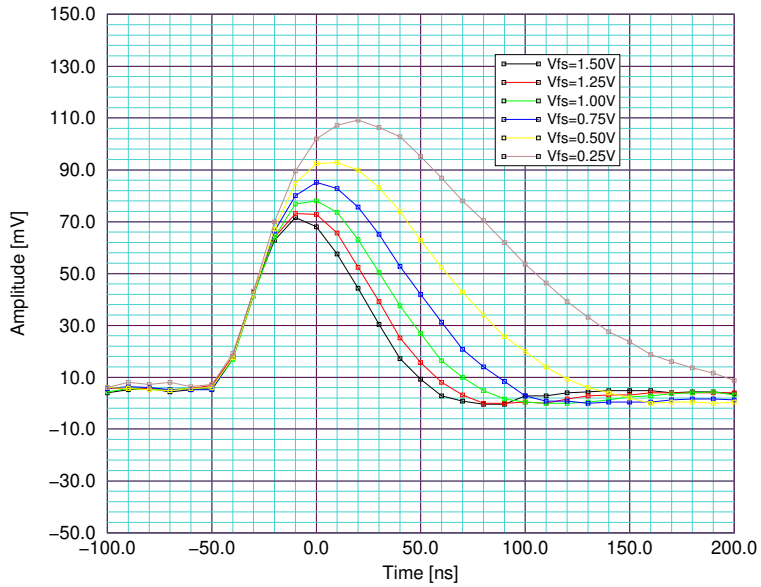

Figure 3.12: *The shape of a pulse after it has passed the shaper of the* HELIX *for different shaper settings [12].*

The time at which the signal value[4] is stored in the pipeline buffer is synchronised with a clock signal. In the HERA environment this clock signal is provided by the accelerator and is in phase with the bunch crossings.
When the first of the three trigger levels of ZEUS signals an event of interest, the MVD receives a signal and the pipeline buffers of all channels of the HELIX chip corresponding to this event are transmitted to the further readout using the fast (40 MHz) multiplexor.

3.4.2 Readout chain (patchbox, ADC, C&C)

The MVD has to be supplied with the necessary electrical power for all electronic devices, as well as with cooling water. All data emerging from the MVD has to be read out, digitised, filtered and stored. This section briefly describes the most important components of the readout and supply chain connected to the MVD.

Fig. 3.13 shows a sketch of the readout chain. The HELIX chips in the MVD as well as the diodes and further supervisory sensors (monitoring e.g. temperature, humidity) are connected via the so called Combo cables. These are short - ~ 6 m, to prevent loss of performance - and compact - to fit through the ZEUS detector - shielded cables.

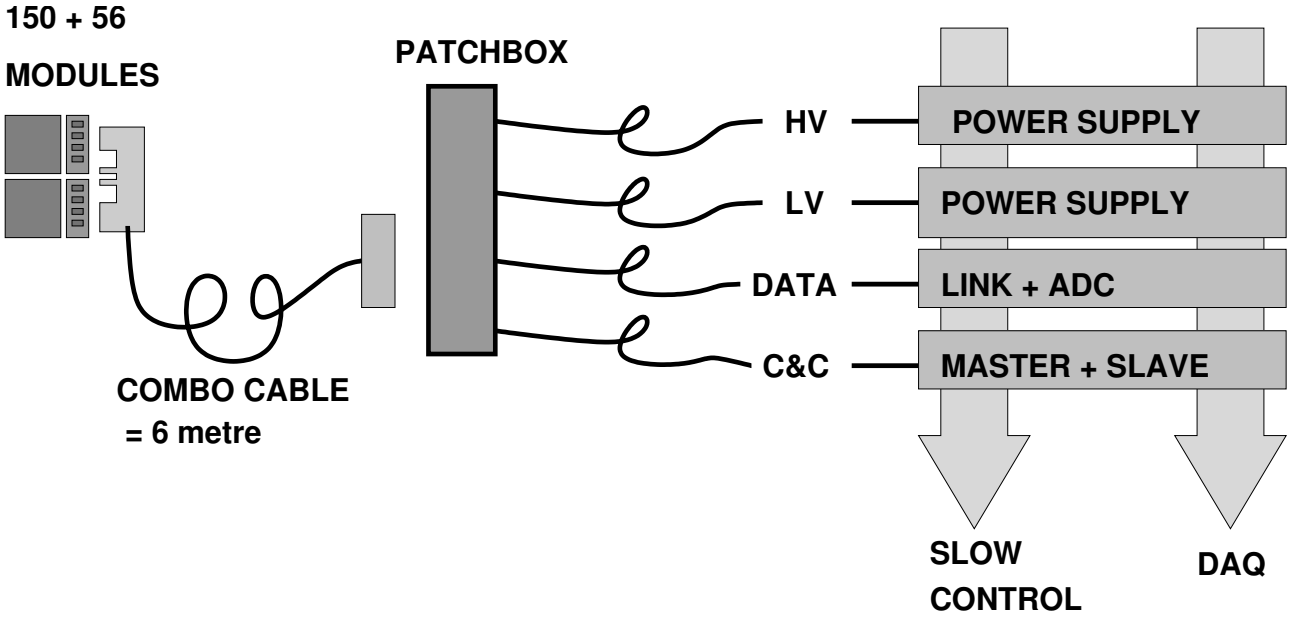

Figure 3.13: *A symbolic sketch of the most important parts of the readout chain is shown. At the left side a module can be seen. The module is connected to the patchboxes via the compact and short Combo cables. From the patchbox onward the electrical connection to the readout crates is realised by separate* ≈ 25 *m long cables.* HV *and* LV *stand for high and low voltage supply lines. The data are led to the* ADC*'s. The clock and control master board communicates with the readout chips via the C&C line. Computers connected to the readout crates run the Slow control and data acquisition (*DAQ*) routines.*

They are connected to 4 patchboxes, located close to the MVD. 5 Combo cables are enclosed by an additional protective shielding tube, called "zipper tube". The zipper tube is electrically

[4]The signal value stored corresponds to the voltage level of the shaper at readout time.

connected to the MVD shielding as well as to the patchbox shielding. Through the patchboxes the Combo cables are interfaced into larger and longer cables ($\sim$ 30 m) connected to the readout electronics racks. The control signals from the detector are converted to LVDS (low voltage differential signal) at the patchboxes as well. LVDS is a signal standard well suited for fast, long distance transmission.

ADC

The raw data of the MVD is transmitted up to the analogue to digital converters (ADC) [13] in analogue form. The ADCs convert the analogue signal to digital form. Additionally they subtract

- the common mode (mean signal height of all strips (no events), i.e. averaged and subtracted per HELIX chip)
- and strip wise pedestals (mean strip wise signal height (no events), i.e. averaged over several readout values).
- The ADC is able to reduce the amount of data by applying a cluster algorithm and only saving those strip addresses and signals, which have been found to contribute to a cluster (A cluster is a pattern of strips meeting certain requirements indicating particle passage, see section 7.1.2). A strip-wise noise cut and a minimal cluster signal height (cluster sum) introduced at ADC level further reduces the data volume.

Clock & Control

The 'Clock part' of the Clock&Control (C&C) master board (controlling 2 further slave boards) distributes the HERA clock signal ($\sim$ 10 MHz), providing the temporal point of reference for the *ep* collisions (electron proton bunch crossings) and the trigger signal.
All control commands for a single HELIX chip (e.g. preamplifier current, readout timing settings) can be sent to the C&C which sends them to the corresponding chip through further HELIX interfaces.

3.5 Module tests and resolution studies

Before and while the MVD was constructed, many tests and studies concerning the detector performance were carried out. Some of these shall be mentioned here.

- During the production phase of the modules of the detector, all components were monitored frequently. For this purpose, all electrical connections were optically checked for shorts or damages. Electrical tests of the conductive connections as well as the sensor properties (e.g. dark current, depletion voltage) were carried out [14, 15]. A laser (wavelength $\lambda = 904$ nm and spot width $\sigma = 8.5\ \mu$m) was swept over the surface of halfmodules and the strip response was observed supplying e.g. information about dead channels or short circuits.

- In parallel to the series production, performances of single sensors and of half modules [16] were studied in a test beam setup using $1-6$ GeV electrons [10, 17, 18]. The sensor was placed in a setup equipped with high precision silicon strip detectors (intrinsic resolution better than 3 μm) supplying a reference measure of the test beam particle position. The angle of incidence was varied and the response of the sensor was observed. Detailed results were obtained concerning the angular dependance of the spacial signal shape as well as the angle and cluster algorithm dependance of the intrinsic resolution, see Fig. 3.14. The

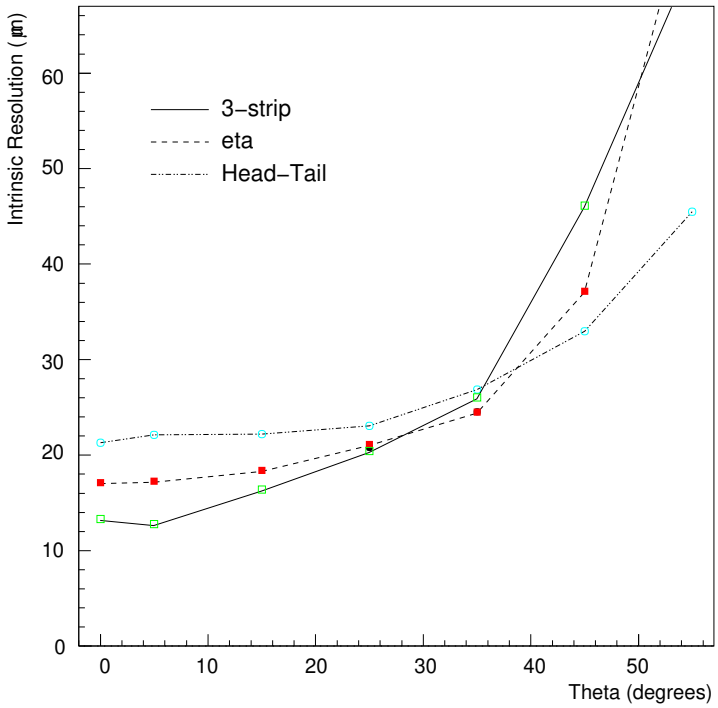

Figure 3.14: *The resolution of a* MVD *half module versus the angle of incidence as a result of the test beam measurements. 0° means perpendicular incidence here. As the dots refer to resolutions achieved with different cluster algorithms, the dependency on the algorithms becomes obvious [16].*

resulting intrinsic resolution was determined to be $\mathcal{O}(10)$ μm for perpendicular incidence. Two different cluster algorithms were found to be suitable for different intervals of angular incidence, as the spacial shape of the cluster depends strongly on the angle of incidence.

Chapter 4

Cosmic rays

This chapter gives a very short overview of cosmic ray induced particles and the description of their energy loss in matter, as these particles were used to test the response of the MVD in the system test, described in the following chapters.

4.1 The signal source: cosmic rays

High energy particles impinging on the earth´s atmosphere originate from astrophysical, mainly intragalactic sources, such as stars, supernovae, pulsars etc. and include all charged particles with lifetimes $\mathcal{O}(10^6)$ years or longer. The major contribution to the particle flux are protons ($\sim 78\%$).
The flux of charged particles at sea level includes mainly muons originating from the decay of charged mesons (pions and kaons). The charged mesons are produced in the interaction of cosmic particles with the atmosphere. Fig. 4.1 shows the vertical fluxes of cosmic rays and cosmic ray induced particles as a function of the altitude.

At sea level, the muons predominantly produced at a height of $\sim$ 15 km have typically lost 2 GeV and have a mean energy of $\approx$ 4 GeV. In the $10 - 100$ GeV range the muon energy spectrum reflects that of the primary particles which is proportional to $E^{-\alpha}$, with $\alpha = 2.7$ being the differential spectral index.

The integral intensity $I_{\mu\perp}$ of vertical muons above 1 GeV at sea level is [19]:

$$I_{\mu\perp} \approx 70 \text{ m}^{-2}\text{s}^{-1}\text{sr}^{-1} \tag{4.1}$$

The angular dependance is $\propto \cos^2\theta$ for muons with an energy of $E_\mu \sim 3$ GeV. For lower energies the angular distribution becomes increasingly steeper while it flattens and approaches a $\sec(\theta)$ distribution for higher energy (above a TeV).

The total flux J_{tot} crossing a unit horizontal area from above is given by:

$$J_{tot} = \int_{\theta=0}^{\theta=\frac{\pi}{2}} j(\theta,\varphi)\cos(\theta)\sin(\theta)\ d\theta\ d\varphi \tag{4.2}$$

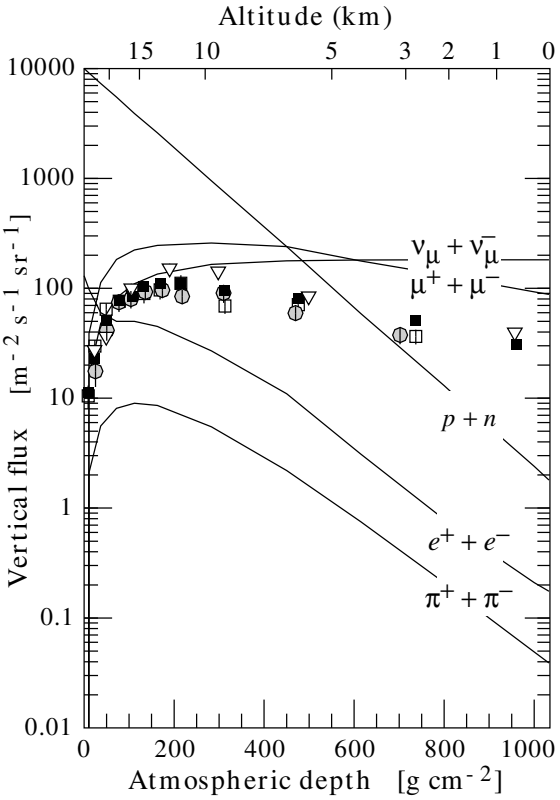

Figure 4.1: *The points show measurements of the vertical flux of cosmic ray induced negative muons with an energy of $E_\mu > 1$ GeV. The lines correspond to estimations based on an empirical formula for the primary cosmic ray flux [19].*

A quick and easy estimation of the total cosmic induced flux I penetrating a horizontal detector can by performed by assuming:

$$I \approx 1 \text{ cm}^{-2}\text{min}^{-1} \tag{4.3}$$

These dependencies were used to estimate the expected rate for the scintillator trigger setup.

4.2 Energy loss by ionisation

This section very shortly deals with the description of the energy loss of ionising particles.

4.2.1 Bethe-Bloch energy loss

The average energy loss by ionisation of moderately relativistic charged particles other than electrons passing through matter can be described over a wide energy range by the Bethe-Bloch formula:

$$-\frac{dE}{dx} = Kz^2\frac{Z}{A}\frac{1}{\beta^2}\left[\frac{1}{2}\ln\frac{2m_\text{e}c^2\beta^2\gamma^2 T_\text{max}}{I^2} - \beta^2 - \frac{\delta}{2}\right] \tag{4.4}$$

Where A is the atomic mass, Z the atomic number of the medium, ze the charge of the incoming particle, I the mean excitation energy, δ a density effect correction to ionisation energy loss and $T_{\max}$ the maximum kinetic energy that can be transmitted to a free e^- in a single collision (for further details see [20]).

The energy loss of positive muons in copper is shown in Fig. 4.2. If a particle has an energy corresponding to the minimum energy loss at $\beta\gamma \approx 3$, it is called a minimal ionising particle ("mip"). In common practice, muons in the energy range from 100 MeV to 100 GeV (in the flat region) are also called mips. For muons in the GeV energy range considered here the energy

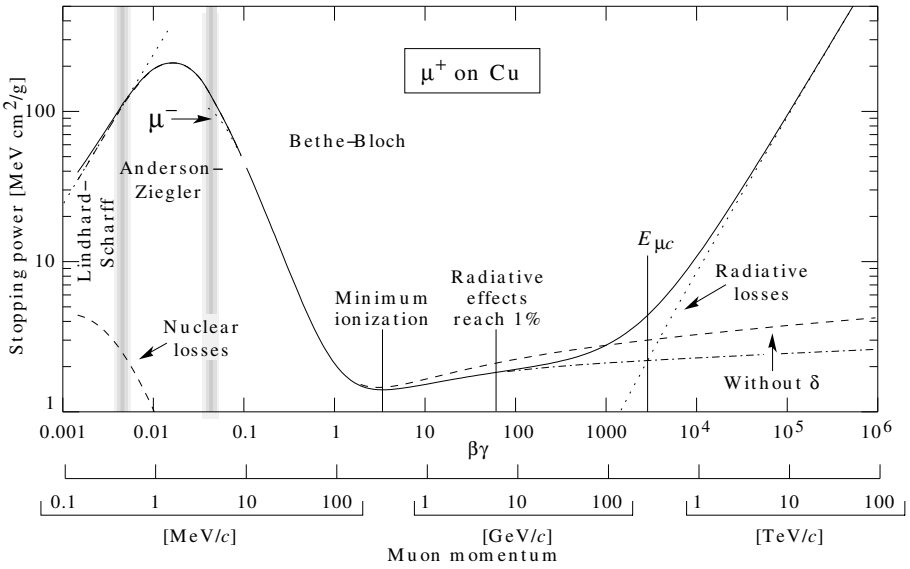

Figure 4.2: *The stopping power (≙ energy loss) of positive muons in copper is shown [20] as a function of $\beta\gamma = p/Mc$. The central range is described by the Bethe-Bloch formula.*

loss is described with an accuracy in the percent region by the Bethe-Bloch formula.

The average energy loss of 4 GeV muons in silicon ($\rho_{\,\mathrm{Si}} = 2.33$ g cm^{-3}) is ~ 4.7 MeV cm^{-1}, close to the average amount in scintillator material ($\rho_{\,\mathrm{polyvinyltoluene}} = 1.032$ g cm^{-3}) with an average energy loss of ~ 2.2 MeV cm^{-1} and well surpassed by the losses in iron ($\rho_{\,\mathrm{Fe}} = 7.87$ g cm^{-3}) being ~ 14.2 MeV cm^{-1}. Material data from [20].

4.2.2 Energy loss fluctuations

Two particles of the same energy do not loose the same amount of energy when traversing the same amount of material. The energy loss fluctuates about the mean value given by equation 4.4 and Fig. 4.2.
The Landau distribution approximately describes the fluctuations of energy loss by ionisation of particles of the same energy passing a thin layer of matter. The Landau formalism makes two restrictive assumptions [21]:

1. The typical energy loss is small compared to the maximum energy loss in a single collision.

2. The typical energy loss in the absorber should be large compared to the binding energy of the most tightly bound electron.

The landau distribution rises steeply with increasing energy, peaks at the most probable value and has a long tail for large values of the energy loss. An energy loss distribution for minimal ionising particles passing a MVD sensor is shown in Fig. 4.3.

The fluctuations around the most probable value (MPV) result from the statistical nature of the ionisation processes leading to energy loss. The mathematical definition of the probability density function can be found elsewhere [21].

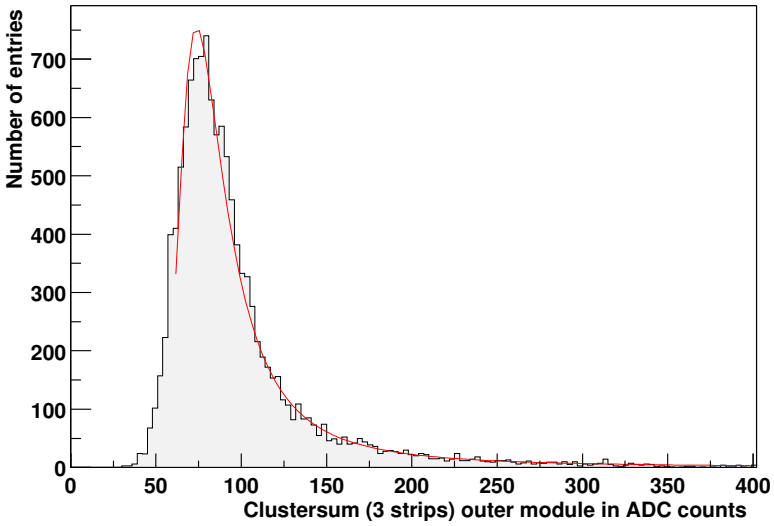

Figure 4.3: *The signal height distribution of one* MVD *half module during the system test. To the energy loss distribution, a landau fit was applied. The fit range was adjusted optimising agreement between the data and the fit peak.*

Chapter 5

The scintillator trigger

To survey the functionality and stability of the MVD sensors in the completed MVD and the subsequent readout chain, a test of the MVD (system test) was carried out, that will be described in chapter 6. This section describes the setup and construction of the scintillator trigger that was used to trigger on cosmic ray induced muons during the system test.
Trying to read out the detector continuously and store all data, would yield data sets of unmanageable size very quickly. Additionally, as the detector is not able to take data while it is read out, this would introduce a considerable dead time. Thus a device to trigger the readout on particle passage only is necessary.

The MVD system test trigger was built from scintillators, equipped with photomultipliers, arranged around the detector. Electrical signals produced by the photomultipliers on particle passage were used to form logic trigger signals.

The timing of the scintillators as well as the average pulse height was adjusted to equal values and an electronic setup was used to build and shape the trigger signal.

This section describes the setup of the scintillator trigger. The components are presented and their tests/construction and calibration is described. Some information on the performance of the setup is given at the end.

5.1 Trigger setup

The installation of scintillators around the MVD was realised as seen in Fig. 5.1.

The "TOP" layer, consisting of 10 ($10 \times 10 \times 50$ cm^3) scintillators centred around the nominal interaction point, was placed above the MVD; 10 similar scintillators below form the "DOWN" layer.

2 panel scintillators ($1 \times 40 \times 80$ cm^3) were placed at the sides. These are subdivided in 8 pads ($1 \times 20 \times 20$ cm^3) which were read out separately. They are referred to as "Side left" and "Side right" (left being the one in positive x direction).

The 2 separated panel scintillators ($47 \times 59 \times 1$ cm^3) in the forward direction are called "Forward

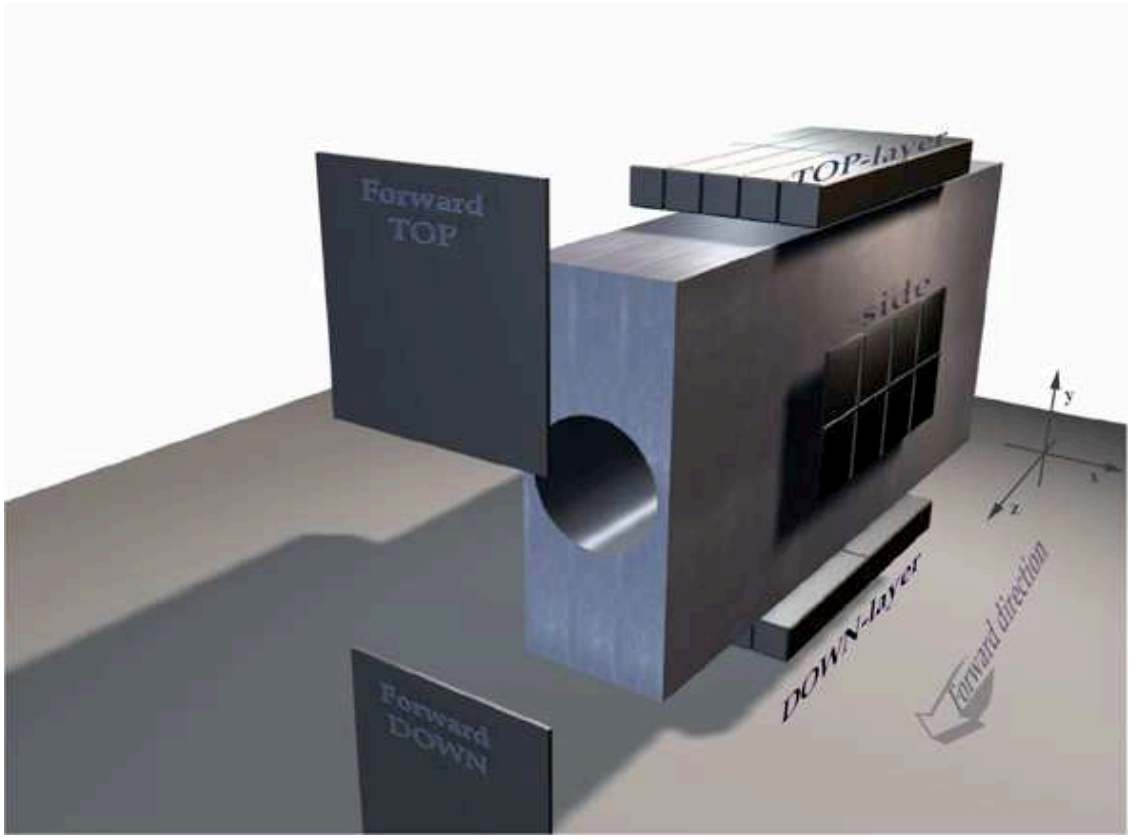

Figure 5.1: *A sketch of the scintillator arrangement around the* MVD. *The* MVD *is located in the cylindrical hole. (To avoid misalignment during the transports, the* MVD *was placed in a support frame for the duration of the transports and system test. The grey box shown symbolises this frame [22]). Also shown are the* TOP, DOWN, *Side and Forward scintillator layers. Details on the arrangement and dimensions are given in the text.*

Top[1]" and "Forward Down" respectively.

2 scintillators similar to the Forward ones, situated below the DOWN layer, are called 3rd layer (not shown in Fig. 5.1). The 3rd layer was not used for trigger purposes, but for efficiency measurements only.

A massive iron block (thickness: 20 cm, not shown in Fig. 5.1, but in Fig. 5.3a) was positioned above the DOWN and 3rd layer, to absorb low energy particles e.g. from electromagnetic and hadronic shower events.

The scintillators at the TOP, DOWN and Side positions were attached to an aluminium support, which can be seen in Fig. 5.2. The scintillators on the 3rd position were placed on a special board on the floor. The Forward scintillators were attached to two horizontal bars each. These 4 horizontal bars were connected to two vertical supports. Lashes were fixed to the bars to fix the scintillators in place, see Fig. 5.2, top left corner.

Fig. 5.3 shows a schematic transverse and longitudinal cut through the installation. The positions of the scintillators are given in millimeters.

[1]The capital letter for the Forward Top was introduced to clearly differentiate the "Forward" scintillator form the "forward" MVD.

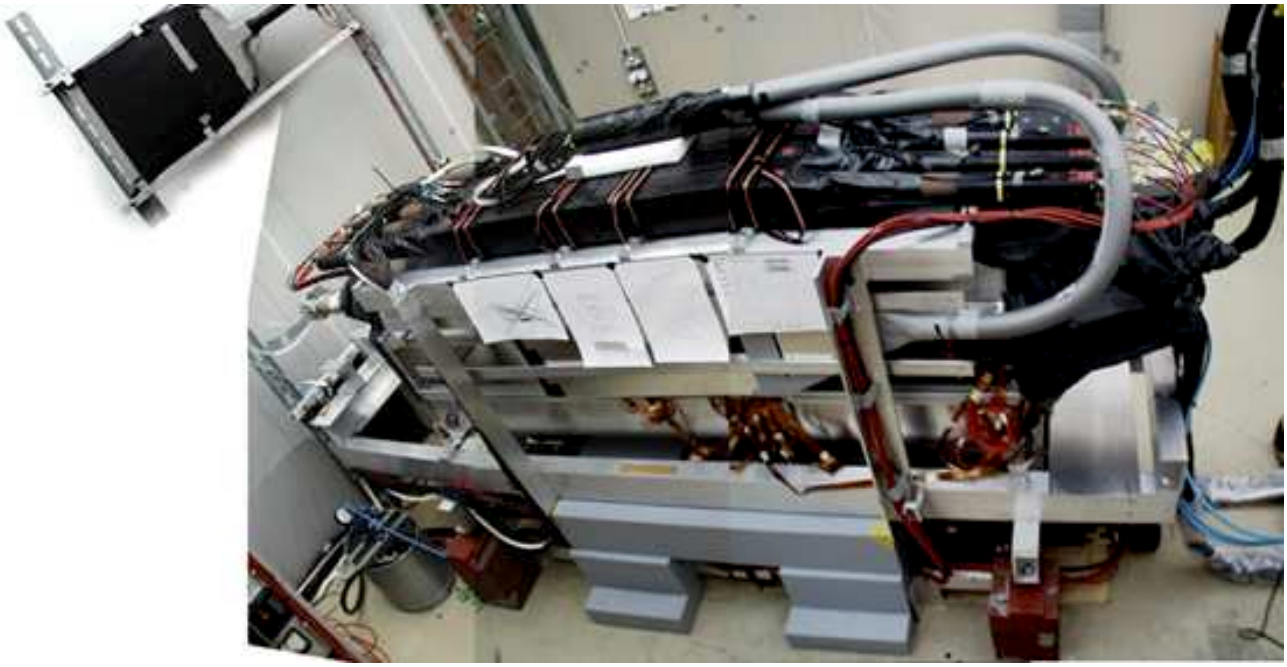

Figure 5.2: *The scintillator setup, seen from the left side. Apart from the Forward scintillators, all scintillators are attached to the aluminium support frame which is partly supported by the massive iron block. The mammoth like foam rubber tubes shielding the light fibers coming from the Side scintillators can be seen at the right side of the photo. The* 16*-fold* PM *(see section 5.3.1, Side scintillators) is placed above the* TOP *layer. On the right side the cables coming from the* MVD *are led towards the patchboxes.*

Two racks containing the high voltage supply units for the photomultipliers attached to the scintillators and the major part of the NIM[2] modules used for the trigger logic (as described in section 6.4) were positioned at the left side of the MVD in the forward region (see Fig. 5.2) and cabled to the scintillator setup, as can partly be seen in the Figures 6.2 and on the left side of 6.1.
One rack outside the tent (at a distance of $\sim$ 20 m) contained two NIM crates and a CAMAC[3] crate. The NIM crates contained modules to adjust the timing of the MVD and CAMAC readout relative to the scintillator coincidence signal and to further prepare the trigger signal for the MVD readout.
The CAMAC crate contained pattern units to register the discriminator signals from the scintillators having released the coincidence signal and a time to digital converter (TDC) which measured the relative time between the coincidence signal and a following clock pulse. The electronic modules are described in more detail in section 5.3.2 the trigger readout in section 6.4.

The diverse cable connections were realised using LEMO and BNC cables. The length of every

[2]NIM: Nuclear Instrumentation Methods; a rather old signal and electronic standard (standard NIM logic levels: on = -800 mV at 50 Ω , off = 0 mV)

[3]CAMAC: Computer Automated Measurement And Control; is a standardised modular data handling system. It represents the joint specifications of the U.S. NIM and the European ESONE Committees. For more details refer to [9] or [23]

signal cable was determined (measured in ns using an oscilloscope) and all connections were checked for electrical contact. The complete setup was operated for a duration of 3 weeks. The TOP, DOWN and 3rd layer were placed and operated in the Jade hall several weeks before the Side and Forward scintillators.

Before the setup was installed at the system test site, all components had been assembled, intensively tested and adjusted at the Institute for Experimental Physics (in building 67*b* on the DESY premises). After e.g. all scintillators of the TOP / DOWN layer were adjusted to equal average pulse height and all numerous light leakages were sealed, the preassembled setup served to test the readout electronics, see Fig. 5.4 and 5.5. The components, construction, performed tests and calibration steps of the setup are described in section 5.3.

5.2 Purposes of the different layers

The scintillators were arranged around the detector, so that different sections of the MVD were triggered by different sets of scintillators:

The **barrel section** was triggered (mainly) by (see Fig. 5.3a/b) →

- TOP with DOWN layer
- Side left with Side right scintillators

The **forward section** was triggered (mainly) by (see Fig. 5.3b) →

- TOP layer with the Forward Down scintillator
- DOWN layer with the Forward Top scintillator

The granularity of the scintillator setup was used in the analysis to estimate the direction of the passing particle.

The arrangement provides a good coverage of the detector. The forward section is fully enclosed in the coincidence volume spanned by the Forward scintillators with the TOP and DOWN layers.

5.3 Components

The coincidence setup was built from existing components. These components will be presented here. Every component was intensively checked for functionality and reliability. The components tests and calibration are presented.

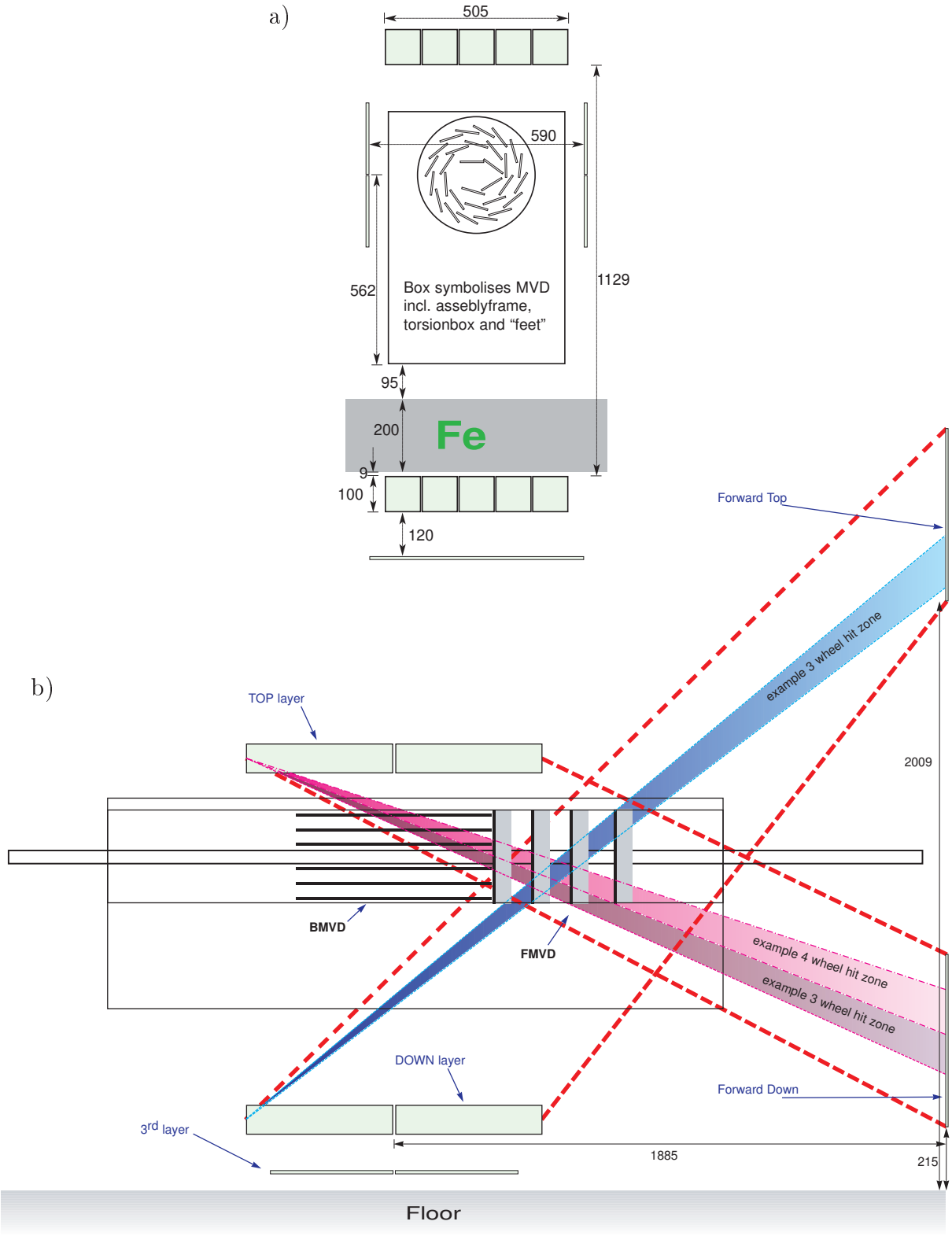

Figure 5.3: *Trigger cut a) transverse, view in negative z direction. Some dimensions of the setup are given in millimeters. The scintillators of the* TOP *layer are above the* MVD*. The iron,* DOWN *and* 3^{rd} *layer are situated below the* MVD*. On the left and right side the Side scintillators are situated. b) longitudinal. On the right the Forward scintillators are sketched, the Side scintillators are not shown. Possible regions for trigger releasing particles are sketched (between thick dashed stripes) as well as some example hit zones.*

Figure 5.4: *The setup in the cellar in building 67b. On the right side, the test setup of* TOP, DOWN *and* 3^{rd} *layer can be seen. The rack containing the readout and supply electronics is situated on the left. The Side and Forward scintillators were prepared in the same room (not shown).*

5.3.1 Scintillators

Three types of scintillators were used in the coincidence setup, used in different layers. In this section, the scintillators are presented according to the layers they formed.

As scintillators and photomultipliers are standard devices, they are not described in detail here. A description can e.g. be found in [9, 20]. In short, the particles passing through the scintillator material loose energy mainly by interaction with bound electrons on their way.
The base material contains aromatic rings. Additionally a primary and a secondary flour are dissolved into the base material. Electrons of the aromatic rings in the plastic scintillator material are excited to higher energy levels by the traversing particles. After a short time ($\mathcal{O}(10)$ ns) the rings decay to the ground state mainly by a resonant dipole-dipole interaction with the first flour. This interaction reduces the decay time of the aromatic rings. To reduce the

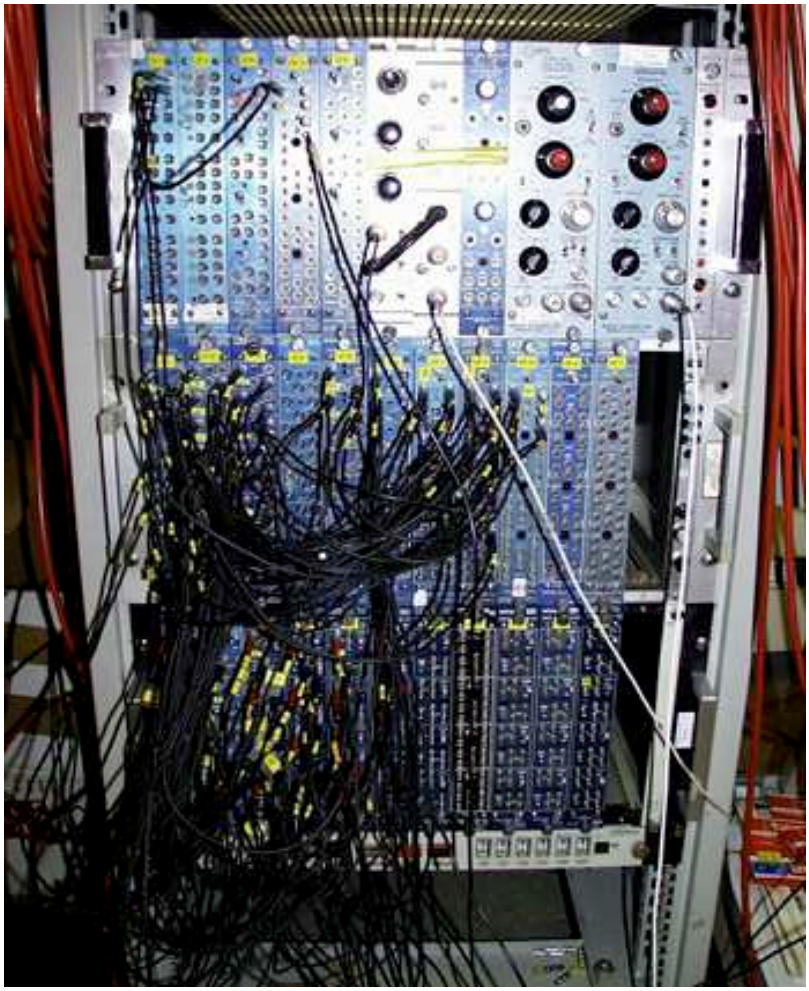

Figure 5.5: *The readout electronics in the test setup of the scintillator coincidence setup in the cellar of building 67b. The lowest crate contains the fan in fan out modules, the middle one the discriminators and coincidence units. The topmost crate is filled with test and spare devices as well as the* MCA *signal shaper chain, which is explained in section 5.3.1.*

reabsorption probability of the photons emitted by the primary flours and to convert the photons to the frequency of maximum quantum efficiency of the PM's photocathode, a secondary flour is used. It absorbs the photons from the primary flour and emits photons at a lower energy. The surplus energy is released in phononic decay. The photons emitted by the secondary flour are subsequently reflected to the light guides and brought to the photocathode of the photomultiplier.
Arriving at the photocathode, the photons release electrons towards the first dynode of the photomultiplier via the photo effect. These photo electrons are then exponentially multiplied by the dynode cascade and the signal is read out by the electronics.
The average energy loss by ionisation can be described by the Bethe-Bloch-formula while the fluctuation of the actual individual energy loss of a charged particle can be described by the landau distribution (see section 4.2).

Top and Down layer scintillators

The 20 scintillators of the Top and Down layer (see section 5.1) were flour doped polyvinyltoluene bars. A light guide was attached to the scintillator. A sketch of one scintillator is shown in Fig. 5.6a.

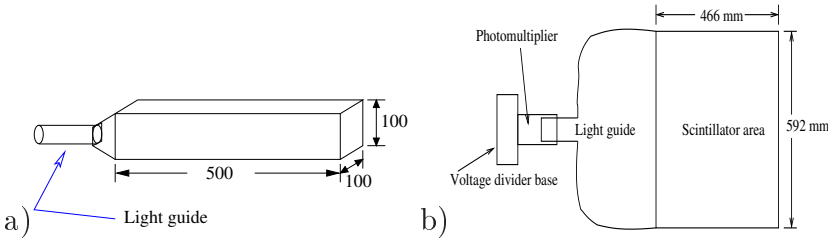

Figure 5.6: *Sketches of the scintillators as placed a) in the* Top *and* Down *layer, b) on the Forward position and in* 3^{rd} *layer*

The polyvinyltoluene bars are shielded from external photons by a double layer of aluminium and black plastic foil. Attached to the light guide is a photomultiplier (Pm) inside a metallic magnetic shielding tube and a voltage divider. Cable connectors (signal and power supply) are situated at the end of the shielding tube.

Forward and 3^{rd} layer scintillators

For the two 3^{rd} layer and for the Forward Top and Forward Down positions, flat and rather large polyvinyltoluene scintillators were used, sketched in Fig. 5.6b. Light guides transport the photons emitted in the sensitive volume at particle passage to the attached Pm.

Side scintillators

The Side position scintillators, enclosed in an aluminium encasement, are subdivided into 8 pads. Each pad is independently read out by six light fibers. The 96 approximately 2 m long fibers of both scintillator panels are brought to one 16-fold Pm (R4760 by Hamamatsu) inside light proof foam rubber tubes. Each of the 16 channels converts the light signal of the pad attached to electrical signals. The photomultiplier signals of the Side scintillators are amplified ($\times$10, using fast photomultiplier amplifiers, see section 5.3.2).

5.3.2 Electronics

The electronic components used in the setup are described here.

Power supplies

The Pms of the setup were supplied with high voltage by two kinds of power supplies: Three valve based high voltage supply units were used for the Pms in Top, Down, Forward and

3rd position. To each supply unit, one or two voltage dividers were attached. These voltage dividers were connected to the 24 photomultipliers of the different layers.
The Side scintillator's PM was attached to a low voltage unit. This 16 fold PM internally produced the necessary high voltage by a Cockroft Walton generator (a diode capacitor cascade circuit [9, 24]).

Electronic modules

As all signals used in the electronic part of the setup are negative ones, "high" is used for signals of a high absolute value, e.g. -800 mV is higher than -100 mV.

All the electronic modules were NIM or CAMAC modules. As can be seen in the logic sketch in

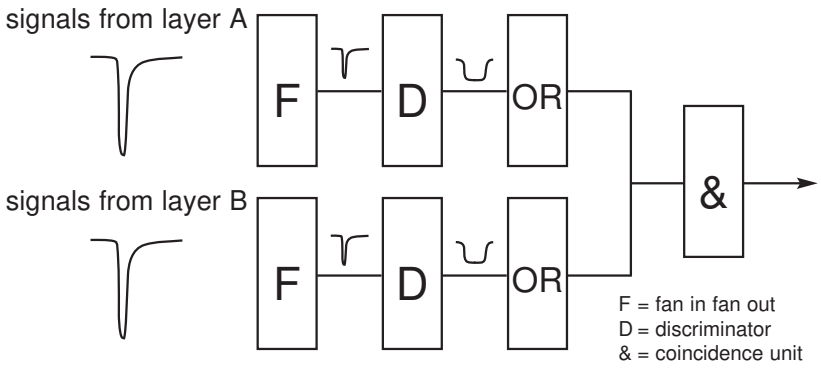

Figure 5.7: *A simplified logic sketch of the coincidence setup. The signals coming from the different layers are led trough the fan in fan out modules, discriminated and then summed at the* OR *units. A signal is generated at the* AND*, whenever two scintillators of two chosen layers indicate particles at the same time. The setup is described in more detail in section 6.4.*

the Figures 5.7 and 5.9, different modules were used in the electronic setups:

- **Linear fan in fan out**
  This module allows the connection of 4 inputs and 4 outputs per channel (4 channels per module). The sum of the input signals is unchanged at every output. It is actively amplified so as not to be dampened in amplitude when given to several outputs.
  In the setup these are used as impedance converters and to be able to maintain the setup by:
  - observing the scintillator pulses without disturbing the trigger chain
  - applying testpulses.

- **Photomultiplier amplifier**
  This module was used to amplify the signals of the Side scintillators by a factor of 10. The module has 12 input channels and 24 output channels (two per input channel). The pedestal of the channels can be adjusted by a potentiometer on the circuit board. The internal delay is 4 ns.

- **Discriminator**
  One channel accepts one input signal and sends a standard NIM signal of adjustable width to its 3 outputs whenever the input signal exceeds an adjustable threshold value (one module contains 8 channels).
  For most of the used modules, the lowest possible threshold value was ~ -30 mV.
  In the setup the threshold level was adjusted to -500 mV for the TOP / DOWN layer scintillators and to ~ -30 mV for the other scintillators. The width of all signals in the primary coincidence logic, as described in 6.4, was set to 20 ns.

- **Coincidence unit (AND)**
  When two signals arrive at the two inputs of one channel of this module at the same time, a standard NIM pulse is sent to the 4 outputs. $'$Arriving at the same time$'$ means, that the two signals overlap at least ~ 4 ns.
  The outputs are (among other features not used for the setup) a linear out and a standard out. The linear out sends a NIM pulse with the width of the overlap of the input signals while at the standard out, one receives a pulse of adjustable but constant width.
  In the setup the standard out was used and the width was set to 20 ns (one module contains 4 channels).

- **Logic fan in fan out (OR)**
  The OR unit sends a NIM pulse of adjustable width to its 2 outputs whenever it receives a signal on at least one of its 4 inputs per channel.
  One module contains 4 channels which can be used in the 4×4, 2×8 or 1×16 mode, which means that either the four channels are separated (4×4), or 2 (2×8) resp. 4 (1×16) channels are used together building the sum of all the inputs of the 2 or 4 channels.
  These modules are used to form an OR of the signals of one layer of scintillators, e.g. the TOP layer.

The following modules were used for a MCA readout chain only (to record the spectra of the scintillators, see section 5.3.3):

- **Main amplifier**
  This device integrates fast input signals and delivers a slow bipolar or unipolar pulse of an amplitude proportional to the area under the input pulse.

- **Gate generator**
  A long NIM gate signal of adjustable width (1 μs to 10 s) is sent to the outputs of this module whenever a NIM pulse is given to the start input.

- **Linear gate**
  The linear gate is a switch controlled by the gate generator. When it receives a NIM pulse at its gate input, it connects two other ports and lets any occurring signal pass for the duration of the controlling NIM pulse.

Also two additional

- **Tail pulse generators**
  The module generates pulses with a short rise time and a longer fall time. The polarity, amplitude, rise time and the rate can be adjusted. Additionally, one module can trigger the pulse generation of another module. It is then possible to adjust the relative phase of the two pulses by a potentiometer and e.g. scan the duration of acceptance of a coincidence module.

were used for test purposes. Two CAMAC modules were used to record information concerning the coincidence signal:

- **Time to digital converter (TDC)**
  A TDC is an electronic stop clock. It sets bits with a given frequency (stepsize^{-1}) beginning after a start signal and ending after a stop signal. After a stop signal has occurred, the stored value can be read out and reset. The minimum time between a start and a stop signal was ~ 25 ns for the used LeCroy TDC, so the stopping signal was delayed by ~ 25 ns relative to the start signal. The stepsize was set to 250 ps.

- **Pattern unit**
  The pattern unit counts the number of signals occurring at its inputs (16 input channels for the system test pattern units) during an interval of time given by a gate signal. Subsequent to the gate signal, the stored counts can be read out and the channels can be reset. In the system test case only one or no signal occurred during active gate at the channels of the pattern unit, as the recorded signals were the discriminated signals from the scintillators contributing to the coincidence signal.

5.3.3 Tests, calibration and construction

The components presented above had to be constructed / repaired and calibrated before they could be used in the coincidence setup. The preparation steps of the different components are described here.

TOP and DOWN layer scintillators

To learn about the scintillator and photomultiplier quality, the pulses produced by passing cosmic ray induced particles were observed with an oscilloscope[4] and the discriminated pulse rate was checked with a scaler[5].

Observed problems

- not light proof
  Whenever a scintillator was badly shielded from external photons, the signal tended either to vanish when the light was switched on in the laboratory (the flux of photons

[4]The oscilloscopes used were Tektronix: 2 channel digital, 500 MHz, 2 GS/s

[5]A scaler is a pulse counting device. It counts pulses for a given time and shows the pulse rate on its display.

caused a high flux of electrons at the first dynode. Due to the limited supply current, the voltage necessary for electron multiplication was not achievable.), or, when smaller leakages appeared, the rate went up considerably and many pulses could be observed with a very small amplitude[6] compared to the average cosmic event.

- electrical breakdowns in the photomultiplier / voltage divider
  Sometimes signals occurred as sketched in Fig. 5.8. When this happened, either the

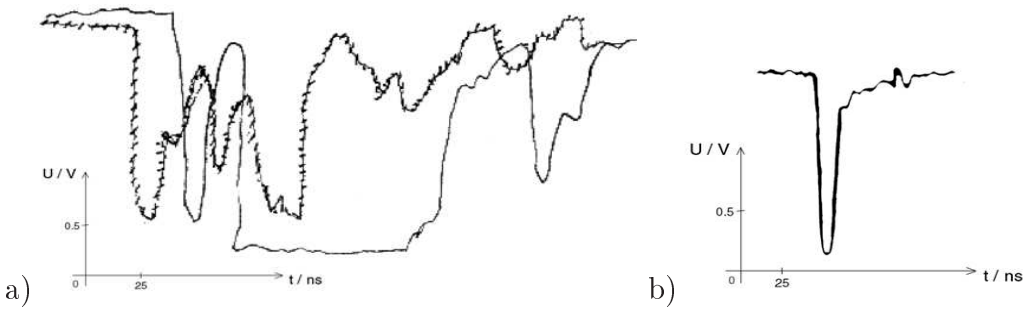

Figure 5.8: *a) An original pencil sketch from the lab book of an unusual pulse due to el. breakdowns in a defect voltage divider base. b) A sketch of a good pulse.*

voltage divider of the PM or the PM itself was damaged.

Repairs

- improve light shielding
  The scintillators with light leakages were wrapped in an additional double layer of thick back plastic foil. Like this the observable dependance on exposition to visible external photons was removed.

- exchange voltage divider / photomultiplier
  The metallic housing of the PM and the voltage divider is attached to the light guide. The voltage divider housing can be unscrewed from the PM housing. The photomultiplier can then be separated from the voltage divider (it is connected to the divider via a special plug) and reequipped with functioning spare parts.

HV / gain adjustment of the TOP / DOWN layer scintillators

The scintillators gain levels were adjusted to assure that the most probable signal value produced by a passing particle was well above the selected discriminator cutoff value and at the same position for all scintillators.
The supply voltage is the only way to vary the gain level of the PM of the scintillator. A rise in the voltage directly enhances the gain.

By enhancing the voltage not only the signal levels, but also the noise level is increased. Thus a limit on the maximum voltage is introduced by the requirement to keep the random coincidence rate low, see section 5.4.3. Another limit is given by electrical breakdowns occurring between the dynodes of the photomultipliers starting from PM dependent voltage levels. As these

[6] typically an order of magnitude smaller than pulses produced by particle passage.

breakdowns lead the to destruction of the PM, the corresponding voltage levels had to be avoided carefully.

To adjust the individual supply voltages of the TOP / DOWN layer scintillators, the signal spectra of the scintillators were recorded with a multi channel analyser (MCA). The signal spectrum of one scintillator was chosen to be the reference for all others (gauge spectrum). The supply voltage of all other scintillators was varied while observing changes in the spectra until the peak of all spectra was approximately at the same place as the one of the gauge spectrum. The precision of this method was sufficient to yield similar efficiency and response of all scintillators for the coincidence setup.

A schematic drawing of the MCA setup is shown in Fig. 5.9. The spectrum was acquired in a

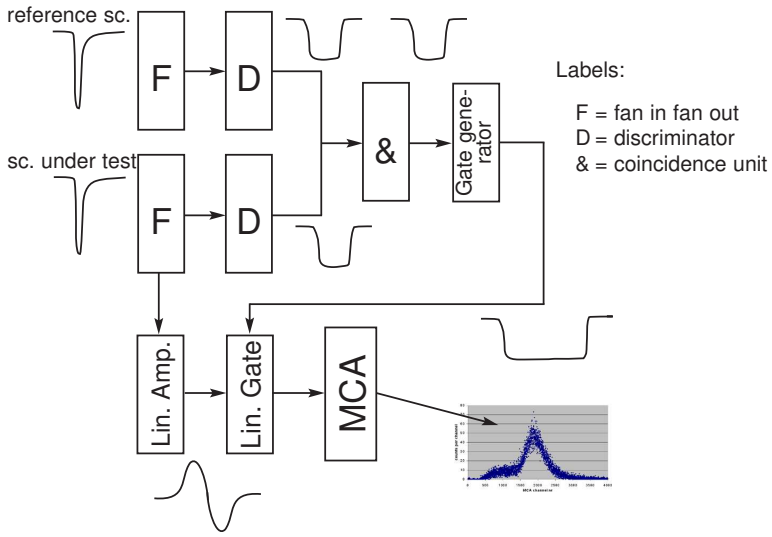

Figure 5.9: *The* MCA *setup used to find the individual voltage level for each scintillator of the* TOP *and* DOWN *layer to gain equal average pulse height. At the discriminators a signal threshold of* 500 *mV was applied.*

coincidence setup to remove the low level noise signals.
The scintillator signals from the PMs were fed into a fan in fan out module (F). Here two branches were used: One branch to form the coincidence signal triggering the MCA and one readout branch to determine the signal height of the scintillator under test.
In the triggering branch, the signals were discriminated, applying a threshold cut. The discriminated signals were fed to a coincidence unit, where a signal was generated whenever two signals arrived at the 'same' time, i.e. in a given time window (this window was set[7] to ~ 36 ns). The gate generator connected to the coincidence unit produced a signal adjusted in length and timing to route the corresponding signal of the scintillator under test to the MCA.
The signal height determination took place in the other branch: Here the scintillator signals coming from the fan in fan out were shaped by a linear amplifier (from a $\sim 10 - 20$ ns long unipolar pulse to roughly 2 orders of magnitude longer bipolar signal) and then led to a linear

[7]If both signals arriving at the coincidence unit have a width of 20 ns and the minimum overlap is 4 ns, a coincidence window of 36 ns results.

gate. The linear gate connected the output of the linear amplifier to the input of the MCA for the duration of the applied gate generator pulse.

A spectrum aquired with the MCA setup is shown in Fig. 5.10. The influence of the discriminator threshold can be seen at channel number 500. Ideally, the device under test would not be included in the trigger. The discriminator threshold would then have no direct influence on the recorded spectrum. This was not possible in the given setup, but the effect is not crucial, as the position of the peak is not influenced by this effect.

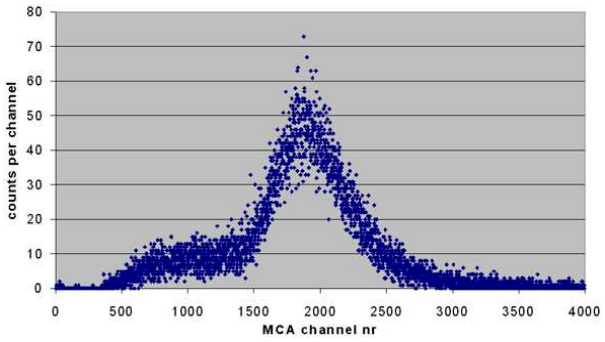

Figure 5.10: *A scintillator hit spectrum as acquired with the* MCA *setup to set the high voltage level for all scintillators of the* TOP *and* DOWN *layer. The high number of low signals is due to the way the gate signal was supplied and the resulting long integration time of the linear amplifier.*

The resulting supply voltage settings ranged from 1.9 to 2.1 kV.

Forward and 3rd layer scintillators

Checks, observed errors and repairs of the Forward and 3rd layer scintillators where comparable to those of the TOP / DOWN layer scintillators.

As the signals of these scintillators were a lot lower than those of the much thicker TOP / DOWN scintillators, the highest possible supply voltage, yielding the highest possible efficiency, was chosen. The limitations concerning the maximum random trigger rate and the breakdown signals set the limit on the highest possible voltage. The high voltage was thus chosen less precise than for the TOP / DOWN scintillators, but as it concerns only four scintillators, two of which are not used for trigger purposes, this was not considered to be crucial.

Side scintillators

The 16-fold PM was new and of higher quality, thus it did not have to be repaired. Still the light proof encasement was problematic, as the "two scintillators" had been "one scintillator" just before the coincidence setup assembly. They had been separated by sawing through the setup in the middle. An aluminium encasement shielded the scintillators form external photons, while at the side, from which the light fibers exited the encasement it was completely open. The open side was closed by attaching 2 aluminium plates, which were shaped to guide the

fibers from the broad scintillator to the slim foam rubber tube, see Fig. 5.11. The tube was used to lead the fibers to the PM. The remaining slim open sides were closed with aluminium foil which was attached to the plates by black plastic tape.

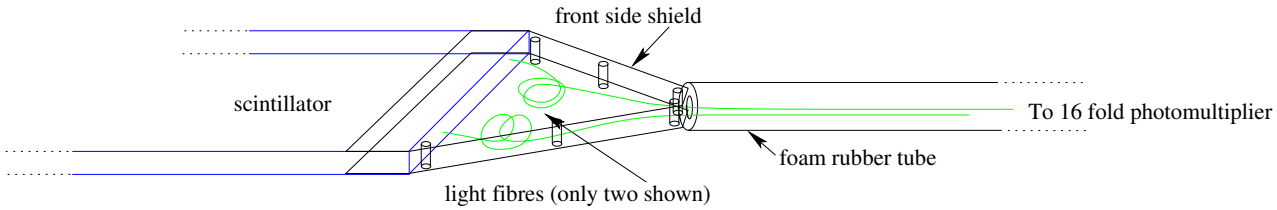

Figure 5.11: *The Side scintillator. The side that was not shielded from external photons was closed with 2 aluminium plates. The remaining open sides were closed with an aluminium foil tape layer. At the slim end of the plates, a foam rubber tube was attached to guide the light fibers to the 16 fold* PM. *The fibers were adjusted in length by winding longer ones up between the aluminium plates.*

The panels were read out by six light fibers per pad, however, which set of light fibers belonged to which pad was not labelled definitely and thus unknown.
The correlation of light fibre bundles to pads was found by using another small scintillator, after the panels had been sealed. An oscilloscope was triggered by the pulses of the small test scintillator. One channel of the 16 fold PM, corresponding to one pad, was attached to the other channel of the oscilloscope. When sweeping the surface of the Side scintillator panel with the small test scintillator, pulses were seen from the observed Side scintillator channel whenever the same particles passed the test and the Side scintillator.

The high voltage was applied differently: inside the magnetic shielding of the PM, a Cockroft-Walton diode capacitor cascade was situated to generate the required high voltage from a low voltage supply line. The low voltage was applied to the PM by using a NIM module produced by the NIKHEF Institute. The voltage level was chosen observing results from efficiency measurements (as described in section 5.4.3) which suggested to raise the voltage as high as possible. The upper limit on the voltage was given by the same requirements as applying for the Forward scintillators.

Electronic module tests

Due to the electronics equipment being of rather advanced age, many tests had to be performed. To ensure to have enough spare parts for the scintillator trigger when in use, availability and necessity checks were performed during the assembly of the trigger setup and a generous spare supply was collected.

The modules were tested by applying pulses to the module input/s and observing the response. Pulses of varying amplitude for testing the linear fan in fan outs and the discriminators were produced by a tail pulse generator. The other modules were tested using pulses of varying length generated by a discriminator which was connected to a pulse generator.

The fan in fan outs (F, fan) cut off pulses higher than $\sim -3\,\mathrm{V}$; as long as the input value was higher, the fan output value was constantly 3 V. Some fans attenuated the input signal

considerably and were sorted out, others showed constant negative outputs and were also not used.

The discriminators (D) were tested and set (threshold value, signal length) at the same time. Some modules again had constant negative outputs, sometimes only restricted to separate outputs, so these were marked and the rest of the module was used.

To test the coincidence units (AND, &), 2 tail pulse generators were coupled using the external trigger I/O port (of the pulse generators) to produce two pulses of defined and adjustable phase shift. The response of the coincidence units was observed on an oscilloscope. A minimum signal overlap time of approximately 4 ns was necessary to produce a coincidence signal. Occasional erratic behaviour was similar to that of the discriminators.

The logic fan in fan outs (OR, ≥ 1)) were supplied with a NIM pulse of 20 ns width and their response level and time was observed. Those modules with constant negative output were once more sorted out.

5.4 Performance

5.4.1 Hit distribution

The scintillator hit distribution is shown in Fig. 5.12. It shows, that all scintillators contributed uniformly to the coincidence signal rate. This was achieved by the overall timing and amplification adjustment of the coincidence setup (the jitter of single scintillator hits around the coincidence pulse was $\mathcal{O}(5)$ ns). The variation of the trigger contribution rate from layer to layer is due to the flux of cosmic rays and the geometry of the setup. The main contribution comes from the TOP / DOWN layer.

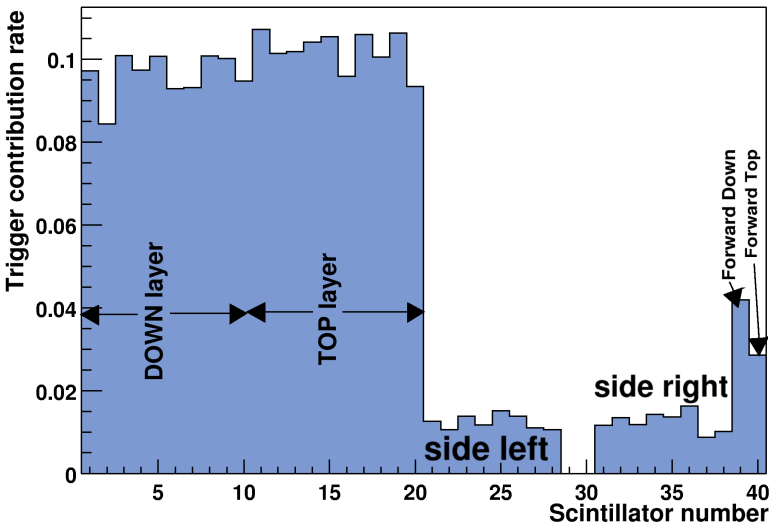

Figure 5.12: *The scintillator hit distribution during the system test on the basis of* 10^4 *events.*

5.4.2 Estimation of the expected rate

To be able to estimate whether the coincidence setup indeed indicated the passage of cosmic ray induced particles, an estimation of the expected rate of the TOP / DOWN layer was performed. The properties of cosmic ray induced particles were assumed to be as described in section 4.1. Using equation 4.3, a single layer (TOP or DOWN) should yield a cosmic induced hitrate of ~ 85 Hz. For the coincidence rate of both layers, the geometry of the setup had to be taken into account.

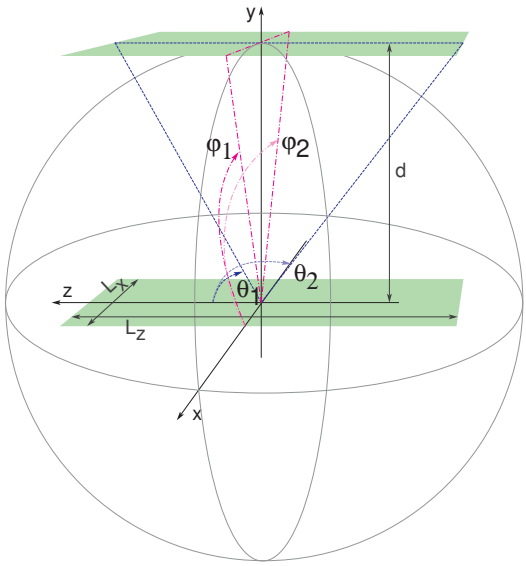

Figure 5.13: *The geometry of the* TOP / DOWN *layers is indicated by the shaded areas. The angles* $\varphi = \varphi_2 - \varphi_1$ *and* $\theta = \theta_2 - \theta_1$ *are the opening angles of the setup and were used to calculate the solid angle spanned by the setup.*

The flux of cosmic ray induced muons is given per steradian, square meter and second. Thus, to estimate the coincidence rate of the setup, the covered solid angle and the area of the setup needs to be known, see Fig. 5.13. The solid angle was estimated using the simplifying assumption, that close to the y axis, lines due to the variation of φ with fixed θ and vice versa produce areas on the uniform sphere that resemble rectangles (rather than circle like objects close to the z axis). Thus the solid angle could be calculated by integrating over a range of angles given by the opening angles of the setup φ_i and θ_i as defined in Fig. 5.13.
Integrating the angular dependent flux over the given interval yields the flux incident at one point of the DOWN layer. Multiplication of this point flux with the area of the DOWN layer (assuming that the covered solid angle varies little when changing the point on the DOWN layer) yields the total flux f penetrating the TOP / DOWN setup:

$$\begin{aligned} < f > &\approx \int_{\varphi_1}^{\varphi_2} \int_{\theta_1}^{\theta_2} I_{\mu\perp} \sin(\theta) \sin(\theta) d\theta d\varphi = I_{\mu\perp}[\varphi_2 - \varphi_1] \frac{1}{2} \left[-\sin(\theta)\cos(\theta) + \theta \right]_{\theta_1}^{\theta_2} \\ &= 11 \text{ Hz} \end{aligned}$$

where the angles are:

$$\varphi_1 = \frac{\pi}{2} - \arctan\left(\frac{L_x}{2d}\right) \quad \varphi_2 = \tfrac{\pi}{2} + \arctan\left(\tfrac{L_x}{2d}\right)$$
$$\theta_1 = \frac{\pi}{2} - \arctan\left(\frac{L_z}{2d}\right) \quad \theta_2 = \tfrac{\pi}{2} + \arctan\left(\tfrac{L_z}{2d}\right)$$

with

$$L_x = 0.505 \text{ m},\ L_z = 1.01 \text{ m and } d = 1.229 \text{ m}$$

The distance d is measured from the centres in y of the TOP / DOWN layers, introducing another simplification, namely that the extension in y of the layers can be neglected.

This result is consistent within 12% with the coincidence rate of the TOP / DOWN layers, which was determined to be

$$12.5 \pm 0.4 \text{ Hz}.$$

This estimation thus shows, that no gross errors happened during in the construction of the scintillator setup and the measured rate is due to the particle flux.

5.4.3 Trigger efficiency

The relative supply voltages of the photomultipliers of all scintillators had been adjusted to approximately equal pulse height. To determine the absolute HV working point in the final system test setup, measurements of the dependance of efficiency on the "global" supply voltage level[8] were performed, hereafter referred to as "efficiency measurements". The aim was to find the voltage level with tolerable random coincidence signal rate (rising with increased voltage level due to higher single hit rates of all scintillators) and maximum efficiency. For this purpose, coincidence rates of different sets of scintillators were determined for various voltage levels.

The principle of all measurements was the following:

2 layers were used as a reference; their coincidence rate r_2 was determined. The surveyed layer was situated between the 2 reference layers and included in the coincidence. Again the coincidence rate r_3, this time with 3 layers, was determined. Ideally, r_2 and r_3 should be measured simultanously. As only one scaler was available, the rates were determined sequentially leading to statitically independent measurements of r_2 and r_3. The measured change in the rate was due to:

- efficiency of the surveyed layer
- slight changes in the geometry of the coincidence setup due to the included third layer which had to be corrected

[8] The voltage is applied to the PMs by a voltage divider which is supplied by a "global" power supply. Thus the relative voltages are set using the voltage divider, while the "global" voltage is set by changing the voltage level of the global supply.

A geometrical dependance factor c_{geo} was estimated from the reduction of the coincidence area due to the included layer under test, changing from A_{ref} before the inclusion to A_{red} after the inclusion, see exemplary Fig. 5.14; here the setup for measuring the Sides is sketched.

$$c_{geo} = \frac{A_{red}}{A_{ref}}$$

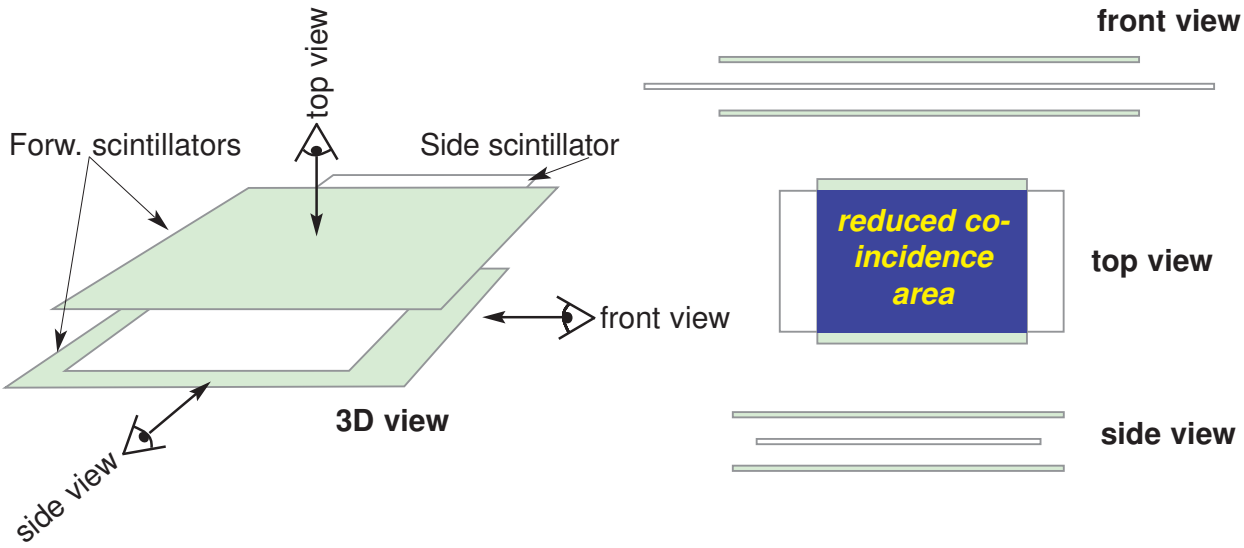

Figure 5.14: *The positioning of the Side and Forward scintillators to determine the efficiency of the Side scintillators is shown here. The reduced coincidence area (A_{red}) in the setup is introduced by including the Side scintillator under test in the coincidence circuit.*

Once c_{geo} was known, the efficiency could be calculated.

$$\text{eff} = \frac{r_3}{r_2} \cdot c_{geo}$$

The upper limit on the voltage range was given by a chosen limit on random coincidence hits. The random coincidence rate of two given layers (with the single hit rate $r_{\text{layer n}}$) was estimated using the following formula:

$$r_{\text{layer 1}} \cdot r_{\text{layer 2}} \cdot \text{coincidence width} \approx \text{random coincidence rate} \tag{5.1}$$

A maximum single hit rate of $\sim$ 500 Hz per layer was required to keep the random coincidence rate well below the per mille regime. Together with the discriminator threshold level this yielded an upper limit of the voltage range.

Measured was the efficiency dependance of the DOWN layer in the final setup as well as that of both Side scintillators.

To measure the efficiency of the DOWN layer of scintillators in the final setup, the TOP and 3rd layers were used as reference layers. This measurement was performed for a range of applied

voltages ("global" voltage) from 1.39 kV to 2.35 kV. In the region of efficiency saturation the maximum single hit rate of 500 Hz limit was not exceeded; the single hit rate was the order of 300 Hz. At the voltage working point thus chosen, an efficiency of roughly 100 % but with large errors was determined for the DOWN layer. The efficiency graph is shown in Fig. 5.15a.

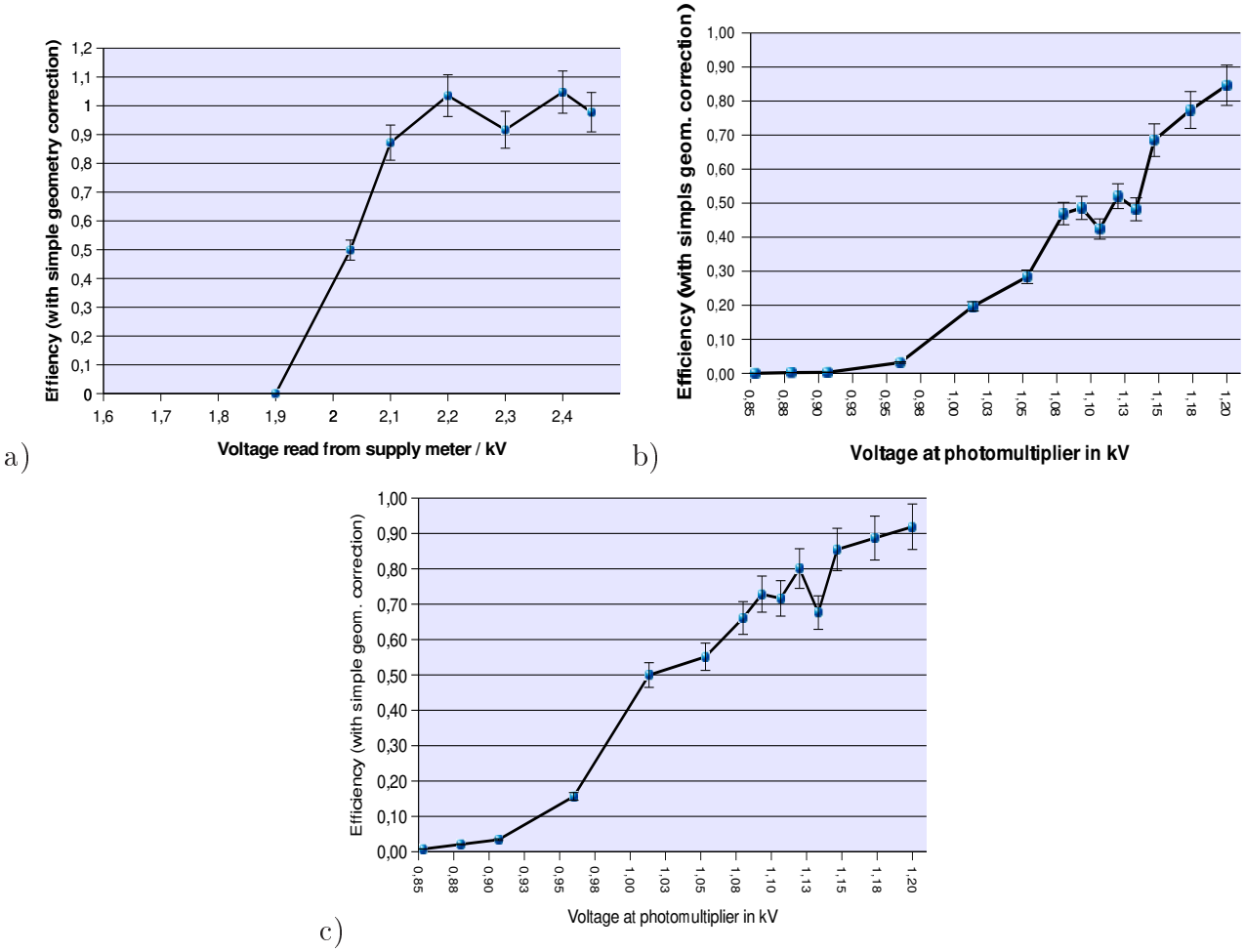

Figure 5.15: *Efficiency curves a) of the* DOWN *layer versus the global supply high voltage level. The voltage level was measured at the main supply unit. It was applied to the photomultipliers using a voltage divider. b) of the right Side scintillator and c) of the left Side scintillator versus the voltage at the 16 fold* PM*. The Side scintillators did not reach the saturation region. The limit on the maximum applied voltage was given by breakthroughs occurring in the dynode cascade of the* PM*.*

The efficiency of the Side panels was determined using the Forward scintillators as reference devices. Being of approximately the same size, the scintillators were arranged as shown in Fig. 5.14. The Side scintillators were measured over a range from 0.85 kV to 1.2 kV. Efficiency saturation was not achieved. The reason for this might have been, that the light fibers were not brought close enough to the photocathode of the photomultiplier, or that the light fibers were connected inefficiently to the scintillating pads.

The resulting efficiency curves of the Side scintillator panels are shown in Fig. 5.15b and c.

Chapter 6

The system test

To check the functionality, interplay and stability of all the components of the recently assembled MVD, the system test was performed. For the system test the MVD was set up in hall north-west (Jade hall of the PETRA storage ring) on the DESY premises.

The MVD, consisting of a forward and a barrel section equipped with silicon strip detectors, has been described in section 3.2. The MVD was assembled in two halves, as shown in Fig. 6.1. The

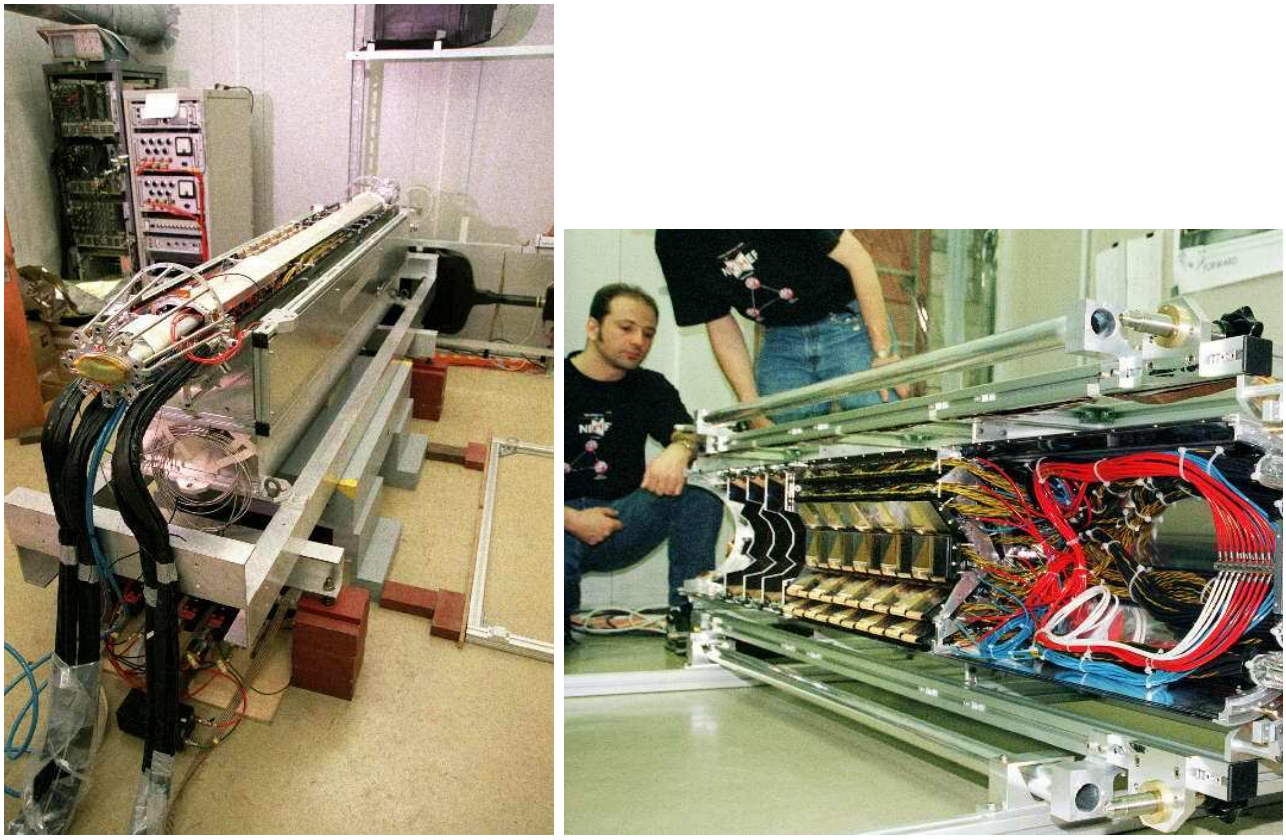

Figure 6.1: *A photograph of an assembly step of the* MVD *in the Jade hall. Here the beam pipe has been inserted into the bottom part of the* MVD*. Afterwards the top half was rotated (shown on the right) and placed on the bottom half.*

completed detector was connected to the readout chain. The scintillator setup, was integrated into the system, providing the option to trigger on cosmic ray induced particles, see chapter 5. After the parameters for stable operation of the detector had been determined, $2.5 \cdot 10^6$ muon events were recorded during a three week period of 24 hour data taking.

This section shortly describes the test setup and the computer control, excluding the setup of the scintillator trigger, which has been described in the previous section. A description of the signal processing and readout of the scintillator trigger is given: Particles simultaneously inducing signals in two trigger layers enclosing the MVD must also have passed the MVD. If such a coincidence signal occurred, a trigger signal was transmitted to the data acquisition (DAQ) system and the detector was read out.

After outlining some of the studies and tests performed at the test site, some facts concerning the system test data taking are summarised and the pedestal and noise levels of the MVD are shown.

6.1 System test setup

The system test was set up in hall north-west on the DESY premises. The MVD, several slow and run control computers (see sections 6.2 and 6.3) as well as the scintillator coincidence trigger and most of the readout and supply electronics required for the trigger, were positioned in a tent ventilated with clean, dry air. The readout and supply racks for the MVD were placed outside the tent.
The MVD was transported from the NIKHEF Institute to DESY in a specially designed support structure which also served as support platform for the MVD during the system test [22]. A 20 cm thick iron block was placed above a lower layer of scintillators (the scintillator trigger and its setup is described in chapter 5) to absorb low energy particles before they could contribute to a trigger signal. Muons with an energy up to ~ 200 MeV are absorbed. On this iron block, the support structure was placed in an additional aluminium frame to hold the scintillators. The finished setup is shown in Fig. 6.2 At the rear side of the MVD, 4 patchboxes were placed and connected to the detector via the so called Combo cables, described in section 3.2.1.
The readout racks outside the tent were equipped with the necessary supply and readout electronics and computers as well the cooling system. The electrical connections to the patchboxes and the water connection to the MVD was installed. The corresponding components (e.g. ADCs) are described in section 3.4.2.
An additional rack was placed close to the readout racks mentioned above, containing the NIM and CAMAC logic units to include the scintillator trigger in the readout chain. This setup is explained in section 6.4.

6.2 Slow control

During the system test, the prepared DAQ and monitoring programs were adjusted and refined until stable operation of the detector was possible.

Two main software parts exist, one of which is the Slow control. It is a package of programs including a graphical user interface (GUI) to control/set and monitor all low and high voltage

Figure 6.2: *A photograph of the system test setup in the Jade hall. The* MVD *is hidden behind the dark grey plastic light shielding enclosed by the scintillators. The black cables emerging from the light shielding are the Combo cables inside the shielding zipper tubes (section 3.4.2). They are led towards the patchboxes which can not be seen here. Close to the tent "wall" the Forward scintillators are positioned on their separate support. On the left of the setup the primary coincidence logic modules as well as the power supplies for the photomultipliers are situated in two racks (the different parts of the scintillator system are explained in section 5.3).*

parameters of the MVD as well as the cooling and several environment sensors.
This includes the settings of

- low voltage: power supply for the front end readout chips
- high voltage: bias voltage for all silicon diodes

and monitoring of

- all low and high voltage levels
- dark currents through the diodes

- temperature at different places in the MVD
- humidity

6.3 Run control

The second software part is the Run control. It also is a package of programs including a GUI which is used to define and survey all run configurations. Before a run is activated, several configurations are set and sent to the detector and the readout electronics (e.g. trigger type, calibration file, configuration file).
Monitoring of several data streams is possible, including:

- ADC data (pedestal suppressed data from single strips)
- calibration data (noise, pedestals per channel)

For the duration of the system test, histograms were available to monitor the scintillators and the relative timing of scintillator coincidence signal and the clock signal.

A trigger event display has been prepared, which is shown in Fig. 6.3.

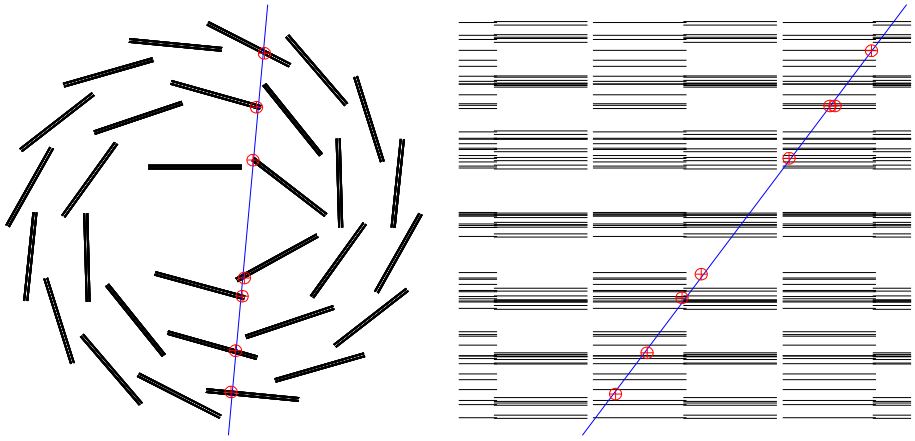

Figure 6.3: *A cosmic ray induced event. It was reconstructed using a version of the* GTT *[25] modified for standalone* MVD *cosmic running with no magnetic field and plotted using the* MVD *online event display [26].*

6.4 The trigger and readout

The readout of the MVD in the system test was realised as described in section 3.4. The signals coming from the front end readout chips HELIX were transmitted via the patchboxes to the readout racks outside the tent where they were digitised by the ADCs.
As the scintillator coincidence setup was present in the system test only, the processing of the scintillator signals (coming from the photomultipliers attached to the scintillators) is described

here. It will be described, how the trigger signal was build to be send to the MVD readout. As mentioned before, information concerning the trigger, in particular a measure of the time between a trigger and the next clock pulse (to which the MVD readout is synchronised) and the coincidence signal releasing scintillators in that event, was recorded for each event. A brief description of this readout is given as well.

Primary coincidence logic

To form a coincidence trigger signal, the pulses coming from the photomultipliers were led through a chain of logic electronics set up from NIM modules. In Fig. 6.4 a sketch of the trigger logic is shown. After passing the fan in fan out modules, the signals of all channels were

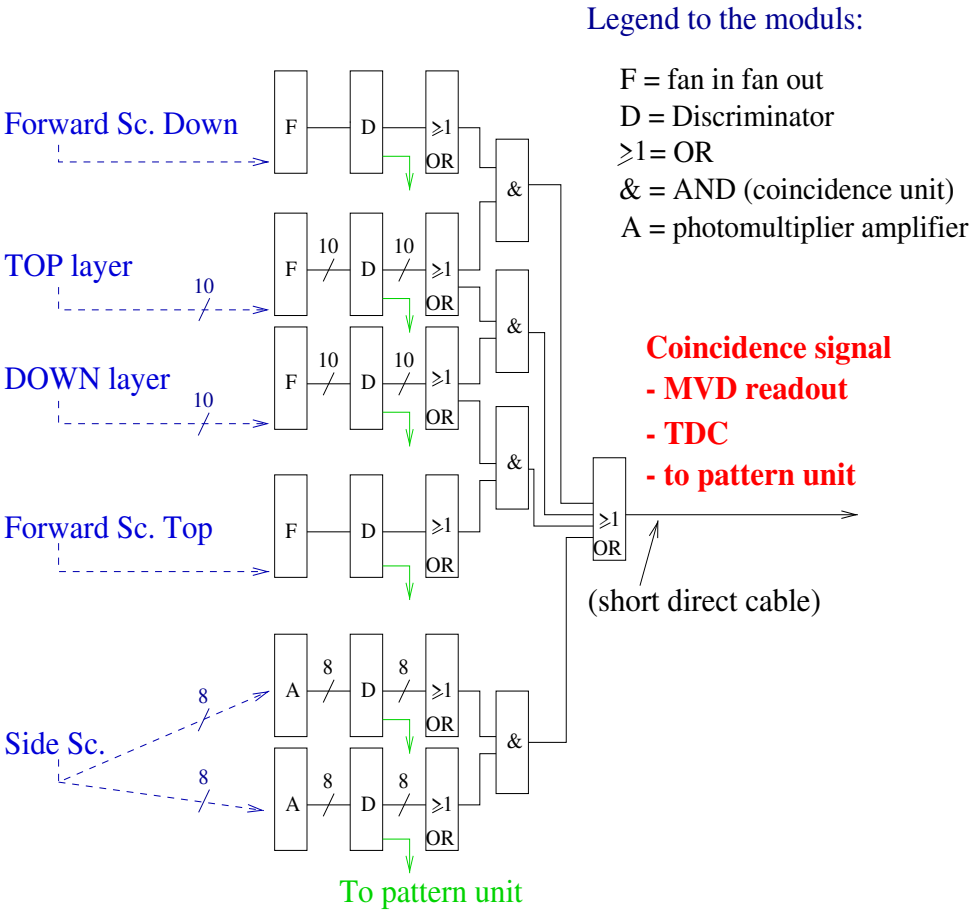

Figure 6.4: *The scheme of the trigger logic. The photomultiplier signals coming from the separate layers are indicated by the dashed arrows. Fan in fan out modules served as impedance converters. The discriminators converted the analogue signal to a digital* NIM *signal (length: 20 ns) whenever it surpassed a given threshold. The* OR *units sum the signals of layers (e.g. the* TOP *layer). Coinciding signals at the AND units resulted in the transmission of a signal to the* MVD *readout. A slashed connecting line with a number n given stands for n similar signal connections. No fan in fan out modules were used for the Side scintillators, to make up the delay introduced by the usage of photomultiplier amplifiers. The 3rd layer is not included in this picture as it was not used for trigger purposes.*

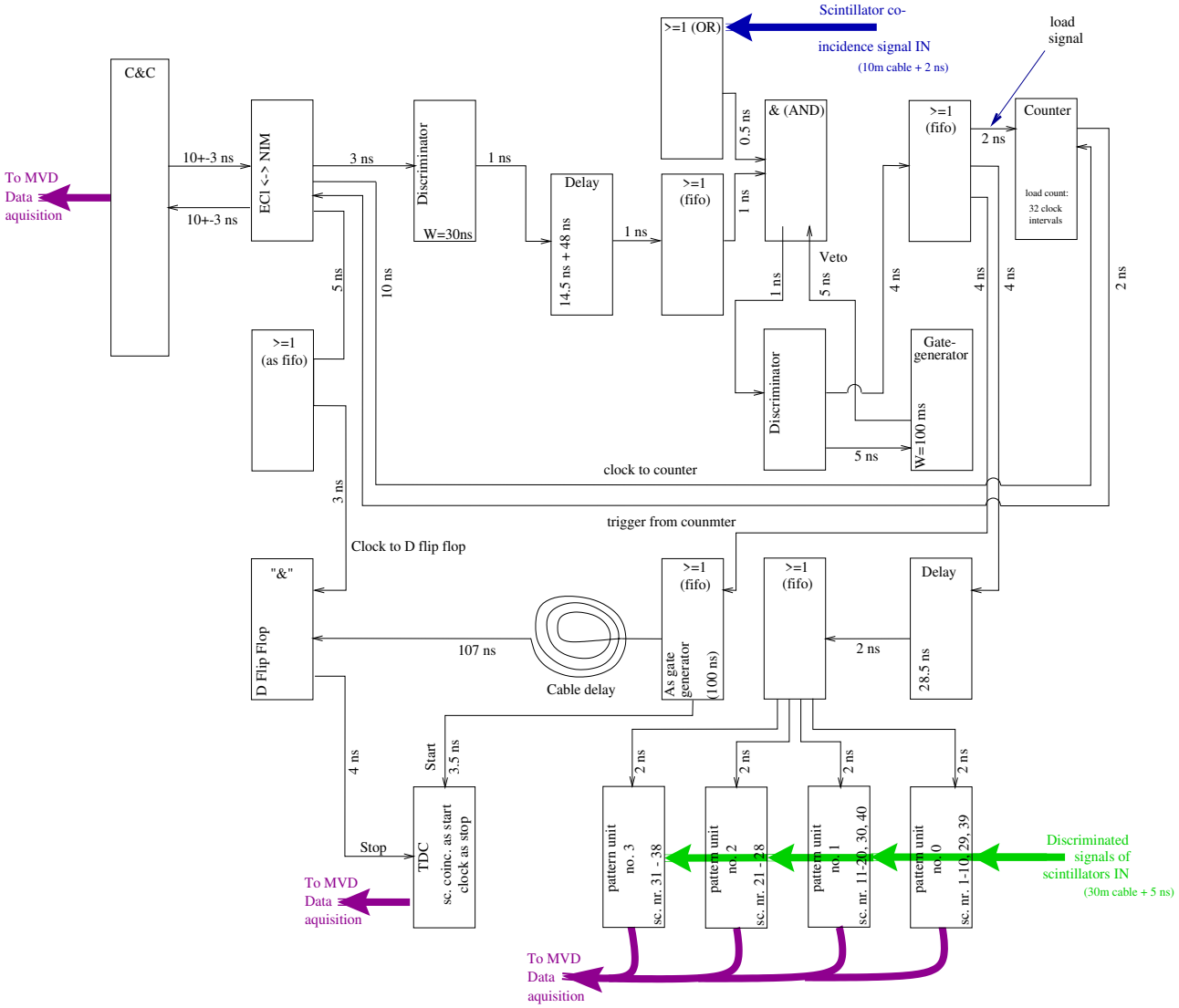

Figure 6.5: *A detailed sketch of the trigger and data acquisition arrangement of* NIM *and* CAMAC *units set up close to the* MVD *readout and supply crates in the Jade hall. The incoming scintillator coincidence signal (top right corner) is processed via diverse* OR, AND, *delay etc. units to finally: 1) release a trigger signal to the* MVD *readout (top left output) after coincidence with the clock in an adjustable time window (from 3 to 96 ns), 2) start the time to digital converter which is stopped by the next clock pulse and 3) act as gate for the pattern units which record the incoming discriminated scintillator signals while gated (gate width: 20 ns).*

discriminated. A threshold of 500 mV for the TOP / DOWN layer scintillators and of ~ 30 mV for the Side and Forward scintillators was chosen, explained in more detail in section 5.3. Any analogue signal (average height: ~ 3 V for the TOP / DOWN layer scintillators, ~ 200 mV for Sides and Forward scintillators) passing this threshold led to the generation of a 20 ns long NIM signal.
The discriminated signals originating from one logic unit of scintillators (e.g. the TOP layer) were merged into one signal by using OR units. The signals from the Forward scintillators did not need to be merged (as the "layer" contained only one scintillator) but were led through OR

units to conserve equally long signal propagation.
The logic sums of the signals of one layer were then brought together at AND modules. For instance it one scintillator of the TOP *and* one scintillator of the DOWN layer emitted a signal at the same time, i.e. in a time window of approximately 36 ns, a coincidence signal was generated. As can be seen in Fig. 6.4, a coincidence was built for the following sets of scintillators:

- TOP with DOWN layer
- TOP layer with Forward Down scintillator
- DOWN layer with Forward Top scintillator
- Side left with Side right

At the beginning of the system test, a reduced set of scintillators was used to trigger the MVD readout. The set was formed by the central two scintillators of the TOP and DOWN layers, allowing a small hit volume in the MVD and thus simplifying the starting of the systematic detector and readout studies.

All coincidence signals were combined at a final OR, to yield the final scintillator coincidence signal. This signal was then sent to the NIM / CAMAC rack outside the clean tent, where it was processed further.

The individual timing of all channels was adjusted, by means of varying the cable lengths, to an overall precision of better than 10 ns. The sources of time shifts in signal arrival times, was the usage of different types of photomultipliers and the adjustment of the photomultiplier supply voltages to achieve similar gain for all comparable scintillators (see section 5.3) as the transit time of the electron cascade in the photomultiplier is dependent on the applied high voltage.

Secondary readout logic

Additionally to the generation of a coincidence signal, the cosmic trigger setup contributed to the system test data stream:

- The discriminated signals of the scintillators contributing to the coincidence signal were recorded using pattern units.
- The time between the coincidence signal and the following pulse of the $\sim$ 10 MHz clock was measured and stored in the data stream using a time to digital converter.

This information was put to use in the data analysis.

The realisation of this signal processing (by modules placed outside the clean tent) will not be explained in detail. Only the most important parts of the electronic setup are summarised here. Fig. 6.5 shows a detailed sketch of the readout circuit. The incoming scintillator coincidence signal serves 3 tasks:

1. Provide a trigger signal to the MVD readout after coincidence with the clock signal.

2. Activate the time to digital converter. The stop signal was given by the leading edge of the subsequent clock pulse
3. Act as gate for the pattern units (gate width: 20 ns). These recorded the discriminated signals of the scintillators having generated the coincidence signal.

To achieve the *first task*, the scintillator coincidence signal had to "coincide" with the clock in a given adjustable time window. This is necessary because the readout of the MVD is optimised for the HERA bunch crossing time. As electron and proton bunches collide every 96 ns in the HERA collider, the MVD pipeline buffer is filled synchronously with this frequency. If a particle arrives before the nominal *ep* pair collides in HERA, the MVD readout chip stores the value of the pulse from the pulse shaper at an early state, where it has not reached its maximum (see Fig. 3.12). This is of course only a problem for cosmic ray induced particles, as they are uniformly distributed in time. For the data taking in the ZEUS detector the MVD can be tuned to the bunch crossing time.

To be able to correctly interpret the pulse height in the cosmic test, two approaches were possible: Either one could slim the coincidence window (of scintillator signal and clock), or one could broaden up the coincidence interval and record the relative timing, yielding a much higher rate of events. The last approach was realised during the system test.

The coincidence time window was therefore varied during the system test. To find the correct pipeline column of the HELIX chips, a full time window (96 ns) was allowed at the beginning, to be able to detect any signal in any of the scanned pipeline columns. All triggered events were recorded with these settings, also many "off time" events. In the final data taking period, the amount of data was reduced by requiring a time window of approximately ± 15 ns.
The final trigger was released in constant phase with the clock. This was realised by sending the coincidence signal to a counter. The signal loaded a number of counts to this counter, which was subsequently counted down with the rate of the also attached clock. At countdown finish, a trigger signal was send, now in phase with the clock.

To achieve the *second task* a CAMAC TDC was used. It determines the time interval between a coincidence signal and the following clock pulse acting like a very sensitive stop clock. The start signal was given by the scintillator coincidence pulse, the stop by a following clock pulse. The clock pulse had to be delayed by 25 ns because the TDC used could only record minimal intervals of 25 ns. After each event the TDC was read out by the DAQ electronics.

The CAMAC pattern units, used for the *third task*, were able to record NIM signals applied to their 16 inputs in a time interval given by the gate signal. As long as the gate signal was active, all pulses arriving at the input channels were stored and subsequently read out and reset. As the scintillator coincidence signal was used as gate, it had to be timed to the arrival of the discriminator pulses of the corresponding scintillators. This was done sending test pulses through the electronics, simulating two continuously firing scintillators. The timing was adjusted using a cable delay unit. The difference in time of arrival of the coincidence signal and the discriminator signal was due to the different signal paths. They branched at the level of the discriminators. One discriminator channel output was led (via 30 m BNC RG-58 cables) directly to the pattern units, while the other branch passed the OR and AND units of the primary logic chain, a 10 m (BNC RG-58, labelled "short direct cable" in Fig. 6.4) cable, as well as several modules of the secondary chain.
The gate signal length was set to 20 ns by means of a discriminator.

6.5 Detector checks

The system test preparations started with tests of a single prototype ladder. The device was operated mainly in 3 trigger modes (random, radioactive source, cosmic particles) making use of a partly set up readout chain. The random trigger mode supplied information mainly on the noise and readout electronics. Runs triggered by scintillators with γ rays from radioactive sources as well as cosmic ray induced particles delivered information on the silicon response. Further tests were performed using the build in HELIX test pulse mechanism, yielding information on the front end readout electronics and the readout chain. These tests served mainly to test the readout electronics and will not be described any further.

After the ladder test, the assembly of the top half of the MVD was finished and it could be transported to DESY. Before it was carefully connected to the patchboxes, that had been installed and cabled to the readout racks during the ladder test, the primary test (scope test) was performed on all modules. This test concerned the HELIX readout chips. Each module was supplied with voltage and programmed using an external programming board. The response of the chip to steering signals was observed on an oscilloscope. Modules not responding as expected were examined more closely later on. Some of these modules could be repaired, as their malfunction was e.g. due to bad electrical connections.

Subsequent to the scope test, laser alignment tests were performed. Along the MVD support structure, several laser sensors are placed [27]. A laser at the rear of the MVD emits a beam relative to which the movement of parts of the detector can be determined. Movements of the detector components of less than 10 μm in z were measured after the transport.

The behaviour of the dark current in the MVD modules was observed for different high voltage settings. Some modules were found to have rising dark currents starting from a certain voltage level [28].

Several other checks were performed (e.g. timing studies) that have not been mentioned here.

6.6 Data taking

Some facts concerning the system test data taking period are summarised in this section.
During three weeks of 24 hour data taking, 2.5 10^6 cosmic ray induced events were recorded (run numbers from 4877 to 5474).
In this time, different configurations of the detector and the readout were realised, some of which shall be mentioned here. The online cluster algorithm applied by the ADC is summarised. and the pedestal and noise behaviour of the MVD during the system test is shown at the end.

High voltage

One detector parameter was the bias voltage applied to each half module. In the beginning of the system test, the same bias voltage was applied to all half modules, independent of the individual depletion voltages. This global value was varied between 50 V and 75 V. From run 5373 individual voltage settings were applied, which were adjusted to a final stable setting from run 5434.

Trigger type

One readout parameter was the trigger type. Two groups of triggers were used: random and cosmic.

The **random trigger** was used to obtain data from the MVD without particles passing, e.g. to determine the pedestals and noise [29] of the channels.

The **cosmic trigger** was generated by the scintillator coincidence setup, indicating particle passage. The triggers were subdivided in triggers with different sets of scintillators: one called "high" were all scintillators contributed to the coincidence and one called "low" were only the central two scintillators of the TOP and DOWN layer contributed to the coincidence signal. Additionally triggers with different timing settings (different size and position of the readout window around the $\sim$ 10 MHz clock pulse) were used.

ADC online cluster

A cluster algorithm was applied by the ADCs (online) to reduce the amount of data that had to be stored.

This algorithm [30] required rather loose conditions for a set of strips to be included in a cluster:

- A **strip signal of $>\sim$ 2$\times$noise**, which is $\sim$ 11 ADC counts was required.
  If, in a strip sweep, a strip signal exceeded this threshold, the cluster was assumed to begin at the strip before this one, i.e. the one that had a lower signal. All following strips exceeding the threshold were assumed to belong to the cluster, until one strip fell below the threshold and the one after this did not again exceed the threshold. The cluster was assumed to end with the first strip below the threshold.
- The **sum of the strip signals** in a cluster was required to be **greater than $\sim$ 6$\times$noise** (i.e. 31 ADC counts).
- Additionally the **number of strips in a cluster** was required to be **smaller than 16**.

Only groups of strips meeting these requirements were stored in the data stream.

Masked modules

Three modules were excluded from being recorded (masked) during the system test, as they behaved erratically during the scope tests and could not be repaired. Two others were masked only temporarily [31].

Pedestal and noise behaviour

The pedestal and threshold ($\hat{=}$2$\times$noise) distributions for the barrel and the forward section of the MVD are shown in Fig. 6.6. These distributions are based on the stable individual bias voltage setting. The mean noise of the barrel and forward MVD is close to 5 ADC counts.

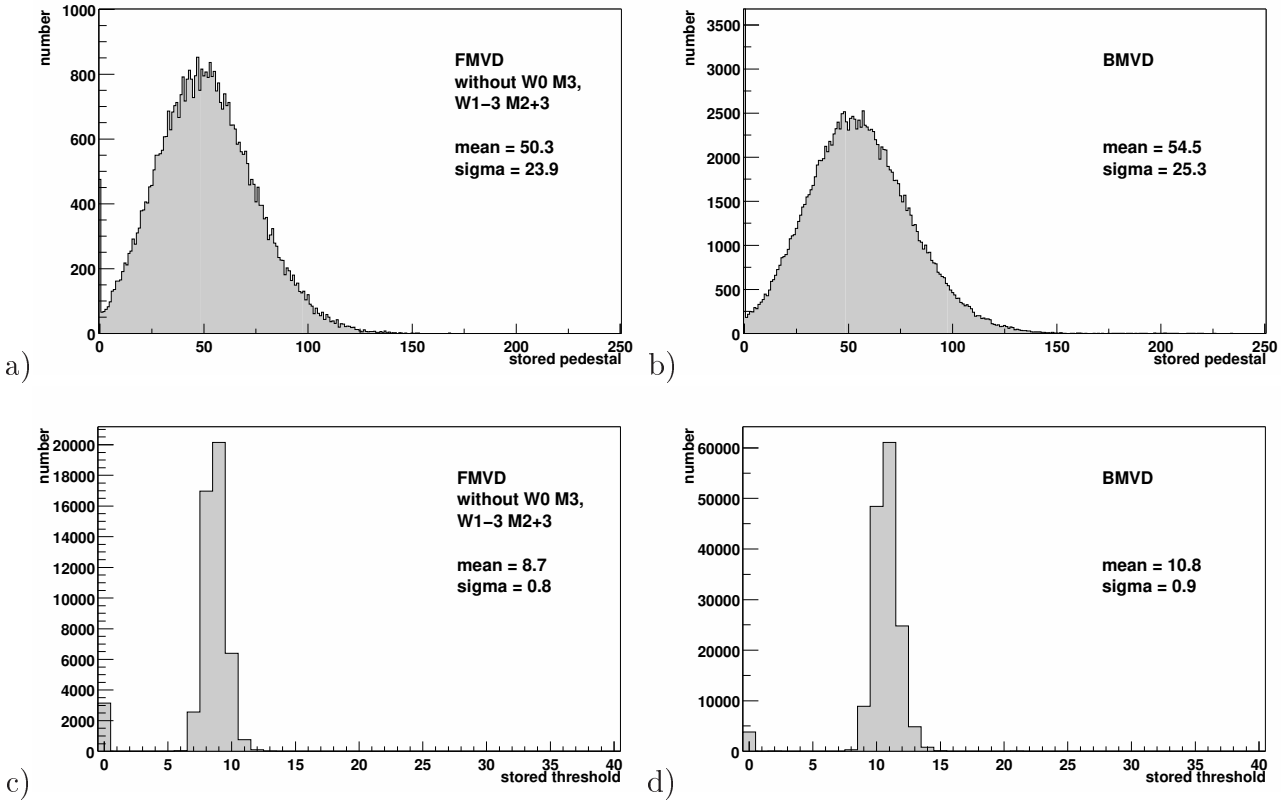

Figure 6.6: *The pedestal and noise-threshold (≙2×noise) values for the barrel and the forward* MVD *section: a) forward pedestal, b) barrel pedestal, c) forward threshold and d) barrel threshold. The sensors were supplied with individual bias voltages for this data.*

All modules were studied concerning the behaviour of the chip-wise pedestal (see section 3.4.2, ADC) and the strip-wise standard deviation from the pedestal values (noise). The study was performed in several measurements with different configurations of the MVD. The most stable configuration was achieved by adjusting the high voltage for the silicon sensors individually.

Chapter 7

System test data analysis

One of the goals of the analysis of the data recorded during the system test was to achieve a good understanding of the functionality of the MVD modules after the assembly steps. For this purpose, the relative number of hits in the forward and barrel section, the relative and absolute timing of the half modules, the distribution of the gain of the halfmodules as well as the MVD sensor efficiency and the resolution were studied.
The analysis presented here concerned mainly the relative number of hits, the relative timing and the distribution of the gain of the halfmodules.

The data used in this analysis contained pre clustered, pedestal suppressed data from all channels per event (including the address), cluster charges, scintillator and TDC data.

Mainly a subset of the total acquired data was used. It was recorded in the runs 5434 to 5474. Constant high voltage settings for each individual sensor, comparable configuration settings and a trigger clock coincidence window of ± 15 ns led to a reliable set of data.
Some modules identified to behave erratic during the scope tests mentioned in section 6.5 that could not be repaired were masked during the data taking. These modules could not be analysed, as no data from them was recorded.

In this chapter, the methods applied to prepare the data for the analysis are presented, followed by the results of the system test data analysis.

7.1 Data preparation

Before the data could be analysed, noisy (bad) channels were found and excluded to avoid distortions in the signal height distributions. Additionally, clusters of strips indicating particle passage were searched for and further cuts enhancing the data quality, using e.g. the scintillator information were applied.

In the following, the detection of bad channels will be summarised briefly. A description of the cluster algorithm applied to find the hits in the detector and the applied cuts will be described.

7.1.1 Investigation of bad channels

The "bad" channels that were rejected during the analysis were detected using two different methods.

One method was to identify the channels that had unstable pedestal behaviour. If a channel was unstable in pedestal, its noise also varied strongly. Some channels with unstable noise behaviour (a number of channels $\mathcal{O}(100)$ depending on the voltage settings) could be identified. In the stable voltage configuration, less than 4‰ of all MVD channels showed such unstable pedestal behaviour. This method and detailed results are presented in [29].

The second method used strip hit maps of those half modules with peaks in their signal distribution to locate the bad channels, as the bad channels generally contributed to a higher number of clusters than properly functioning channels. That way 3 more noisy channels were located. A list of noisy or malfunctioning channels of the MVD during the system test can be found at [31].

7.1.2 Clustering

Two kinds of cluster algorithms were applied to the data, before it was used in the analysis: the online cluster algorithm that has been mentioned in section 6.6 and an offline cluster algorithm, which shall be described here. The restrictions caused by the used algorithm will be explained.

The offline cluster algorithm was applied only to those channels, that had passed the online cluster algorithm. Thus the thresholds of the online algorithm also hold here.

Offline cluster

The applied offline cluster algorithm was a rather simple one. Every single half module was scanned for

- a **cluster seed**, i.e. a strip with a signal **higher than 5×noise** (standard deviation of the pedestal distribution, 25 ADC counts).
- If found, the **sum of the seed and the 2 neighbouring strips** ("clustersum") was required to be **higher than ∼ 6×noise** (32 ADC counts).
- An **identified cluster in** the **outer and inner half module** was required.

The clusters of the inner and outer half modules were stored separately.

Restrictions were caused by this cluster algorithm. For each real hit there exists a ghost hit, as shown in Fig 3.4b. Without a track fit, it is not possible to tell them apart. As the strips of the sensor with the real hit are perpendicular to the ones with the ghost hit, it is unknown whether the angle of incidence of the tracks varied along or perpendicular to the strips. Strongly inclined particle incidence along a strip leads to a high signal on this strip and hardly leads to an increase of the signal on neighbouring strips. A strongly inclined incidence perpendicular to the strip direction leads to a broad cluster of many rather low strip signals as shown in Fig. 7.1. As the cluster width was fixed in size large clusters due to strongly inclined tracks were underestimated in signal height, as depicted by the right cluster in Fig. 7.1.

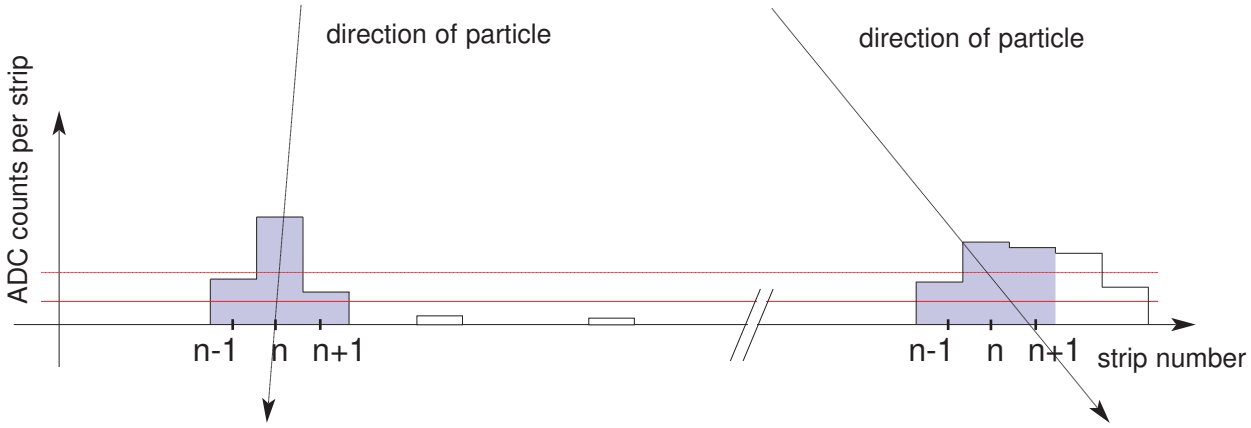

Figure 7.1: *Two clusters for different directions of incidence on the sensor. The left cluster is slim because the incidence is close to perpendicular. The right cluster with strongly inclined incidence is rather broad (also see Fig. 3.10). The shaded area is assumed to contribute to a cluster using the offline cluster algorithm. Thus, in the right case, the clustersum is lower than it should be. The two lines indicate thresholds. The lower one is the noise threshold applied by the online cluster algorithm, the upper one the seed threshold applied by the offline cluster algorithm.*

7.1.3 Cuts

The data used in the analysis was filtered by applying cuts which are summarised here.

Reject clusters containing known bad channels

During the system test, several channels of the detector showed unstable and unphysical behaviour, as is summarised in section 7.1.1. Any cluster containing such channels was rejected and thus did not contribute to the analysis.
Without cutting these channels, about 14% of the clustersum distributions of separate half modules were distorted by spikes and false peaks. The "bad channel" cut removed these distortions from the clustersum distributions.

Reject shower-like events

Events with many particles, e.g. hadron shower events or events with many delta electrons, potentially contain lower energy, non minimal ionising particles. These lead to higher signals than mips, and thus distort the signal distributions. The iron layer was used to absorb low energy particles in the system test setup before they could contribute to the trigger.

To further reduce the number of clusters due to these events, a cut on the scintillator pattern was performed. Shower-like events are likely to produce signals in more than two scintillators, so events with more than 1 scintillator per layer (e.g. the TOP layer) and more than 2 scintillators in total were rejected. The result of the cut is shown in Fig. 7.2.

a) b)

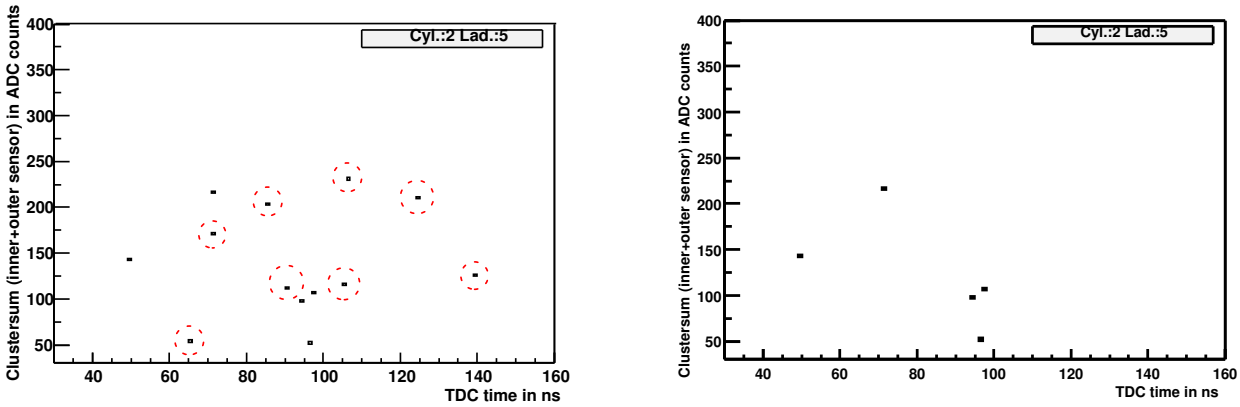

Figure 7.2: *Plots of single strip signals of one ladder versus the recorded* TDC *time for a broad time window of* 96 *ns in run nr.* 5059*. a) without b) with shower cut. A set of scintillators has been requested, so that the ladder shown should not have any hits (noise only). When using the shower cut, several entries due to sprays of particles in the detector (marked with dotted circles) vanish. At the time this plot was produced, the bad channels were not yet known; the remainder of the entries is due to these.*

Reject invalid scintillator patterns

Some events were recorded, in which the scintillator information was not reliable. This included events, were only one scintillator was recorded, and others with 2 or more scintillators of layers, that did not correspond to a coincidence signal. These entries were likely to be due to random inefficiencies of the patten units. All such events were rejected.

Forward scintillator hit requirement

From Fig. 5.3b it is clear that only particles passing the Forward scintillators lead to reasonable tracks through the forward MVD. Thus a hit in one of the Forward scintillator panels was required when the forward section of the MVD was surveyed.

7.2 Results

In this section, the results gained by analysing the data described in the last section are presented.

7.2.1 Efficiency comparison of barrel and forward section

To be sure, that the barrel and the forward section have similar efficiency and are generally working, a study of the expected ratio of hits in the barrel section to hits in the forward section was performed.

Different sections of the MVD were triggered by different sets of scintillators, as described in section 5.2. Assuming that the TOP / DOWN triggers only yield tracks in the barrel section and the Forward triggers yield tracks in the forward section only, one can roughly estimate the ratio of the number of tracks in the forward section to the number of tracks in the barrel section. The estimated track ratio is

$$\frac{f_{\mathrm{T/D}}}{f_{\mathrm{F_T/D}} + f_{\mathrm{F_D/T}}} = 8.5\ \%$$

With the separate rates $f_{\mathrm{X/Y}}$ of the different sets of scintillators:

$$f_{\mathrm{T/D}} \sim 12.88\ \mathrm{Hz} \quad \bullet \quad f_{\mathrm{F_T/D}} \sim 0.43\ \mathrm{Hz} \quad \bullet \quad f_{\mathrm{F_D/T}} \sim 0.67\ \mathrm{Hz}$$

This ratio does not give a correct estimate of the ratio of hits in the forward and barrel section, as the number of sensitive planes per track as well as the geometrical efficiency of the separate trigger paths is neglected. The assumption, that Forward scintillator triggers exclusively lead to hits in the forward MVD section also leads to inaccuracies.
The estimation can thus be improved by estimating and including the geometrical efficiency as well as the number of planes per track.

The geometrical efficiency can be estimated by projecting the observed section of the MVD (forward or barrel section) to the scintillator coincidence area, indicated by the hatched area in Fig. 7.3, yielding the effective trigger area. The ratio of the coincidence area and the effective trigger area is a measure on the geometrical efficiency.

The number of hits per track in the separate sections can be estimated by projecting and summing all sensor planes of the MVD sections to the scintillator coincidence area.

These separate steps are explained in the following.

- Estimate the effective trigger area:

  $A_{\mathrm{trig\ X/Y,}\ \mathit{eff}}$ is the area in the plane perpendicular to the trigger releasing muons (scintillator coincidence area) where detector components are present (see Fig. 7.3):
  The plane between two scintillators ($A_{\mathrm{coinc.\ X/Y}}$) is larger than the projection of the detector to that plane $A_{\mathrm{trig\ X/Y,}\ \mathit{eff}}$. Calculating the effective trigger area the effective flux ϕ_{eff} can be calculated from the known scintillator coincidence rate $f_{\mathrm{X/Y}}$:

$$\phi_{\ eff} = f_{\mathrm{X/Y}} \cdot \frac{A_{\mathrm{coinc.}}}{A_{\mathrm{dead\ X/Y}}}$$

The number of hits is assumed proportional to $\phi_{\ eff}$.

- Project sensitive material covered area to effective trigger area:
  The total number of hits increases with the number of modules crossed by a track. This number is given by the projection of all sensitive detector areas to the coincidence plane. If a sensor is perpendicular to the incoming muon, its complete area A_{sensor} can be assumed to contribute to the number of hits, whereas if it is inclined by an angle $(90° - \alpha_{\mathrm{X/Y}})$ only $\cos(90° - \alpha_{\mathrm{X/Y}}) \cdot A_{\mathrm{sensor}}$ can be counted. The number of hits therefore is proportional to $\cos(90° - \alpha_{\mathrm{X/Y}}) \cdot A_{\mathrm{sensor}}$.

The ratio of the number of hits in the two sections of the detector was assumed to be proportional to:

$$\begin{aligned}
\left.\frac{N_{\mathrm{hits,\ forward}}}{N_{\mathrm{hits,\ barrel}}}\right|_{\mathrm{estimated}} &\propto \frac{\phi_{eff,\ \mathrm{forward}} \cdot A_{\perp,\ \mathrm{forward}}}{\phi_{eff,\ \mathrm{barrel}} \cdot A_{\perp,\ \mathrm{barrel}}} \cdot \underbrace{\left(\frac{\mathrm{efficiency}_{\mathrm{forward}}}{\mathrm{efficiency}_{\mathrm{barrel}}}\right)}_{\equiv 1} \\
&= \frac{N_{\mathrm{hits\ T/F_D}} + N_{\mathrm{hits\ D/F_T}}}{N_{\mathrm{hits\ T/D}}}
\end{aligned}$$

$$\begin{aligned}
N_{\mathrm{hits\ X/Y}} &= \underbrace{\phi_{\mathrm{X/Y}} \cdot \frac{A_{\mathrm{trig,\ }eff}}{A_{\mathrm{dead\ X/Y}}}}_{=\phi_{eff}} \cdot \frac{A_{\perp\ \mathrm{X/Y}}}{A_{\mathrm{trig,\ }eff}} \\
A_{\perp\ \mathrm{X/Y}} &= A_{\mathrm{sensor}} \cdot \left(\sum_{\mathrm{sensors}} \cos(90° - \alpha_{\mathrm{X/Y}}) \right)
\end{aligned}$$

The angle $\alpha_{\mathrm{X/Y}}$ is the tilt in φ (ZEUS coordinate system, polar coordinate, see Fig. A.1) of the ladder for the barrel section estimation and the angle between the average muon and the horizontal in the forward section estimation (see Fig. 7.3). For the forward section, the sum is not needed. $A_{\mathrm{trig}\ eff}$ and $A_{\mathrm{dead\ X/Y}}$ are explained in Fig. 7.3.

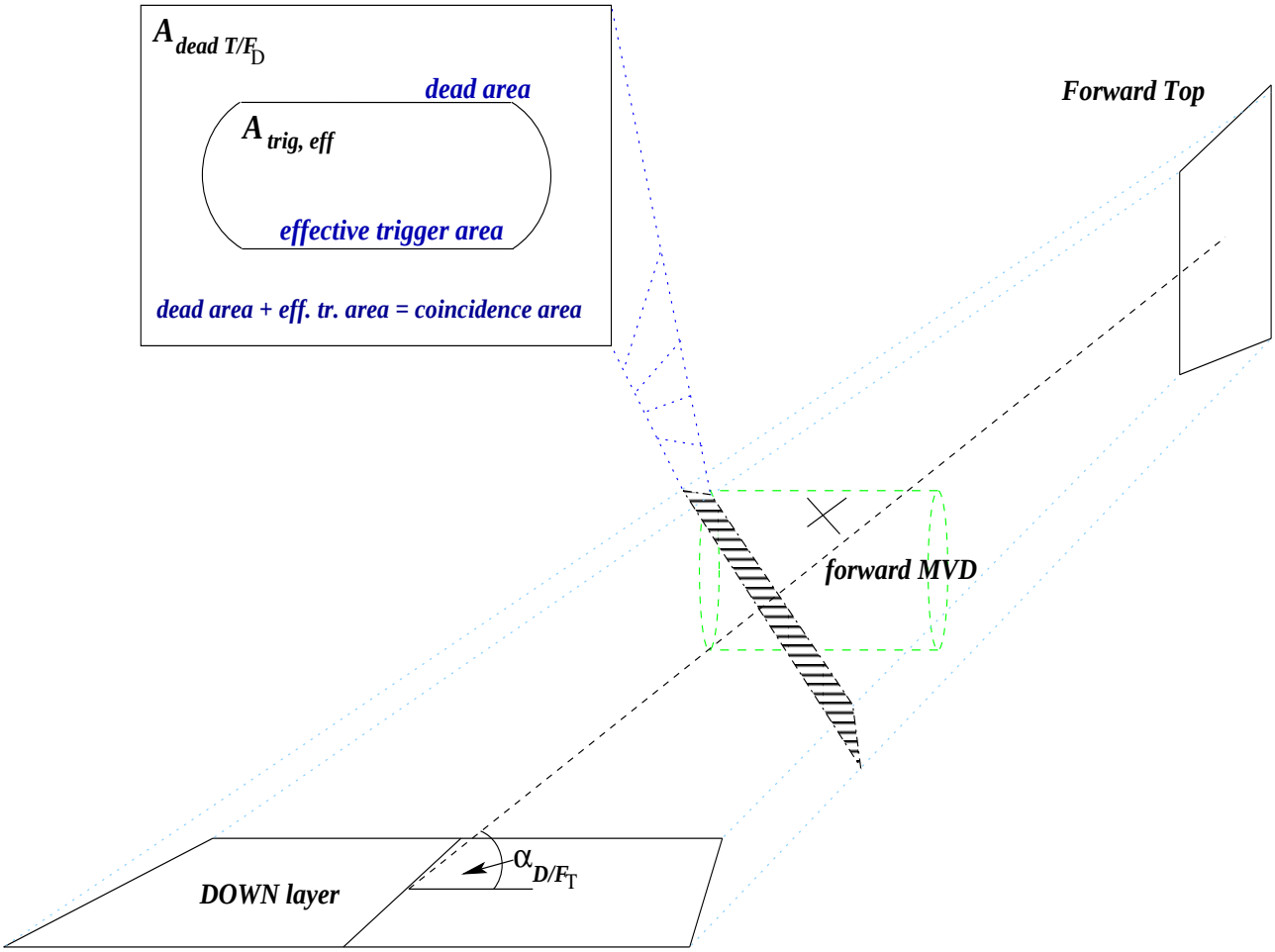

Figure 7.3: *Illustration of the parameters used for the estimation of the forward to barrel hit ratio. The cylinder labelled "forward* MVD*" symbolises the volume spanned by the 4 wheels. A blowup of the hatched plane is shown in the top left corner: the "effective trigger area" is the projection of the cylinder to the "coincidence area" perpendicular to the average passing muon.*

Using these assumptions a value for $N_{\text{hits, forward}}/N_{\text{hits, barrel}}$ was estimated:

$$\left.\frac{N_{\text{hits, forward}}}{N_{\text{hits, barrel}}}\right|_{\text{estim}} = 1.8\ \%$$

The measured ratio of hits / clusters in the forward section to those in the barrel section was found to be:

$$\left.\frac{N_{\text{hits, forward}}}{N_{\text{hits, barrel}}}\right|_{\text{measured}} = 1.7\ \%$$

These numbers agree well and show, that the two sections of the MVD behave similarly.

7.2.2 Timing of barrel and forward section

To ensure that the signals of the sensors in the forward MVD section arrive at the same time at the ADCs, a signal time scan was performed. The individual readout timing of the forward and barrel MVD section had to be adjusted individually, as the signal cables (Combo cables) for both sections are of different length. This adjustment was checked.

The time window relative to the $\sim$ 10 MHz clock was set to 30 ns in the set of data used.

The average cluster height plotted versus the time between a coincidence signal and the clock ("TDC time") is a time scan of the peak of the HELIX shaper signal:
If a muon passes at the optimal time relative to the clock, the maximum signal value (the peak of the HELIX shaper signal) is stored in the pipeline buffer (see section 3.4.1). If the muon passes off-time, the shaper signal is shifted relative to the clock and an off-peak value is stored in the pipeline buffer, leading to a lower recorded signal.

The timing settings have to meet two requirements:

- the peak of the shaper signal scan should be centred in the time window and
- the peaks of forward and barrel section should appear at the same time.

If those requirements are fulfilled, the relative timing has been adjusted properly.

A quadratic fit was applied to the data points depicting the mean value of the signal distributions in bins of TDC time, yielding the local maximum of the shape. The encircled fit values (parameter $[p_0]$) give this maximum.

In Fig. 7.4 the result of the time scan is shown.

The two maxima at $t_{\text{TDC, barrel}} = 151.2$ ns and $t_{\text{TDC, forward}} = 152.1$ ns agree within a nanosecond and are entered in the time window. Thus the barrel and forward section have been properly adjusted in the readout timing.

Additionally the same check was performed for each halfmodule (of barrel and forward sector). It was found that the maximum deviation of the peak value of a single module relative to the value given above is less than 8 ns for all modules. This corresponds to a damping of the signal by less than 5%. Thus a correction of the individual timing is not necessary.

7.2.3 The effective angular dependance of the signal size

The angular dependance of the signal size was studied. Signals due to the passage of particles passing the silicon perpendicularly to the sensor surface are smaller than those of strongly inclined passages (see also section 7.1.2). This is due to the longer way the inclined particles have through the sensor. The behaviour can be quantified by assuming the energy loss to be proportional to the particles path in sensitive material, yielding a $\frac{1}{\sin(\text{angle})}$ behaviour. Thus this effect can be used to test the detector. Furthermore it can be used to correct the signal for the influence of the angle of incidence.

To find the angular dependance, the angle of incidence was estimated. Then the signal dependance on the angle of incidence was measured by observing the variation the peak of the clustersum distributions with this angle.

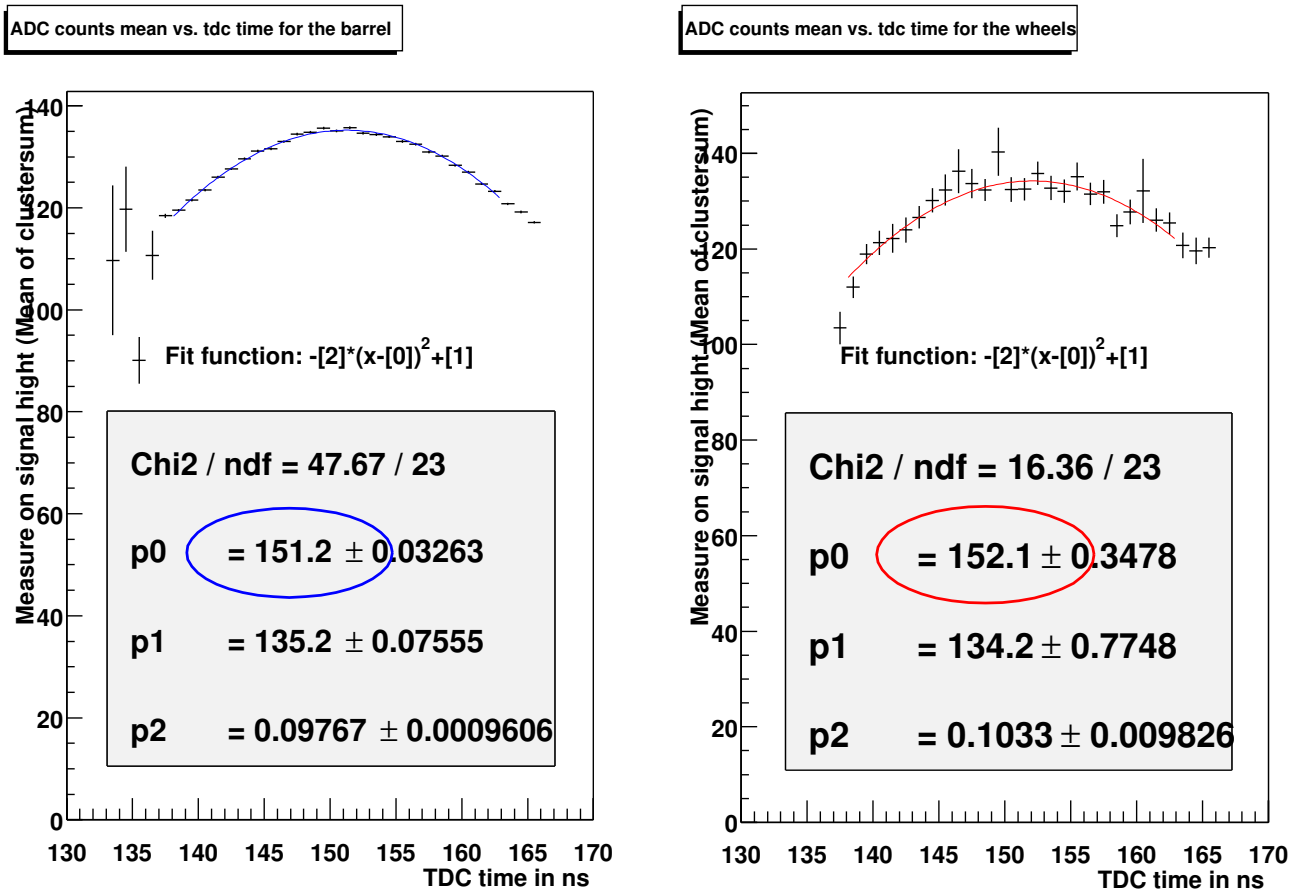

Figure 7.4: *The mean of the clustersum entries for all modules of the barrel section (left) and the forward section (right) versus the time between a coincidence signal and a following clock pulse in nanoseconds. This is a scan of the peak of the* HELIX *shaper signal which is shown in Fig. 3.12. The peaks of the curves of both sections of the* MVD *are in similar positions as shown by the fit parameter* $[p_0]$.

Estimation of the angle of incidence

To estimate the angle of incidence of the trigger releasing particle, the scintillator information was used, as sketched in Fig 7.5. This method, although less precise than an explicit track fit, has the advantage to yield a hit distribution unbiased by track fit requirements.

For each event with detected clusters, the connection line of the centres of the two trigger releasing scintillators was calculated. The spherical coordinate angles θ and φ of this line in the MVD system gave the estimated direction of incidence of the particle. Figure 7.5 shows the estimation of the angle φ.

The extension of the scintillators introduced an uncertainty in the angles which was estimated geometrically, as is described in appendix C.

The purely geometric error estimation yields:

$$\begin{aligned} \sigma_\varphi &\sim 2^\circ \\ \sigma_\theta &\sim 9^\circ \end{aligned}$$

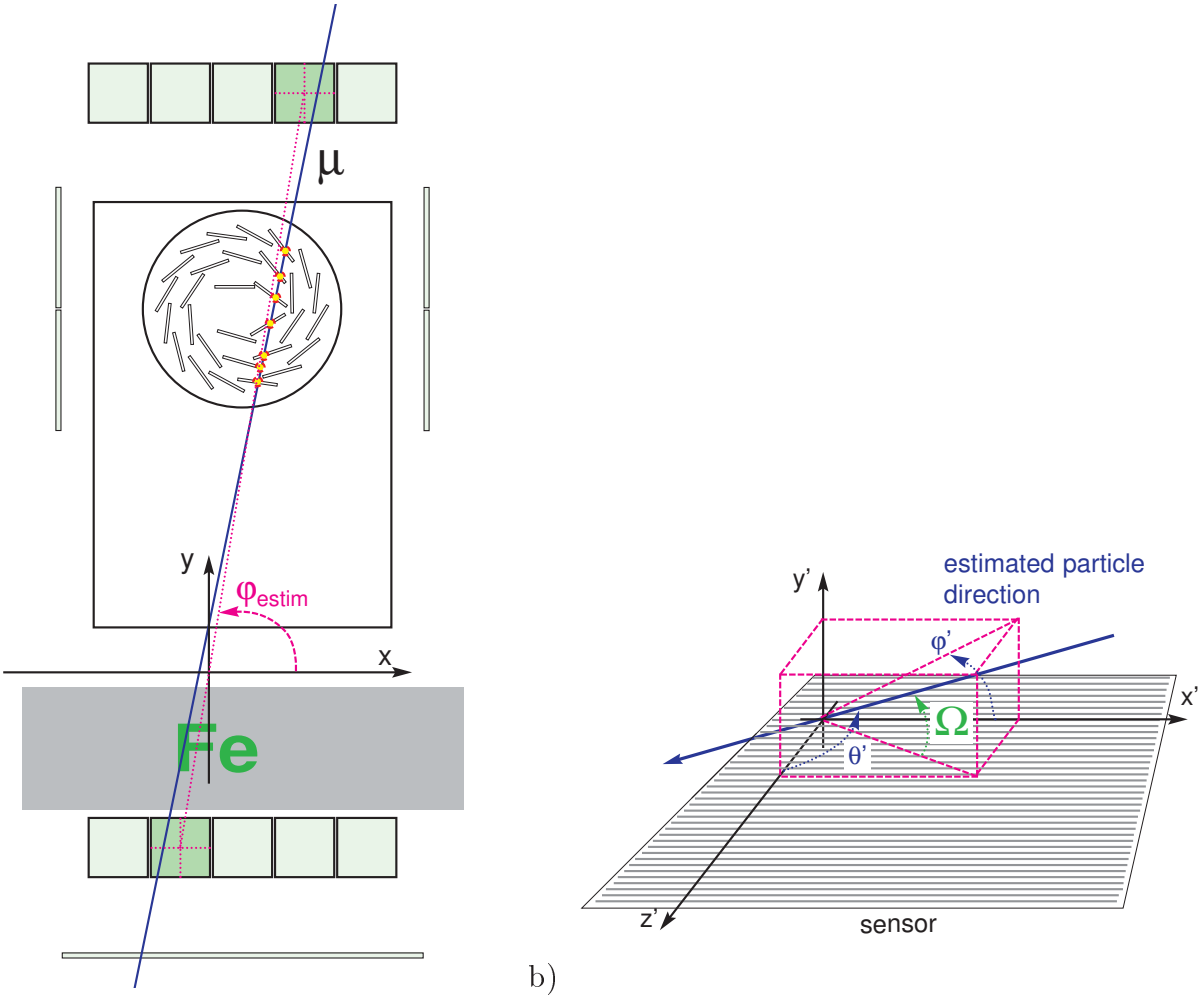

a) b)

Figure 7.5: *a) An xy cut through the test system setup (*MVD *with scintillators). The solid through going line symbolises a passing trigger releasing particle. The dotted connection line of the scintillator centres was used to estimate the direction of incidence. b) A sketch of the angles contributing to the calculation of the solid angle of incidence in the module system* Ω*.*

The error is determined by the size of the scintillators of the TOP / DOWN layer. The extension of the scintillators in z is larger than the extension in x (see Fig. 5.3), thus the spread of the distribution is larger.

From the estimated direction of incidence, the angle of incidence in the module system Ω was calculated, see Fig. 7.5b. This was done for each cluster, as the angle of incidence depends on the orientation of the module. The official MVD geometry description [32] supplied the orientations of all modules α_{lad_i}. First, the angles θ and φ were transformed into the module system (rotation by α_{lad_i} around the z axis), yielding θ' and φ'. From these Ω was calculated (also see Fig. 7.5b):

$$\sin(\Omega) = \sin(\theta')\sin(\varphi')$$

Determination of the angular dependance of the signal size

Knowing the angle of incidence, it was possible to examine the angular dependance of the signal size.
This study was carried out only for the barrel section of the MVD, as the number of entries per "half module" in the forward section was too low. It was performed for the inner and outer half modules separately. As the inner and outer results are essentially the same, all plots shown here are those of the inner half modules.

Notice also that the angle of incidence is measured with respect to the module plane. Thus a passage with a large angle is close to perpendicular incidence while a small angle indicates a steeply inclined passage.

Restrictions are introduced by: The fixed clustersize and neglecting the strip direction relative to the incoming particle, both of which are described in section 7.1.2. The fixed clustersize leads to a loss in signal for steeper tracks which is partially compensated by the neglection of the strip direction. Thus the found angular dependance is called "effective".

Having this "effectiveness" in mind, one can try to choose a reasonable angular range. For this purpose the clustersum mean was calculated in bins of the solid angle of incidence Ω. The result is shown in Fig. 7.6.

As the data looks reasonable down to an angle of $\sim 45°$ the range used for further analysis was chosen to be $\Omega \in [45°,\ 90°]$.

For this range, a more precise approach was chosen to find the angular signal size dependance. Clustersum distributions were filled in 23 2° bins of Ω (resulting in bins 44.5°- 46.5° ... 88.5°-90.5°) and to each distribution a landau fit was applied. The measured peak of the distributions (most probable value, MPV) was again displayed versus Ω. This was performed separately for the inner and the outer half modules. The result of the inner halfmodules is shown in Fig. 7.7. The rise of the signal for smaller angles (steeper incidence) can be seen nicely. To quantify the measured dependance, a fit function f_{fit} was applied to this data.

The fit

For an ideal detector (no dependance on strip direction, complete charge collection) and if the energy loss is proportional to the length of the particle track in sensitive material, the dependance on the angle of incidence Ω would be:

$$\text{signal}(\Omega) = \frac{1}{\sin(\Omega)} \cdot \text{signal}|_{90°}$$

Due to the fixed cluster size introduced by the offline cluster algorithm, due to the dependance on strip orientation and non complete charge collection this dependance is somewhat flattened out. Thus an additive term was used in the fit function, yielding:

$$f_{\text{fit}}(\Omega) = [p_0]\frac{1}{\sin(\Omega)} + [p_1] \tag{7.1}$$

where $[p_0]$ and $[p_1]$ are parameters optimised by the fit routine (using the χ^2 method). The resulting parameters for the inner half modules of the barrel section are shown in the top right corner of Fig. 7.7.

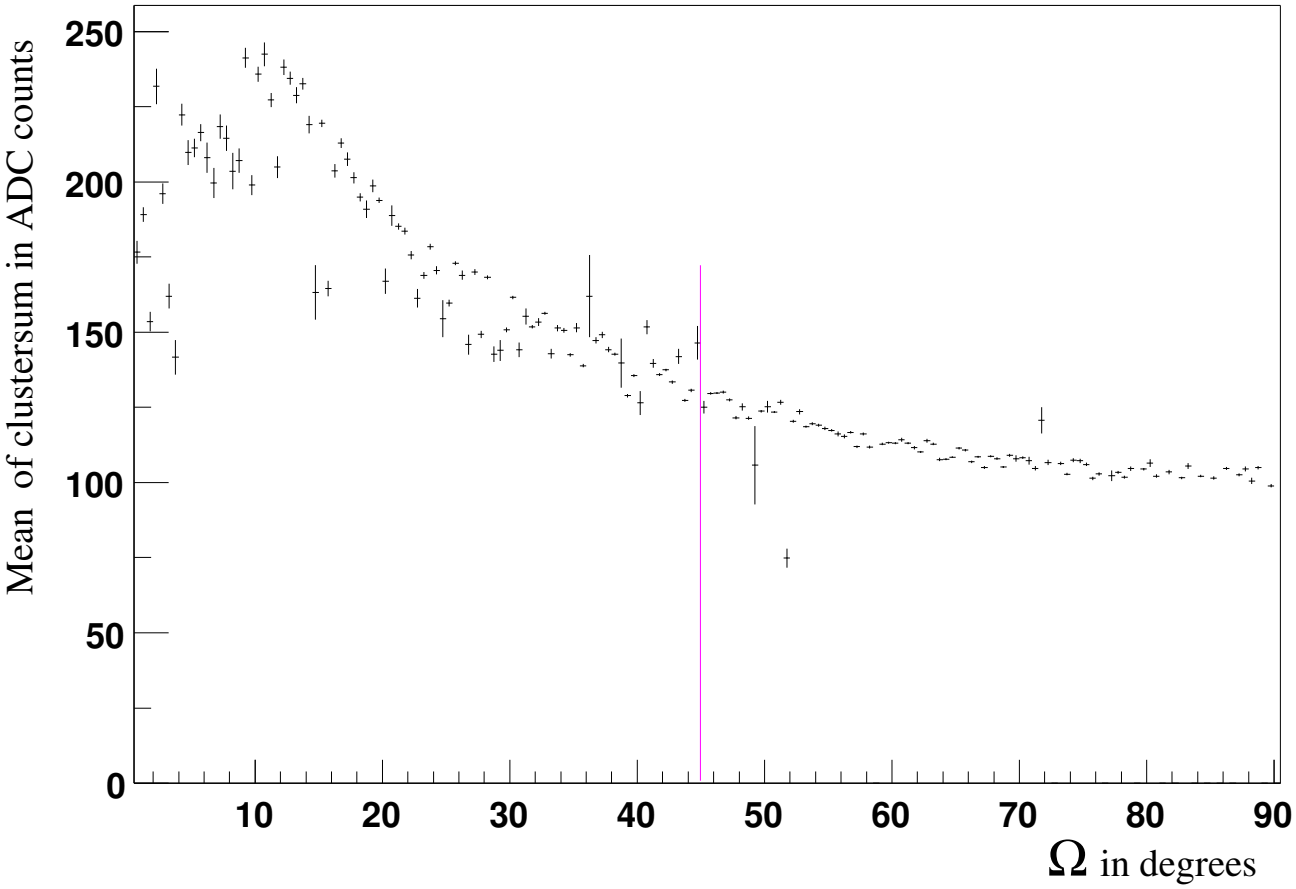

Figure 7.6: *Profile plot of the clustersum (inner half modules) versus the angle of incidence. The data looks reasonable down to an angle of* $\sim 45°$ *(*$90°$ *is perpendicular incidence, i.e. smaller angles indicate steeper passage, see text). For steeper passages the restrictions introduced by the cluster algorithm and by the estimation of the angle of incidence dominate. The estimated angles of incidence are discrete. Certain groups of angles are correlated with groups of modules. The systematics seen clearly for angles below* $45°$ *is due to this correlation.*

The mean of the parameters of outer and inner half modules was determined to be:

$$[p_0] = 63.09 \pm 0.47 \quad (7.2)$$

$$[p_1] = 16.22 \pm 0.21 \quad (7.3)$$

with the error being the experimental standard deviation of the 2 values from the inner and outer half modules. The angular dependance of the detector could thus be determined. As the data is well described by the two parameter fit the expected behaviour is found. The MVD passed this check.

7.2.4 Measurement of the gain distribution

To learn about the variation of the gain averaged per half module and to establish reference values for future studies, a scan of the peaks of the clustersum distributions was performed

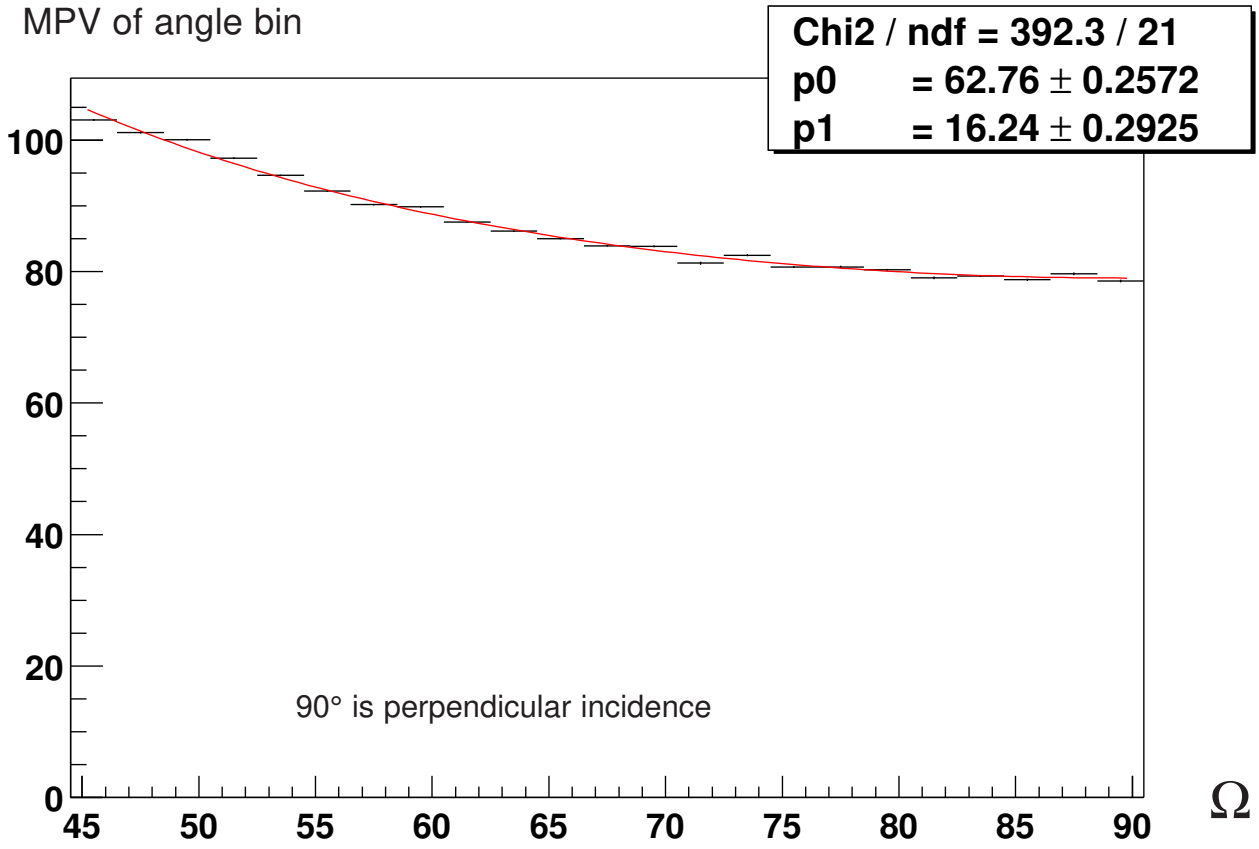

Figure 7.7: *Result of the fits to the clustersum distributions (of the inner half modules) in 2° bins of Ω. The signal rises for smaller angles as expected. The slim grey line shows the result of the applied fit.*

half module wise. As the gain is proportional to the MPV of the clustersum distribution, the MPV distribution gives a measure of the gain distribution.

It is necessary to correct for the angle of incidence. Otherwise half modules standing rather parallel (strongly inclined) to the main particle flux seem to have higher peak values than perpendicular ones (hardly inclined), as more particles cover a longer distance in the inclined than in the perpendicular modules. The behaviour of the uncorrected clustersum distributions is shown on the left two plots of Fig. 7.8. They show the clustersum distributions of half modules standing perpendicular (top plot, hardly inclined) and parallel (bottom plot) to the main particle flux. The distribution of the MPVs without angular correction is shown in Fig. 7.9. The geometry of the MVD obviously dominates this plot.

The angular correction

The determined angular dependance (section 7.2.3) was used to correct the clustersum distributions of all half modules for the angular dependance of the signal. The value of every single clustersum (called "hit" here) was multiplied with a correction factor, depending on the angle

of incidence of this cluster:

$$\mathrm{hit}_{\mathrm{corr}} = \frac{[p_0] + [p_1]}{[p_0]\frac{1}{\sin(\Omega)} + [p_1]} \cdot \mathrm{hit}_{\mathrm{uncorr}} \tag{7.4}$$

The impact of this correction on the clustersum distribution of two half modules is also shown in Fig. 7.8. This correction was performed in the same range of angles of incidence used to

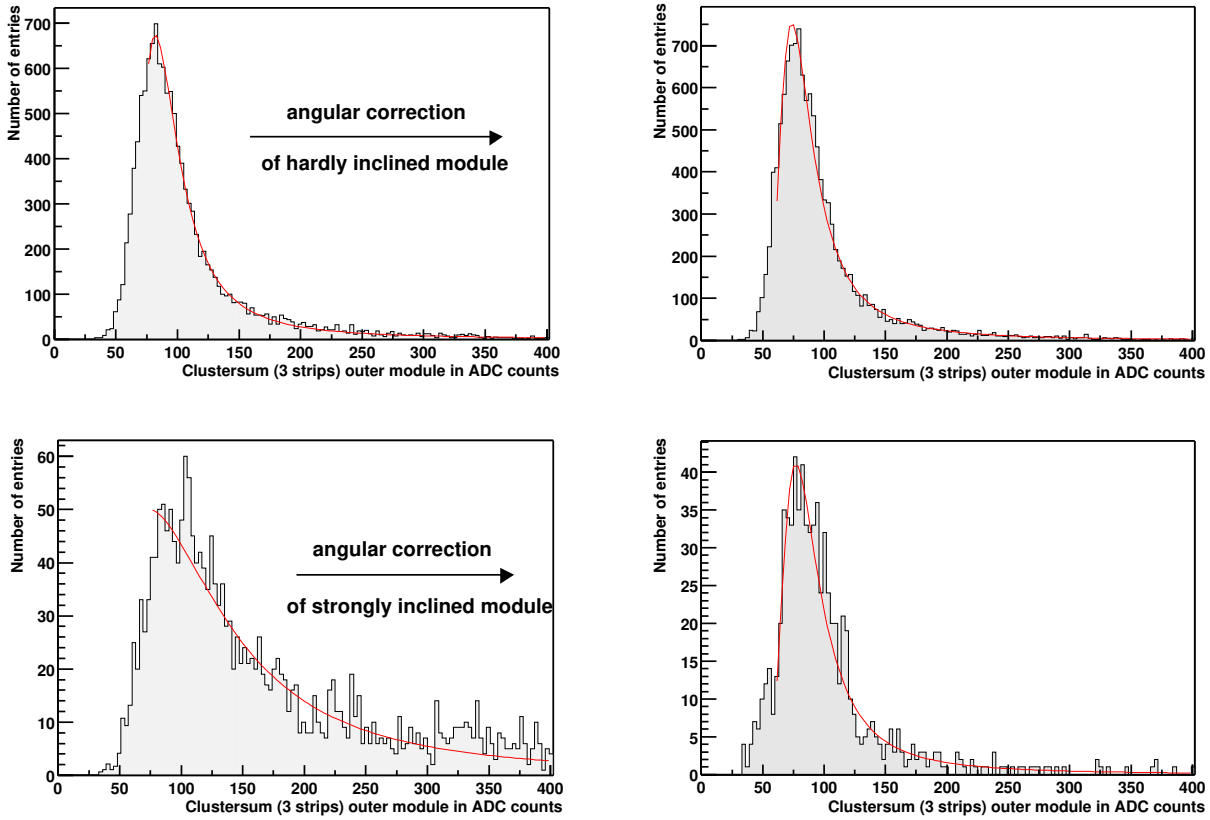

Figure 7.8: *The influence of the correction on the signal height distribution of a half module which is parallel to the* Top / Down *layer scintillators (top plots) and one, that is strongly inclined (lower plots). On the left side two uncorrected clustersum distributions are shown. On the right side the angular corrected distributions can be seen.*

find the angular dependance. The corrected clustersum distributions of all half modules yield a similar shape.

Determination of the peaks of the clustersum distributions

To find the peak of the clustersum distributions, a landau[1] fit was applied to the distribution of every half module, yielding the peak value (Mpv). The fit range was adjusted to the distributions such that the peak was described best.

[1] The landau fit of Root ("successor to Paw") was used.

The result achieved for non angular corrected distributions is shown in Fig. 7.9. Here the MPVs of the landau fits are displayed versus the module number (only outer half modules are shown, module numbers start at the innermost layer). The influence of the arrangement of the modules in the MVD can be seen nicely and the distribution of the values shown on the right is rather broad.

When fitting corrected clustersum distributions for every half module of the barrel section of the MVD, the dependance on the geometry of the MVD vanishes, as shown in Fig. 7.10. The determined MPVs are displayed versus the module number. On the right side of Fig. 7.10, the distribution of the MPVs is shown.

The gain distribution

The MPV distribution shown on the right plot in Fig. 7.10 is of Gaussian shape and rather slim with a standard deviation of 2.4 ADC counts. It peaks at a value of 78.8 ADC counts. As the gain is proportional to the MPV, this distribution corresponds to a distribution of the gain of the barrel MVD half modules with a relative width of 3%. The left side of Fig. 7.10 shows the MPVs for every half module of the barrel MVD (module number). This is a measure on the gain distribution, as the MPVs are proportional to the individual gain.

The determined MPVs using the described angular correction can e.g. be used as points of reference in future tests of the MVD.

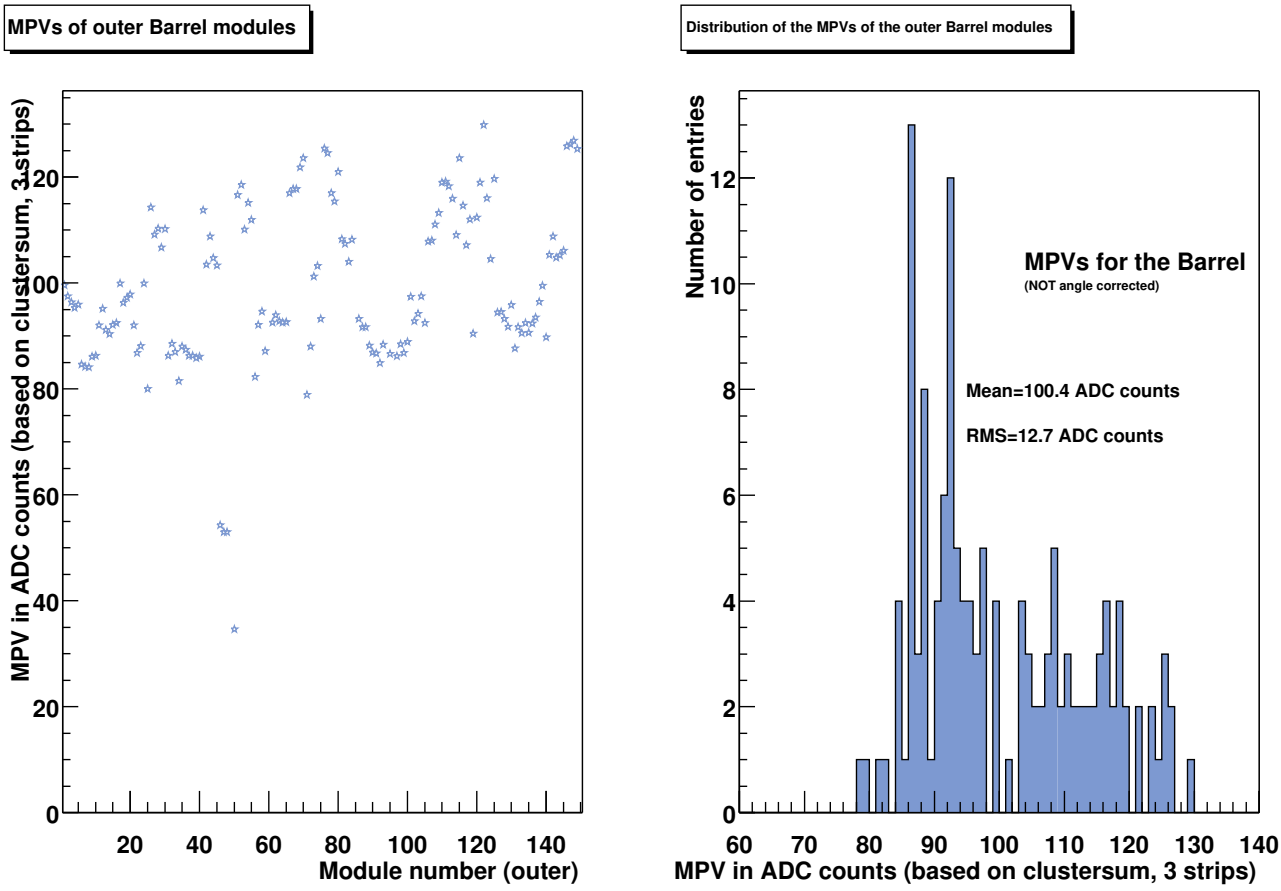

Figure 7.9: *The non angular corrected* MPV *(gain) distribution of the outer barrel half modules is shown here to demonstrate the influence of the angular correction. Without correction the geometry of the* MVD *is recognisable from the left plot and the distribution of the* MPVS *(projection to the* y *axis) shown on the right is rather broad.*

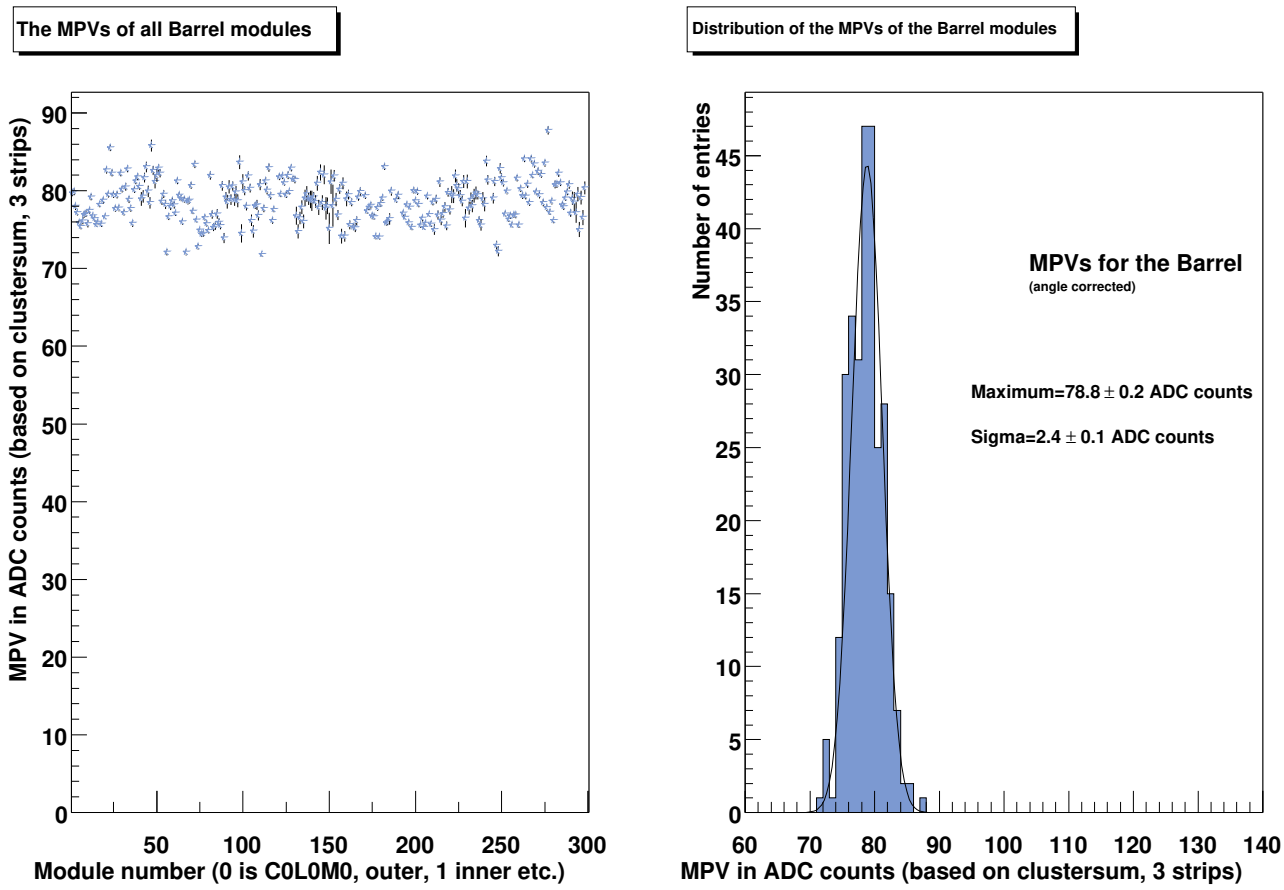

Figure 7.10: *The distribution of the* MPVs *(gain distribution) of the barrel* MVD *half modules. On the left, the* MPVs *are shown versus the module number (see text, starts at the innermost module). The values are based on the angular corrected data. On the right, the* MPV *distribution is shown. It is rather slim with a relative standard deviation of* 3% *and entered around* 78.8 ADC *counts.*

7.3 Related results of other analyses

Some results of analyses which were carried out parallel to the work for this thesis shall be summarised here.

7.3.1 Pedestal stability

An important result was gained by looking at the stability of the pedestal and noise values per channel during several data taking runs [29], as mentioned in section 7.1.1. All channels with unstable pedestal values also showed unstable noise behaviour. A detailed description of the thresholds set to determine the unstable channels is given in [29].

For the stable voltage configuration the number of identified noisy channels was less than 4‰.

7.3.2 The track resolution / track residuals

A track fit program was produced by the NIKHEF Institute [33]. It runs a different cluster algorithm and finds tracks by requiring seed hits in the outer layer of the MVD barrel section.

The status of the residual (distance between track and cluster position) analysis using this track fit program is shortly summarised here. A fundamental limitation in this analysis is the state of the MVD geometry files used. The data shown is based on the design geometry and does not yet include alignment corrections.

The cluster position is found by a centre of gravity method.
The residuals of one sensor are determined by fitting a track going through the surveyed sensor. Then that track is refitted neglecting the surveyed sensor and the distance of the identified cluster to this track is measured perpendicular to the strip direction.

The results obtained so far are shown in Fig. 7.11. The residuals have a current value of ~ 80 μm in the barrel section. Improvements like including the "true" geometry description of the MVD rather than the design geometry and improved cluster algorithms will reduce this value. The values obtained for the forward section are dominated by alignment uncertainties.

7.3.3 Efficiency of the barrel modules

The efficiency of the MVD barrel sensors was studied using the track fit as well. The results presented are of preliminary character.

To estimate the efficiency of the modules, tracks were fitted. The modules that should have contributed hits to these tracks were looked for.
The efficiency is the number of times a sensor is found to have contributed a hit of the track divided by the times it should have contributed a hit.

The very preliminary result is shown in Fig. 7.12. The Sensors which have efficiency zero are known bad sensors and were masked during the data taking.

The current approximate efficiency value of $\sim 97\%$ will certainly also improve with an enhanced cluster algorithm and geometry description.

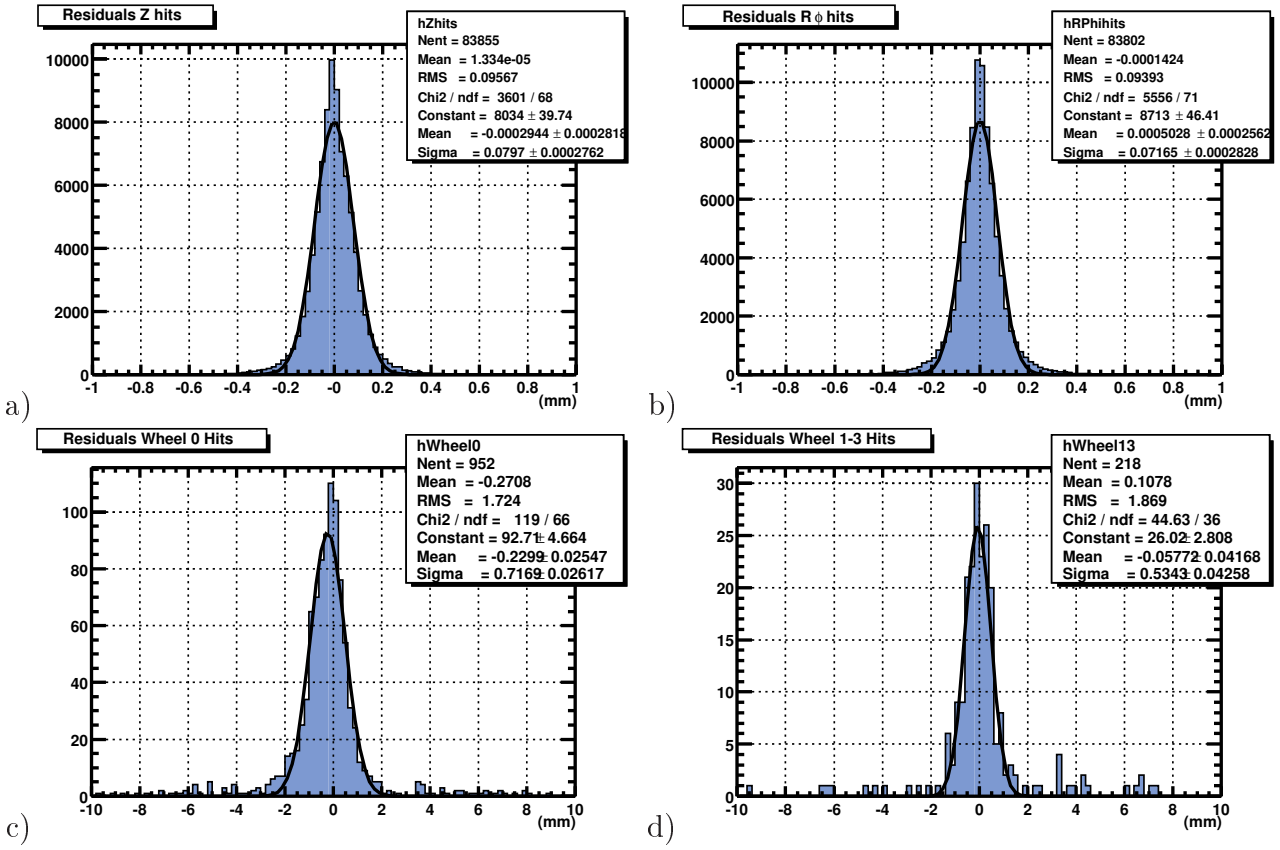

Figure 7.11: *The track residuals using the* MVD *design geometry and a centre of gravity approach for the cluster positions. a) and b) show the z and $r\varphi$ residuals of the ladders respectively. The residuals of the wheel closest to the barrel section are shown in c), those of the following 3 wheels are shown in d). The very low number of tracks in the forward section and alignment uncertainties are a restriction here. [33]*

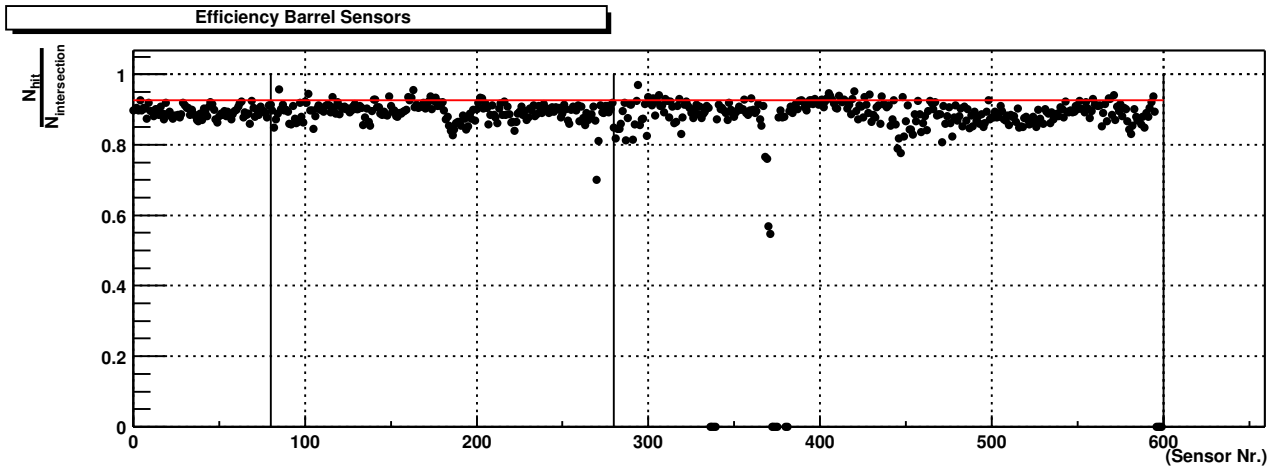

Figure 7.12: *The efficiency of the barrel* MVD *sensors is shown. The vertical lines separate the 3 layers, starting with the innermost one at the left. The active area is about 0.93 of the total sensor area. The estimated geometrical efficiency is indicated by the line at 0.93 [33].*

Further analysis options

Initially it was planned also to use the track fit program in the analyses described in the sections 7.1 and 7.2. An algorithm defining an allowed volume spanned by two trigger releasing scintillators was developed and has been included in the track fit program.
The use of this algorithm would e.g. have allowed interesting noise studies, as the hits inside the allowed volume are "hit" biased and the ones outside are noise biased. Due to time limitation this study was not yet performed.

Chapter 8

Conclusion

The Micro-Vertex Detector system test was successful. Stable and reliable operation was achieved and a set of cosmic ray test data could be collected.

A scintillator coincidence setup allowed to use cosmic ray induced muons as a data source. The setup was designed and constructed using existing components, and arranged around the MVD. All components of the setup were checked and calibrated. Finally the setup was integrated into the system test readout. It worked stably and reliably. The scintillator hit distribution was flat indicating well-balanced behaviour of the single scintillators. The efficiency for vertical muons was close to 100%.

The system test data were used for first analyses of the MVD performance. Comparing the forward and barrel section of the MVD, similar detection efficiency could be demonstrated.
It could be established that the readout timing of barrel and forward section was well adjusted. The average timing of barrel and forward MVD agreed within a nanosecond and the half modules showed a maximum deviation of 8 ns from the average timing.
The response of the detector to minimal ionising particles yields the expected landau shape. The angular dependance of the signal height distributions was studied. The angular corrected peaks of the signal distributions of the barrel MVD half modules follow a Gaussian distribution with the peak at 78.8 ADC counts and a standard deviation of 2.4 ADC counts. This corresponds to a gain distribution with a relative width of 3%.
Further analyses yield e.g. track residuals which have currently reached a value $\mathcal{O}(80\ \mu\text{m})$. The average efficiency of the barrel modules is better than $\sim 97\%$.

Furthermore, the system test data will be used as a reference for comparisons with later MVD data sets, e.g. to monitor the MVD detector quality.

Acknowledgements

I would like to thank:

R. Klanner for making this interesing thesis possible. My brilliant and very engaged tutor A. Geiser for many a patient explanation and strong support. T. Carli for providing the basic analysis tools and also for patient support. B. Koppitz for supplying all necessary hardware and teaching me a lot about it. U. Koetz for his precise hardware explanations and many a helpful question. J. Hauschild for supplying the scintillator support frame. A. Polini for integrating the scintillator setup into the system test readout. E. Maddox for making the trackfit available. The whole MVD group for continuous strong support and interest. A. Garfagnini, D. Dannheim and V. Chiochia for many an explanation concerning the MVD. V. Adler for supplying the bad channels, programming help and great teamwork. B. Kahle for the idea to estimate the rate of the sc. setup easily and together with C. Nguyen, J. Stahl and O. Gutsche for frequent support. U. Pein and P. Buhmann as well as the "Nukleare Messtechnik" group for strong support and a superb work environment. G. Magee for reading and correcting this thesis and finally my parents and family for supporting me continously.

Appendix A

The ZEUS coordinate system

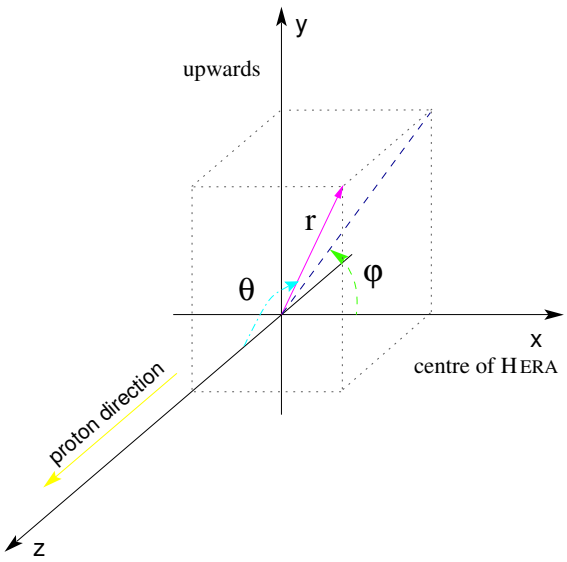

Figure A.1: *The* ZEUS *coordinate system. The z axis points along positive proton direction. The point of origin is located at the nominal interaction point. The angles θ (angle to z axis), φ (angle in xy plane) and the distance $r = \sqrt{x^2 + y^2}$ shown are standard polar coordinates. Unless stated otherwise, this system is used throughout the document.*

Appendix B

Scintillator numbering scheme

p.u. number	coded in the	bitword		bit number
3	2	1	0	in .evb longwords
31	21	11	01	00
32	22	12	02	01
33	23	13	03	02
34	24	14	04	03
35	25	15	05	04
36	26	16	06	05
37	27	17	07	06
38	28	18	08	07
		19	09	08
		20	10	09
				10
				11
				12
		30	29	13
				14
		40	39	15

Figure B.1: *Arrangement on the pattern units and in the "evb" data stream.*

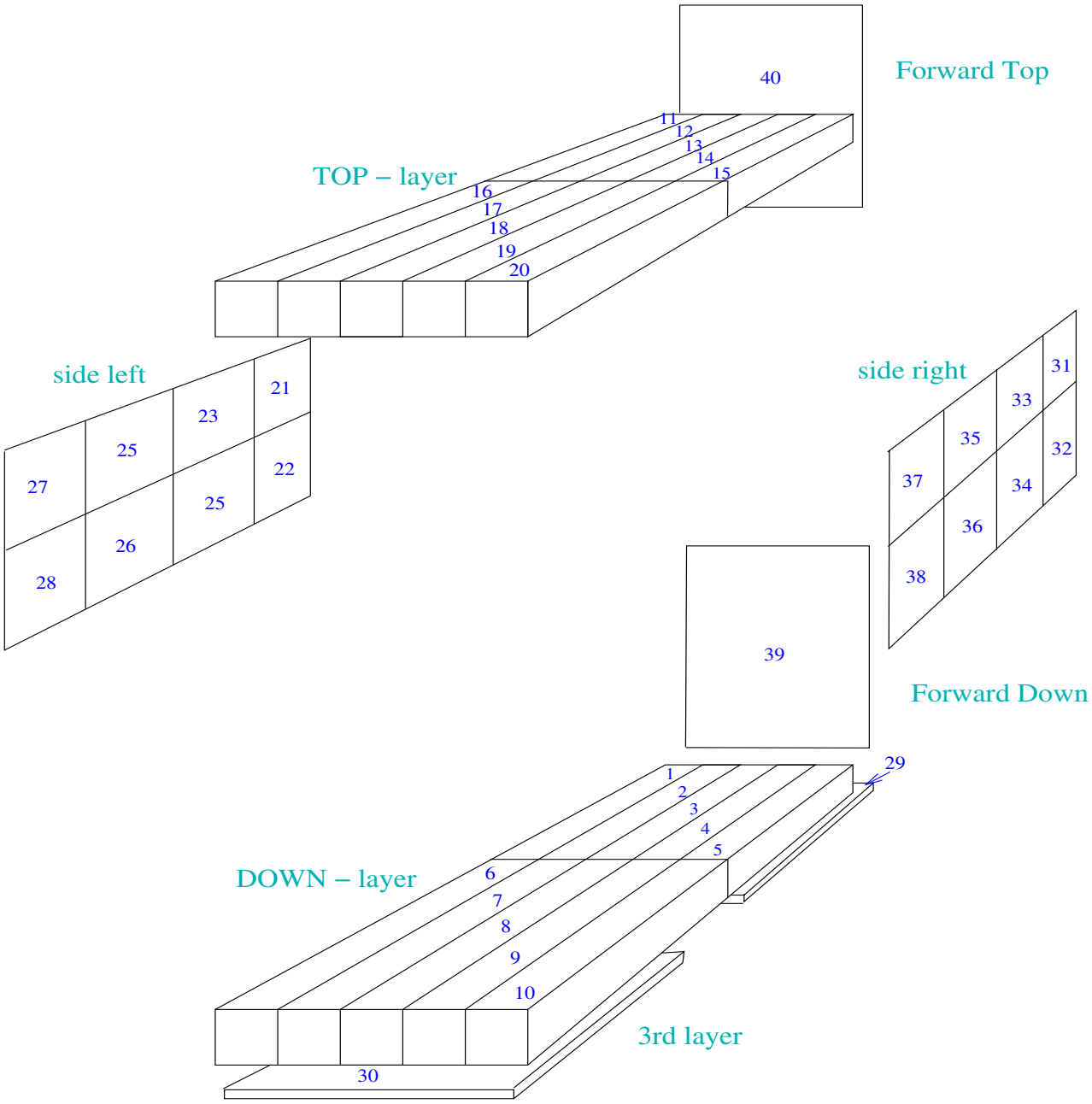

Figure B.2: *The scintillator numbering scheme.*

Appendix C

Estimation of the angle of incidence: error estimation

The estimation of the error introduced by the estimation of the angles of incidence is described here. The error was estimated geometrically, depicted in Fig. C.1.

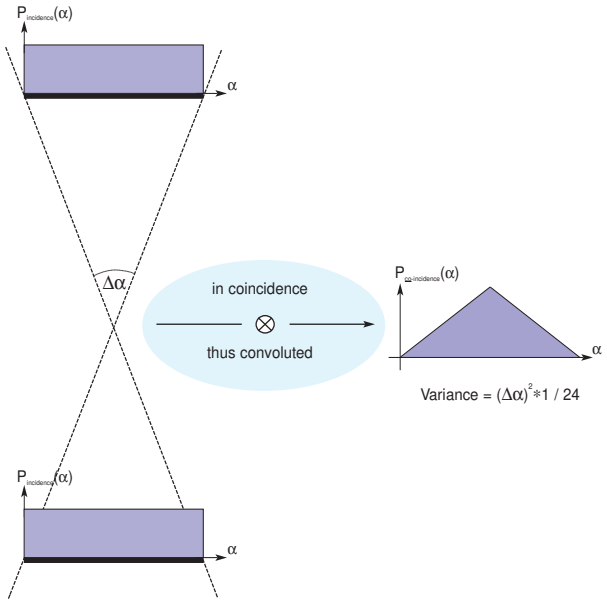

Figure C.1: *The origin of the triangular shape of the probability of incidence versus the angle of incidence is sketched here. Assuming uniform distributions for the separate scintillators the convolution of the distributions of two scintillators in coincidence yields a distribution of triangular shape. The absolute width of the distributions is estimated by the opening angle* $\triangle\alpha$.

The scintillators used to estimate the angle of incidence as described in section 7.2.3, were used in coincidence. To estimate the uncertainly of this estimation, it was assumed, that the probability of incidence of a single scintillator does not depend on the angle of incidence, yielding uniform distributions. A convolution of the distributions of the upper and the lower scintillator

yields the resulting distributions of the coincidence setup. This probability distribution is of triangular shape. The variance V of a triangular distribution with a absolute width of 1 is $V = \frac{1}{24}$. The absolute width of the angles of incidence is given by the geometrical opening angle $\triangle\alpha$ shown in Fig. C.1. Thus the error of the angles of incidence can be estimated by multiplying the absolute width with the variance of a triangular distribution. The opening angle in θ is larger than that in φ, as the extension of the scintillators in θ is larger, see Fig. 5.3. The opening angles in θ and φ are:

$$\begin{aligned} \triangle\theta &= 44.3^\circ \\ \triangle\varphi &= 9.3^\circ \end{aligned}$$

Thus the geometrical error can be estimated to be:

$$\begin{aligned} \sigma_\varphi &\sim \tfrac{9.3^\circ}{\sqrt{24}} &\sim 2^\circ \\ \sigma_\theta &\sim \tfrac{44.3^\circ}{\sqrt{24}} &\sim 9^\circ \end{aligned}$$

Appendix D

The ntuple

The clustered data was saved in a cluster wise organised ntuple. The contents of this ntuple are shown in Table D.1.

run nr.	***event nr.***	***detector section***	***cylinder***
each evb file contained one run of varying number of events	as the ntuple was organised cluster-wise, several entries had the same event nr.	1 for forward, 0 for barrel section	0 to 2 for the barrel section, always 0 for the forward section
ladder	***module***	θ	φ
0 to number of ladders per cyl. for barl. section, a wheel mod. for the forward section	0 to 4 in the barl. section, wheel number, also 0 to 4 in the forward section.	estimated angle rel. to z axis	estimated angle in the xy plane rel. to x axis
cluster sum inner	***cluster sum outer***	***sc. nr. 1***	***sc. nr. 2***
the cluster sum of the cluster found in the outer half module	the cluster sum of the cluster found in the inner half module	one of the 2 scintillators having released the coincidence signal	the entries are sorted by scintillator numbers. The 2^{nd} is the lower one.
highest strip nr. inner	***highest strip nr. outer***	***TDC time***	
contains the number of the highest strip in the outer half module. (ranges from 0 to 511)	contains the number of the highest strip in the inner half module. (ranges from 0 to 511)	the time measured by the TDC is stored here (250 ps stepsize)	

Table D.1: The entries of the ntuple are shown here. On the basis of this data, the analysis was performed.

Appendix E

Documentation of the code

The structure of the data that was analysed is presented, followed by the description of the applied code.

E.1 Data format

The MVD system test data stream is organised in tables. A table contains either the information of one logic unit of data acquisition devices, e.g. a number of ADCs positioned in one rack, or just information about the file itself, e.g. size, identifiers (names) of all included tables.

The tables again, are made up of 32 bit words ("longword"). The first word of a table contains the size of the table in bytes. The second is its identifier which is followed by the data.

Four tables were used: CAM1 and STR0/1/2:

- CAM1 is the table containing the scintillator and TDC (relative time between scintillator coincidence signal and the $\sim$ 10 MHz clock signal) information and was present in the MVD evb data stream only during the system test. The data, beginning at the third longword, contained entries from 4 pattern units (in the first 4 longwords, coded as shown in appendix B) followed by the TDC information (one set bit per 250 ps).
- STR0/1/2 contains address and charge per strip of the MVD sensors.
  This data is not the raw data as sampled by the ADC[1]: After sampling, the calculated common mode (general offset of the signals of one HELIX-chip, calculated per event) is subtracted, followed by the subtraction of the pedestal per channel (measured and calculated in pedestal runs performed in regular intervals and always anew when any configuration of the detector has been changed). To this pedestal suppressed data a loose cluster algorithm is applied (see section 6.6, ADC online cluster). Only strips passing this cluster algorithm are stored on disc to avoid saving huge amounts of irrelevant data.
  The identifier numbering (STR0 etc.) refers to separate units of ADCs situated in racks. STR0 is the 1st ADC rack, STR1 the 2nd etc.

[1]The ADC samples data coming from an electronic card called "analogue link". This card subtracts two streams of data coming from the HELIX chips: the "out" signal and the "dummy out" signal. The "dummy out" is a reference signa to the raw strip data in "out". For further details refer to [12]).

E.2 test.c ana.C / MvdAna

To find the clusters, apply cuts (on the cluster data and using scintillator information) and finally fill relevant data (run number, event number, cluster sum, address (of the highest strip of the cluster numbers, TDC time and angles) into the ntuple, a routine called "test.c", later "MvdAna" was used.
test.c is an interpreted macro in ROOT using CINT. It was later on replaced by the much faster "MvdAna", a compiled version linking the ROOT libraries. The main difference between the two routines is the slightly modified cluster algorithm (see: "do_cluster").

This section is meant to explain how MvdAna works, i.e. the ntuples were produced on which the analysis described in this thesis was based.

MvdAna loops over a given set of data files, i.e. over a given set of runs. In each run, each event is checked (not empty) and is subsequently read and filled into an integer array (called data[]).
Running over this array, a routine called "Get_abs_table" returns a pointer to the first data element of a required table (e.g. STR1 being the strip data of the modules connected to the ADCs in crate 1, see section E.1, or CAM1 being the hit and timing information of the scintillators and coincidence trigger connected to the pattern units and TDC in the CAMAC crate). Once the pointer is set, the complete table information (strip addresses (of strips in pre clusters found by the ADC) and corresponding counts (noise suppressed strip data)) or scintillator number and TDC time is stored in structures (called "mvd" and "gen_" respectively).

The mvd structure is subsequently scanned by the clustering routine "do_cluster". This is a simple cluster routine, not yet exploiting the known properties of the MVD sensors. The implementation of this is underway.
For each event, do_cluster searches for the highest strip in the outer and inner layer of each module. If the outer or inner highest strip is higher than the given parameter "smax" (usually set to $5 \times$ noise), the address of the module is saved in a structure called "selcluster". Additionally to the address of the module, the clustersum of both found clusters is stored. In test.c this cluster sum was just the counts on the highest strip, while MvdAna adds the highest and the 2 neighbouring strips to a 3 strip cluster[2].

The found clusters are scanned and filled into the ntuple. Here cuts using the scintillator information are applied:

- to reject shower like events no_shower(1) was applied, reducing the number of scintillator hits to 1 per layer and 2 in total (see section E.7)
- the pattern units used to record the scintillator hits occasionally recorded wrong scintillators, e.g. coincidence hits between TOP and Side layer or just hits in one layer. As events like this could not occur due to the logic connection of the scintillator signals (see section 7.1.3), they were rejected at this point.
- for some ntuples coincidence hits in the inner and outer module ("crossed hits") where required. This was done by asking the cluster sum of the outer and inner half module to be above 32 Adc counts (which is approximately 6 times the noise).

[2] do_cluster thus finds not more than 1 cluster per half module. Two tracks passing one module could not be found using this algorithm.

Subsequent the scintillator cuts was the calculation of the angles θ and φ. For this purpose angler was given the 2 scintillators having released the coincidence trigger and the result was stored in a double array which was then finally filled into the ntuple.

The ntuple was organised cluster wise and contained entries as shown in table D.1.

E.3 hexer

As described in section E.1, a bit is set to "true" in the evb data stream, if the scintillator connected to the corresponding port of the pattern unit has contributed to the coincidence signal. The bit words of the 4 pattern units are mimicked by "hexer":
The routine takes an integer number between 1 and 40 (corresponding to the scintillator numbers). It fills a 4 integer long global array with the pattern that would have been stored in the evb stream had only this scintillator fired. Slot 0 of the array corresponds to the entries in pattern unit 0, etc[3].
This pattern can than be compared to the one in the data stream, which is performed by:

E.4 matcher

If given a valid scintillator number, this routine uses "hexer" to produce the pattern described above. It then compares this pattern to the one stored in the structure "gen_.pu[i]" by MvdAna.

If at least the required scintillator has fired it returns 1, otherwise 0. To require a certain set of scintillators to have contributes to the coincidence signal, a combination of "matcher" requests can be done: e.g.
if(matcher(8)&&matcher(13)) printf("Scintillators 8 and 13 have fired!");

E.5 unhex

While "matcher/hexer" translate scintillator numbers to bit patterns, this routine translates bit patterns to scintillator numbers: the structure entries gen_.pu[i] of MvdAna are read by this routine. It needs to be given a pointer to a 41 integer long array [4]. If e.g. the scintillators nr. 10 and nr. 20 have fired, slot 10 is set to 10 and slot 20 is set to 20; all others are set to 0.

E.6 angler

If given a set of 2 scintillators and a pointer to a 2 double long array, "angler" calculates the connecting line of the centres of the scintillators. Then the θ and φ coordinates of this vector

[3]the original "hexer", not used in MvdAna, was able to take several scintillator numbers and produce the corresponding output. It became clear, that this was not necessary, so "hexer" was reduced to this simple form.

[4]This array is not 40 integers long, to have scintillator nr. 1 in slot 1 as the scintillators were numbered starting from 1.

(in the ZEUS coordinate system centred around the nominal interaction point) are calculated (using the scalar product). They are stored in the supplied array. "angler" returns 1 on success and 0 on wrong scintillator numbers.

The calculation of the connecting line and of the meaning of the two calculated angles shall now be explained a little closer. "angler" calls "coordinates", a subroutine which basically contains the positions of the scintillator centres in millimeters. The difference of these two 3 dimensional points gives the connecting line. The scalar product with the elementary vector along the z axis divided by the product of the absolute values of the two vectors yields θ. φ is calculated by using the same formula with the trajectory projected to the xy plane and the elementary vector along the x axis.
The so determined angles are used to calculate the estimated angle of incidence of the passing particle for every sensor. The error introduced by this estimation is discussed in appendix C.

The segmentation in φ is rather fine and leads to a maximum error on φ of $\sigma_\varphi \sim 2°$. The segmentation in θ is somewhat larger and leads to an upper limit on θ of $\sigma_\theta \sim 9°$.

E.7 no_shower

"no_shower" is a little subroutine using matcher to reject events with shower like appearance in the scintillator pattern. Shower events (hadronic or electronic) are likely to release more than one scintillator per layer[5] or more than 2 scintillators in total.
The maximum number of recorded scintillators per layer (max) is given to "no_shower" as argument. It returns 1 in case of acceptance and 0 in case of more than max scintillators recorded in one layer. Using it in the form:

```
if(no_shower) ntuple->Fill("clustersum", ...);
```

no_shower limits the number of scintillators per layer to max and additionally the total number of hits in all scintillators to $2 \times max$. Using "no_shower" results in considerably cleaner signal distributions.

[5] reminder: layers are: TOP layer, DOWN layer, Side left and Side right layer (see Fig. 5.3).

Bibliography

[1] B. Holzer, HERA *status* , at the ZEUS collaboration meeting, Feb. 2000

[2] U. Schneekloth, *The* HERA *luminosity upgrade* , Tech. report DESY 98-05, DESY, 1998.

[3] The ZEUS collaboration, *The* ZEUS *detector, status report 1993*, Tech. report, DESY, 1993.

[4] G. Wolf, *Deep Inelastic Scattering at Large Energy and Momentum Transfers: Recent Results from the* HERA *Collider*, DESY report 01-058, DESY, 2001.

[5] D. Griffiths, *Introduction to Elementary Particles*, Wiley, 1987.

[6] The ZEUS Collaboration, *A Microvertex Detector for* ZEUS, Tech. Report DESY-PRC 97/01, DESY, 1997.

[7] H1 collaboration, *Measurement of the Beauty Prod. Cross Section At* HERA *Using Lifetime Information*, subitted to the 30th Intl. Conf. on High-Energy Physics ICHEP2000, Osaka, Japan, July 2000.

[8] H1 collaboration, *Beauty Prod. in Deep Inelastic ep Scattering*, subitted to the Intl. Conf. on High-Energy Physics, Budapest, July 2001.

[9] William R. Leo, *Techniques for nuclear and particle physics experiments : a how-to approach*, Springer, 1994.

[10] M. Milite, Ph.D. Thesis, Universitiy of Hamburg, *to be published*

[11] U. Koetz, Nucl. Instr. Meth. A **461** (2001) 210

[12] Wolfgang Fallot-Burhardt et. al., ASIC Labor Heidelberg HD-ASIC-33-0697 or for additional information: http://wwwasic.kip.uni-heidelberg.de/~feuersta/projects/Helix/ .

[13] T. Fusayasu and K. Tokushuku, *Analog readout modules for the ZEUS microvertex detector,* Nucl. Instrum. Meth. A **436** (1999) 281.
Further information is summarised at
http://www-zeus.desy.de/components/mvd/electronics.html .

[14] A. Garfagnini and U. Kotz, *The assembly of the silicon modules for the ZEUS Micro Vertex Detector,* Nucl. Instrum. Meth. A **461** (2001) 158.

[15] J. Martens, *Simulationen und Qualitätssicherung der Siliziumstreifen-Detektoren des* Zeus*-Mikrovertexdetektors,* Diploma Thesis, Desy-Thesis-1999-044, Universität Hamburg, 1999.

[16] V. Chiochia, Proceedings of the X Int. Workshop on vertex detectors, Brunnen, Switzerland, Sep. 2001, submitted to Nucl. Inst. and Meth. A

[17] I. Redondo Fernandez, *Charm electroproduction at HERA,* Desy-Thesis-2001-037.

[18] D. Dannheim, *The Silicon Strip Detectors of The* Zeus *Microvertex Detector,* Diploma Thesis, Desy-Thesis-1999-027, Universität Hamburg, 1999.

[19] T.K. Gaisser et al., European Physical Journal C15 (2000) 1, cap. 20 (Pdg).

[20] D.E. Groom et al., European Physical Journal C15, 1 (2000).

[21] D. H. Wilkinson, *Ionization energy loss by charged particles. I: The Landau distribution*, Nucl. Instrum. Meth. A **383** (1996) 513.
further information at
http://wwwinfo.cern.ch/asdoc/geant/node273.html

[22] The layout of the transport frame is described at
http://www.nikhef.nl/pub/departments/mt/projects/zeus/vertex/assemblyframe/ .

[23] An introduction to Camac: http://www-esd.fnal.gov/esd/catalog/intro/introcam.htm or alternatively http://www.lecroy.com/lrs/appnotes/introcam/introcam.htm .

[24] A short article on Cockroft-Walton voltage multipliers is found at
http://www-ed.fnal.gov/projects/snowmass/accelerators.html

[25] M.Sutton and C.Youngman, *The Global Tracking Trigger System and Architecture* , Zeus-Note 99-074 (1999).

[26] M.Hayes, "Green" event display. Zeus Mvd Daq group documentation.

[27] On the Mvd laser alignment:
http://www2.physics.ox.ac.uk/designoffice/ZEUS/default.htm .

[28] E.Koffeman, H. Tieke, J.J. Velthuis, *Influence of Humidity on the Leakage Current of the Silicon Strip Sensors in the* Zeus Mvd, Zeus-Note 01-045 (2001).

[29] V. Adler, *The System Test of the* Zeus *Microvertex Detector: Calibration and Digitisation of the Detector Signals* , Dipl. thesis in preparation, Uni Hamburg, 2001.

[30] The Adc cluster algorithm is described at http://www-zeus.desy.de/~toku/mvd/adcm-argo.htm .

[31] A web interface to the Mvd system test bad channels:
http://www-zeus.desy.de/ gallo/ZEUS/mysql2/output.html

[32] E. Koffeman and E. Maddox, Full Geometry and Material Description of the Zeus Mvd, http://www.nikhef.nl/~h21/mvd_geo/download/bluebook/ .

[33] E. Maddox, Excerpt of the current status of the system test data analysis and the trackfit algorithm,
http://www.nikhef.nl/ h21/systemtest/ .